

BULGARIAN CHEMICAL COMMUNICATIONS

2020 Volume 52 / Special Issue E

Selected of papers presented on the "Sofia Electrochemical Days 2019" –
National Conference with International Participation, October 16 – 19, 2019,
Sofia, Bulgaria

*Journal of the Chemical Institutes
of the Bulgarian Academy of Sciences
and of the Union of Chemists in Bulgari*

EDITORIAL

National conference “Sofia Electrochemical Days’2019” (SED’2019) 16-19 October, 2019, Sofia, Bulgaria

The current issue of Bulgarian Chemical Communications consists of papers, presented as lectures and posters at the 7th national conference with international participation “Sofia Electrochemical Days’2019” held in Sofia from 16 to 19 October 2019.

SED’2019 was organized by Institute of Electrochemistry and Energy Systems – BAS, with the support of the Bulgarian Electrochemical Society and in collaboration with the University of Chemical Technology and Metallurgy – Sofia, Institute of Physical Chemistry – BAS and Joint Innovation Centre of the Bulgarian Academy of Sciences.

The event was sponsored by International Electrochemical Society and Bulgarian National Science Fund.

This forum, dedicated to the 150th anniversary of the Bulgarian Academy of Sciences gathered more than 70 participants from 8 countries - young and experienced scientists, representatives of various academic institutions and companies. The conference was opened by Prof. Konstantin Hadjivanov, Vice

Chairman of the Bulgarian Academy of Sciences. The first lecture at this forum was dedicated to the life and work of Prof. Dr. Zdravko Stoynov, a long-time ISE member and its regional representative for Bulgaria, as well as a conference founder.

The organizers would like to express their gratitude to the SED’2019 participants for their contribution to the conference success and also for the warm and collaborative atmosphere they created. We express our sincere thanks to the authors for their impressive presentations, to the referees for their efforts in reviewing the submitted manuscripts and to the Editorial Board of the Bulgarian Chemical Communications for the publications in this issue.

Guest editors:

Antonia Stoyanova

Vania Ilcheva

*Academician Evgeni Budevski Institute
of Electrochemistry and Energy Systems,
Bulgarian Academy of Sciences*

Graphene-based poly(vinyl alcohol)/chitosan hydrogels with electrochemically synthesized silver nanoparticles for medical applications – a review

Katarina R. Nešović, Vesna B. Mišković-Stanković*

University of Belgrade, Faculty of Technology and Metallurgy, Karnegijeva 4, Belgrade, Serbia

Received January 20, 2020; Accepted February 13, 2020

Silver nanoparticles (AgNPs) have become an interesting alternative to antibiotics for potential applications in biomedicine, since nanocrystalline silver is proved to be highly efficient antimicrobial agent with a wide inhibiting spectrum against many types of microorganisms. AgNPs embedded in hydrogel matrices are attractive for biomedical applications due to the possibility for their controlled release resulting in enhanced antimicrobial activity. Thus, combination of AgNPs with biocompatible hydrogels, poly(vinyl alcohol) (PVA) and chitosan (CHI), provides potential for design of improved medical treatments and devices (antimicrobial wound dressings, soft tissue implants). Graphene (Gr) has exceptional mechanical properties and has therefore been applied as adequate reinforcing component for polymer-based composite materials. The synthesis of AgNPs is always subject to innovation and improvements, as it is desirable to minimize the use of chemical agents with the aim of improving the biocompatibility of the obtained material. With this in mind, a green alternative to traditional chemical synthesis methods would be the electrochemical reduction of silver ions, especially as this method provides the option of direct in situ synthesis of AgNPs inside the polymer matrix. In this paper, we provide an overview of the state of the art regarding graphene-reinforced polymer matrices with electrochemically synthesized silver nanoparticles for medical application. We show that the electrochemical method of AgNPs synthesis in PVA/CHI hydrogel matrices has emerged as an excellent method to obtain nanoparticles, and that the incorporation of graphene improved the hydrogels' mechanical properties and elasticity.

Keywords: graphene, chitosan, silver nanoparticles, electrochemical synthesis, hydrogel

INTRODUCTION

Recent trends in biomedical materials science have emerged regarding the research of novel wound dressing materials to improve their antibacterial and anti-inflammatory properties, as well as longevity and controlled delivery of active components. These are the most prominent features where the traditional dressing materials come short, as they have some glaring drawbacks, especially when it comes to treating chronic wounds. Particularly big problem is the need for almost daily replacement of gauzes and cotton bandages, due to their susceptibility to bacterial colonization and proneness to dry out and adhere to the newly-grown fibrous tissue on the wound [1,2]. Hydrophilic polymers represent an exciting perspective to overcome these drawbacks, as they are a group of materials with many possibilities that can be tailored to suit the needs of chronic wound patients. Hydrogels based on both synthetic and natural-origin polymers have emerged as prospective moisture-retentive wound dressing materials for long-lasting wound healing applications [1,3]. Poly(vinyl alcohol) (PVA) is a synthetic polymer with exceptional biocompatibility that has been used in bio-

applications for over half a century [4], and it provides a great structural matrix for hydrogel wound dressings, due to its ability to form physically cross linked hydrogels via the facile freezing-thawing route [5]. PVA is often blended with natural-origin polymers to improve its bioactivity, such as polysaccharide chitosan (CHI), which is a partially deacetylated derivate of chitin – long-chain N-acetylglucosamine polymer derived from crustacean exoskeletons and fungi cell walls [6]. CHI, an acidic media-soluble polymer, is an exciting component for wound dressing materials, due to its intrinsic antibacterial activity that stems from the presence of protonated $-NH_3^+$ groups on its chain [7], as well as due to the well-documented ability to provide an excellent matrix for immobilization of antibacterial metallic nanoparticles [8,9]. Out of the many metals used in antibacterial applications, silver nanoparticles (AgNPs) have long been known as one of the strongest and most versatile antimicrobial agents with a broad-spectrum activity against many microorganisms [10,11]. The nanocrystalline form of silver has been shown to possess enhanced antibacterial activity compared to silver-ion

* To whom all correspondence should be sent.
E-mail: vesna@tmf.bg.ac.rs

formulations, due to the multi-faceted mode of action as well as the ability to also release Ag⁺ ions through oxidative dissolution in aqueous physiological media [10]. AgNPs also exhibit size-dependent activity – the smaller the nanoparticle, the higher the antibacterial effect [12]. High surface energy of very small AgNPs makes them very unstable though, so they are usually stabilized inside polymer matrices, such as hydrogels, to ensure long-term efficiency [12]. Of the many methods to synthesize AgNPs in a hydrogel matrix, *in situ* electrochemical route has emerged as a facile and green alternative to the usual chemical reduction [13–15]. The obtained AgNP-loaded hydrogels can, however, suffer from poor mechanical properties and susceptibility to degradation, especially chitosan-based blends, due to the poor mechanical strength of CHI [16]. Thus, research has shown that hydrogels can be reinforced by the means of a nano-filler addition, such as graphene (Gr), which can improve the stability of the hydrogel even at small loading amounts [17–20]. Gr, the two-dimensional (2D) prodigy of a material, has many exceptional properties [21], and has found a versatile application even in biomedical materials fields [22].

In this work, we provide a brief overview of PVA and chitosan-based, graphene-reinforced hydrogel materials with antibacterial electrochemically-synthesized AgNPs for next-generation wound dressing materials.

Graphene-based hydrogels for medical applications.

Since its discovery at the beginning of this century, graphene (Gr) has revolutionized many areas of materials science and opened up a plethora of new possibilities and research directions. A honeycomb 2D lattice of carbon atom monolayer, graphene has exhibited many fantastic expected and unexpected properties [21], which opened the door to its applications in broadest spectrum of materials science and engineering fields. Graphene has shown such diverse applicability which one would not think possible and it is researched for applications in electronics [23], photovoltaics [24], energy storage [25,26], biosensors [27]. Aside from its special properties such as mechanical strength, electrical conductivity, zero-bandgap semiconductivity [21] and high specific surface area [22], Gr was even shown to exhibit antibacterial activity that gave rise to significant interest in graphene nanocomposites bio-applications such as wound dressings or drug delivery [22].

Composite polymer hydrogels with added graphene or its derivatives such as graphene oxide (GO), have drawn significant attention in wound dressing and tissue engineering fields [22]. Fan et al. [28] have shown that konjac glucomannan/carboxymethyl chitosan/graphene oxide wound dressings exhibited significant increase in compressive strength and modulus, as well as improved biocompatibility towards NIH-3T3 mouse embryonic cells with increased GO content; whereas it was also shown that GO incorporation improved Young's modulus, maximum compression stress and strain of poly(acrylic acid)/gelatin hydrogels [29]. Gelatin methacrylate hydrogels with incorporated GO also enhanced proliferation of HaCaT keratinocyte cells [30]. An interesting study showed that free-standing graphene hydrogels could possess osteoinductivity and ability to promote bone tissue regeneration, as confirmed by both *in vitro* and *in vivo* tests [31]. Sodium carboxymethyl cellulose/reduced graphene oxide hydrogels exhibited anti-biofilm activity, reducing *S. aureus* and *P. aeruginosa* biofilm formation by ~80% and ~60%, respectively [32]. Ag/graphene composite hydrogels cross linked with acrylic acid and N,N'-methylenebis(acrylamide) possessed strong *in vitro* antibacterial activity and enhanced *in vivo* wound healing [33]. Ma et al. [34] showed that sodium alginate/graphene oxide (GO)/poly(vinyl alcohol) nanocomposite sponges loaded with norfloxacin had excellent antibacterial activity against *E. coli* and *S. aureus*, while also promoting wound healing *in vivo*. Another study investigated ciprofloxacin-loaded chitosan/poly(vinyl alcohol)/graphene oxide nanofibrous membranes and confirmed significant inhibitory effect against *E. coli*, *S. aureus* and *B. subtilis*, along with good cytocompatibility [35]. Bacterial nanocellulose/poly(acrylic acid)/graphene oxide composite hydrogels promoted attachment and proliferation of human dermal fibroblast cells, indicating good wound healing potential [36]. Graphene was also incorporated in poly(vinyl alcohol) [14,18,37–39] and poly(vinyl alcohol)/chitosan [13,15,17,40,41] hydrogels and films with incorporated silver nanoparticles (AgNPs) for wound dressing applications, where it was shown that very small amounts of Gr improved elasticity and strength of these wound dressing materials [17,18].

Quite obviously, graphene has found wide application in biomedical field, and this short review will cover some aspects of graphene-loaded hydrogels based on poly(vinyl alcohol) and chitosan polymers, as antibacterial wound dressing materials.

Silver nanoparticles as an antibacterial agent and their electrochemical synthesis.

Silver nanoparticles have long been recognized and established as one of the strongest antimicrobial agents [11], with broad-spectrum performance and without the inherent risks associated with antibiotics that are well known to quickly induce bacterial resistance, due to their targeted modes of action [42]. The modes of action of AgNPs have been long and widely investigated, and covered in several comprehensive reviews [11,12,43]. Most studies agree that the AgNPs antibacterial activity stems from their large surface area that allows direct contact with the bacterial cell wall, which results in various types of membrane damage, cytoplasm leakage as well as in penetration inside the cell itself [12,43]. Further, the AgNPs can participate in generation of reactive oxygen species (ROS), as well as undergo oxidative dissolution, resulting in the release of Ag^+ ions, which, in turn, also possess significant antibacterial activity [44]. The antibacterial activity of AgNPs is also known to be dose-dependent and size-dependent, with most research works indicating that the nanoparticles smaller than 10 nm, exhibit the strongest antibacterial effect [12]. As described above, the mode of action is very versatile, which makes it difficult for bacteria to develop resistance mechanism, rendering the AgNPs an excellent choice for an active agent in wound dressings for long-term application. However, a non-negligible risk with silver nanoparticles application is their documented toxicity towards healthy mammalian cells [12]. The mechanisms of AgNP cytotoxicity are similar to those of their antibacterial action, with cellular uptake, Ag^+ release, DNA and protein damage, and ROS generation being some of the most widely cited causes of toxicity [12]. Besides dose-dependent cytotoxicity, a major issue is also potential accumulated toxicity caused by accumulation of smaller amounts of silver in cells and tissue over longer periods of time [12,45]. Therefore, when designing silver-containing wound dressing material, the dose is of crucial importance and the release effects must be taken into account, in order to achieve a product which can retain antibacterial properties for long time periods, all the while not posing a threat towards the healthy tissue.

One of the most reliable methods to obtain silver nanoparticles in polymer gels and dispersions is certainly electrochemical synthesis [14,15,37,40,46]. The merits of this method include one-step setup and the avoidance of possibly toxic chemical agents for Ag^+ reduction. There are various electrochemical techniques for AgNPs synthesis,

including reduction in polymer dispersion, where the AgNPs are stabilized by polymer chains [37,46,47], as well as *in situ* reduction in a hydrogel matrix, where the main purpose of electric current is to serve as an intermediary to produce hydrogen gas on the cathode, which then permeates the hydrogel, reacting with Ag^+ ions to form nucleation sites for the formation of AgNPs [13,17]. One such principal scheme for this type of *in situ* electrochemical synthesis is presented in Fig. 1, showing that the hydrogel, pre-swollen in Ag^+ precursor solution (usually AgNO_3 of desired concentration) is placed between the two platinum plates that serve as working and counter electrodes, and are connected to a DC power source, used to supply a constant voltage. Briefly, the hydrogels were obtained by first preparing the PVA/chitosan/graphene colloid dispersions without CHI and with 0.1 wt% CHI (PVA/0.1CHI/Gr) and 0.5 wt% CHI (PVA/0.5CHI/Gr), pouring them into Petri dishes up to 5 mm height and then cross linking by the physical freezing-thawing technique [15,17,40]. After 5 cycles of freezing and thawing, the hydrogels were cut to 10 mm \times 5 mm discs and the electrochemical synthesis was performed as follows. The obtained hydrogel discs were immersed in 3.9 mM AgNO_3 precursor swelling solution and swollen for 48 h, after which they were placed in the electrochemical cell depicted in Fig. 1 and subjected to 90 V constant DC voltage, to obtain silver-loaded hydrogels (3.9Ag/PVA/Gr, 3.9Ag/PVA/0.1CHI/Gr and 3.9Ag/PVA/0.5CHI/Gr) [15,17,40].

The advantage of this *in situ* method is the fact that the synthesis is performed in a single step, and the final product is a nanocomposite hydrogel with incorporated AgNPs, which is completely biocompatible and there is no need to perform subsequent washing and extraction of unreacted chemicals, as is the case with the chemical AgNP synthesis method. A representative photograph of poly(vinyl alcohol)/chitosan/graphene (PVA/CHI/Gr) and silver/poly(vinyl alcohol)/chitosan/graphene (Ag/PVA/CHI/Gr) hydrogels, obtained using the above-described method is shown in Fig. 2 – typical yellow coloration of the hydrogel sample in Fig. 2b attests to the successful formation of AgNPs.

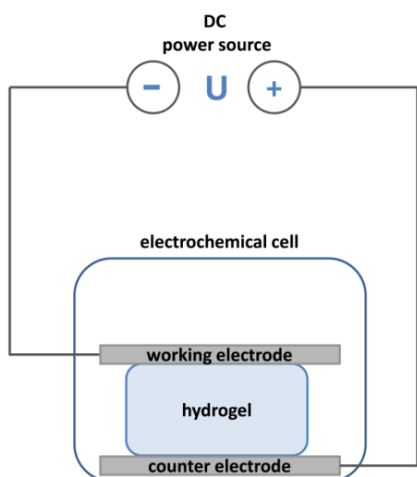


Fig. 1. Scheme of the electrochemical setup for the synthesis of silver/poly(vinyl alcohol)/chitosan/graphene hydrogel

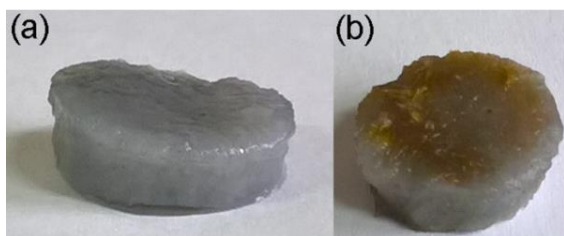


Fig. 2. Images of (a) poly(vinyl alcohol)/chitosan/graphene and (b) silver/poly(vinyl alcohol)/chitosan/graphene hydrogels

Chitosan has been repeatedly shown to significantly influence the formation and concentration of AgNPs inside the hydrogel matrices, as confirmed by much higher absorbance value in the UV-vis spectrum of hydrogel containing CHI, compared to that without it (Fig. 3) [15, 17]. A plausible explanation would be the mild reducing properties of CHI itself that could contribute to the quicker formation of AgNPs inside the CHI-containing hydrogels. This effect will be examined in a bit more detail in the following sections.

The effect of graphene on the properties of PVA/CHI hydrogels with AgNPs.

Mechanical strength and elasticity are some of the most important physical properties of a wound dressing, which can ensure prolonged structural integrity of the dressing material that is usually to be used over longer time periods. Graphene, when used as a nano-filler inside three-dimensional (3D) polymer matrices, is known to dramatically

improve their mechanical properties, such as elasticity or yield strength [20,29].

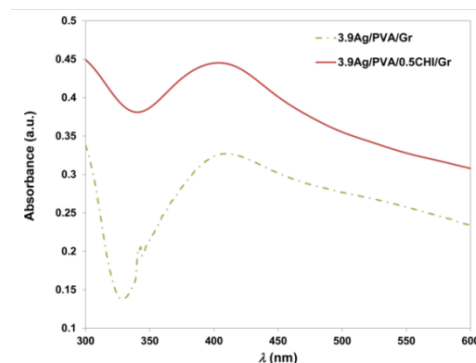


Fig. 3. Representative UV-vis spectra of silver/poly(vinyl alcohol)/graphene hydrogels (3.9Ag/PVA/Gr) and silver/poly(vinyl alcohol)/0.5 wt% chitosan/graphene hydrogels (3.9Ag/PVA/0.5CHI/Gr) hydrogels, showing characteristic absorbance maximum of AgNPs at ~400 nm.

Loading small amounts of Gr in polymeric matrices has been shown to improve mechanical properties of poly (acrylic acid) [48], polylactide/poly(ϵ -caprolactone) blend [49], as well as poly(vinyl alcohol) [18,50] and poly(vinyl alcohol)/chitosan hydrogels [17]. For example, the effect of graphene loading on the mechanical properties and elasticity of poly(vinyl alcohol)/chitosan matrices, can be seen very distinctively from the Table 1 [17]. Films with 10 wt% PVA and varying amounts of chitosan – 0.1 wt% (PVA/0.1CHI) and 0.5 wt% (PVA/0.5CHI) were prepared, and it was observed (as expected) that the increased amount of chitosan decreased the overall mechanical stability of PVA/0.5CHI, which exhibited much lower yield strength as well as elasticity modulus [17]. On the other hand, the addition of very small amount of graphene (0.01 wt%) drastically increased both elasticity modulus and yield and ultimate strength of the PVA/0.5CHI/Gr sample (Table 1) [17]. Other studies have confirmed the same, showing that Gr can be used as a very strong reinforcing material which imparts excellent mechanical strength and elastic properties upon hydrogel matrices – which is especially important when using such natural-origin biopolymers with poor intrinsic mechanical properties, as chitosan.

Table 1. Mechanical properties of PVA/0.1CHI, PVA/0.5CHI and PVA/0.5CHI/Gr: σ_R – tensile yield strength, ε_R – yield elongation, E_J – Young’s elasticity modulus, σ_U – ultimate strength, ε_U – ultimate elongation. Reprinted from [17] with permission from Elsevier (Copyright 2019).

| | σ_R (MPa) | ε_R (%) | E_J (MPa) | σ_U (MPa) | ε_U (%) |
|---------------|------------------|---------------------|-------------|------------------|---------------------|
| PVA/0.1CHI | 30.7 | 2.7 | 21.4 | 38.5 | 28.1 |
| PVA/0.5CHI | 22.6 | 3.8 | 14.0 | 24.4 | 38.0 |
| PVA/0.5CHI/Gr | 78.0 | 1.3 | 121.7 | 63.1 | 23.2 |

However, graphene could not only influence mechanical properties of wound dressing nanocomposite materials. Gr has also been shown to affect the formation and stabilization of AgNPs inside the polymer matrix [51,52], although these effects have not been investigated thoroughly. UV-vis spectroscopy is a fairly reliable method to assess the amounts/concentrations of incorporated silver nanoparticles, as they give rise to quite distinctive peaks in the lower visible region, known as surface plasmon resonance (SPR) maxima [53]. When comparing the obtained UV-vis spectra for hydrogels with different amounts of chitosan (0, 0.1 and 0.5 wt%) [15,17,40], the first thing to be noticed is that hydrogels with higher chitosan content (Ag/PVA/0.5CHI/Gr) exhibited higher maximum absorbance ($A_{\max}=1.6$), compared to both Ag/PVA/Gr ($A_{\max}=0.45$) and Ag/PVA/0.1CHI/Gr ($A_{\max}=1.05$) [15] pointing to higher amount of AgNPs due to additional reduction on CHI chains, as already briefly discussed above. Further, it can be noticed that hydrogels containing graphene also possessed higher absorbance of their SPR peak, and therefore higher AgNP concentration, compared to their counterparts without Gr [13,15,17,40]. For example, 3.9Ag/PVA/0.1CHI/Gr ($A_{\max}=1.05$ [15]) and 3.9Ag/PVA/0.5CHI/Gr ($A_{\max}=1.6$ [15]) hydrogels exhibited higher A_{\max} than 3.9Ag/PVA/0.1CHI ($A_{\max}=0.3$ [13]) and 3.9Ag/PVA/0.5CHI ($A_{\max}=1.0$ [13]), respectively, which is also true for 0.25Ag/PVA/0.1CHI/Gr ($A_{\max}=0.1$ [40]) and 0.25Ag/PVA/0.5CHI/Gr ($A_{\max}=0.41$ [40]) hydrogels, compared to 0.25Ag/PVA/0.1CHI ($A_{\max}=0.05$ [13]) and 0.25Ag/PVA/0.5CHI ($A_{\max}=0.17$ [13]), respectively. Obviously, graphene can affect the formation and stabilization of AgNPs inside polymer matrices, likely through interactions and shielding nanoparticles from agglomeration, as it was shown before that Gr and Gr oxide can be even used as effective dispersion agents to support metal nanoparticles [52,54,55].

A complementary dynamic light scattering (DLS) technique revealed average hydrodynamic

diameters of the obtained nanoparticles to be 8.06 ± 0.098 nm for Ag/PVA/0.1CHI/Gr and 6.38 ± 0.12 nm for Ag/PVA/0.5CHI/Gr [17], indicating a strong influence of increased chitosan content on stabilization and consequent smaller size of AgNPs in the hydrogel.

These findings indicate that CHI plays a significant role in nanoparticle stabilization, which was also confirmed by transmission electron microscopy (TEM) (Fig. 4) [13,17]. TEM analysis indicated the incorporation of even very small nanoparticles inside the hydrogel matrices, such as the nanoparticle in Fig. 4d, sized around 2-3 nm in 3.9Ag/PVA/0.5CHI/Gr hydrogel. The statistical distribution of AgNPs obtained by DLS, coupled with the microscopic TEM investigation, confirmed the incorporation of very small AgNPs (<10 nm) inside hydrogels both with and without graphene, pointing to their strong potential as antibacterial agents for wound dressing.

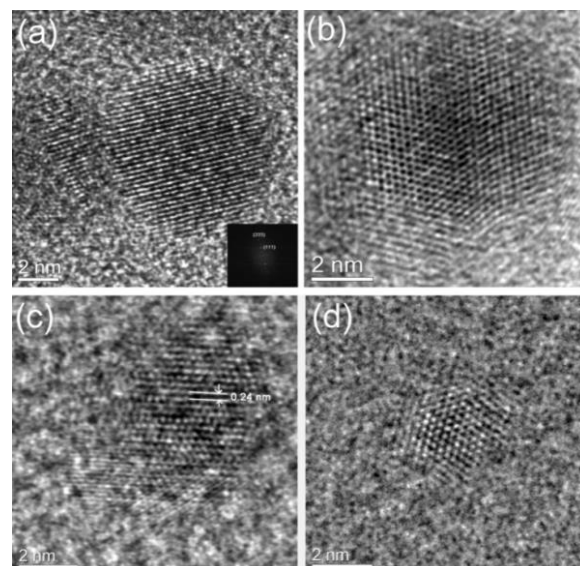


Fig. 4. TEM micrographs of (a) 3.9Ag/PVA/0.1CHI, (b) 3.9Ag/PVA/0.5CHI, (Reprinted from [13] with permission from Elsevier (Copyright 2019)) (c) 3.9Ag/PVA/0.1CHI/Gr and (d) 3.9Ag/PVA/0.5CHI/Gr (Reprinted from [17] with permission from Elsevier (Copyright 2019)).

Application of graphene-based poly(vinyl alcohol)/chitosan hydrogels with AgNPs – silver release and antibacterial properties.

As already mentioned, when designing a new wound dressing material with an active antibacterial component, it is very important to determine the release behavior of this agent, in order to tailor the properties of the dressing to achieve the optimal infection protection. The release measurements are usually carried out at 37°C, in some physiological buffer, such as phosphate buffer (PB) that mimics the physiological environment in human organism. In addition, the non-toxicity requirements for wound dressings dictate the incorporation of smaller amounts of AgNPs in order to achieve the best antibacterial effect without inducing any cytotoxic response [13,17]. Thus, for *in vitro* silver release and antibacterial experiments, hydrogels were prepared from lower-concentration precursor swelling solution (0.25 mM AgNO₃) [13,17,40]. Fig. 5 shows representative silver release profiles for 0.25Ag/PVA/0.1CHI/Gr and 0.25Ag/PVA/0.5CHI/Gr hydrogels, which were measured over 28-day period [40]. The release curves provide several interesting observations, the first being that the total initial concentration of AgNPs was higher in 0.25Ag/PVA/0.5CHI/Gr hydrogel (80 mg dm⁻³), compared to 0.25Ag/PVA/0.1CHI/Gr (55 mg dm⁻³) [40]. Further, the release profiles exhibited typical burst release in initial 3-5 days, followed by slower period until finally reaching a plateau. The 0.25Ag/PVA/0.5CHI/Gr hydrogel also retained higher amount of silver after 28 days (~50 mg

dm⁻³), in comparison with 0.25Ag/PVA/0.1CHI/Gr (~30 mg dm⁻³), ensuring that the hydrogel maintained sterility over prolonged time period.

More information from the release profiles can be extracted by fitting with well-known theoretical models that could be used to elucidate the kinetics of silver release. Some of the most common models – zero, first and second order kinetics – are presented in Table 2, along with equations that describe them and rate constant parameters that can be calculated from the fit. The silver release profiles, fitted with models from Table 2, for 0.25Ag/PVA/0.1CHI/Gr and 0.25Ag/PVA/0.5CHI/Gr hydrogels are shown in Fig. 6.

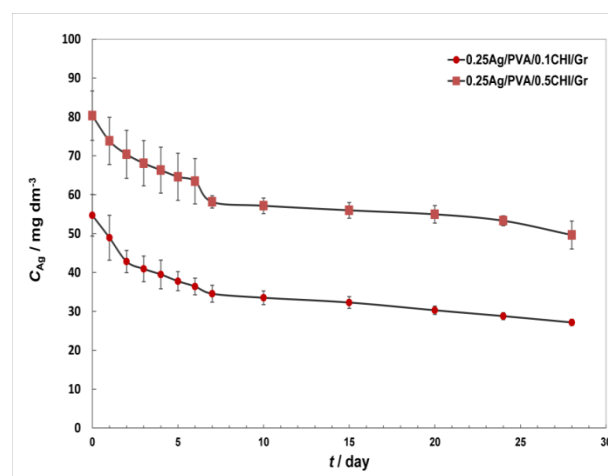


Fig. 5. Silver release profiles for 0.25Ag/PVA/0.1CHI/Gr and 0.25Ag/PVA/0.5CHI/Gr hydrogels [40]

Table 2. Kinetic models used to fit silver release profiles [41].

| Model name | Equation | Constants |
|--------------|---|------------------------------------|
| Zero order | $c_{Ag} = c_{Ag,0} - k_0 \cdot t$ | k_0 – zero-order rate constant |
| First order | $\ln c_{Ag} = \ln c_{Ag,0} - k_1 \cdot t$ | k_1 – first-order rate constant |
| Second order | $\frac{1}{c_{Ag}} = \frac{1}{c_{Ag,0}} + k_2 \cdot t$ | k_2 – second-order rate constant |

From Fig. 6, it can be observed that the release profiles cannot be fitted with one model over the entire release period, rather they are split into three, and two stages for 0.25Ag/PVA/0.1CHI/Gr and 0.25Ag/PVA/0.5CHI/Gr, respectively. The first stage that corresponds to shorter release times is characteristic for burst release behavior, where the release is quicker upon initial immersion of the hydrogel in PB medium. This first period is described by higher values of rate constants for all

three models (Fig. 6), compared to the latter period that corresponds to the time needed to reach the plateau on the release profile. In the case of 0.25Ag/PVA/0.1CHI/Gr, the burst release period actually comprised two stages with different release rates, indicating that the fastest release of AgNPs is actually achieved between 2 and 7 days. This delay in silver release in the first 48 h might not be ideal for wound dressing applications, as it is crucially important to achieve the highest initial inflow of the

antibacterial agent to the wound area, especially in this initial 2-day period. Therefore, the hydrogel with higher chitosan content (0.25Ag/PVA/0.5CHI/Gr) might be a better option for wound dressing material, as it does not show this discrepancy, exhibiting instead a smooth burst release period lasting up to 7 days. In addition, 7 days is a fairly long period for fast release, so these hydrogels would also possess a very desirable property of retaining antibacterial activity and maintaining long-lasting wound sterility, without the need for frequent replacements [40].

It should be also noted that all three kinetic models provided satisfactory correlation with the experimental data, especially for 0.25Ag/PVA/0.1CHI/Gr hydrogel, and especially in the initial burst release period. However, the best model should be chosen by evaluation of parameters in all stages, and it was found that the second order model provided the best fit for both

hydrogel samples and for all release periods ($R^2 > 0.99$ for burst period, and $R^2 > 0.97$ for long-term release). Another interesting observation could be made by comparing the results presented here with the release models for hydrogels without graphene from our previous study (0.25Ag/PVA/0.1CHI and 0.25Ag/PVA/0.5CHI) [41]. Hydrogels without graphene were also found to exhibit second-order kinetics of silver release [41]; however, for those samples only one smooth period was observed upon fitting with the second-order model. Obviously, the Gr-containing hydrogels exhibited different behavior, releasing silver in several stages with different rates, as shown in Fig. 6 and discussed above. These findings indicate that Gr could play a role in AgNPs stabilization, and that the interactions between Gr sheets and AgNPs might account for different release behavior of these hydrogels in comparison with their counterparts without Gr.

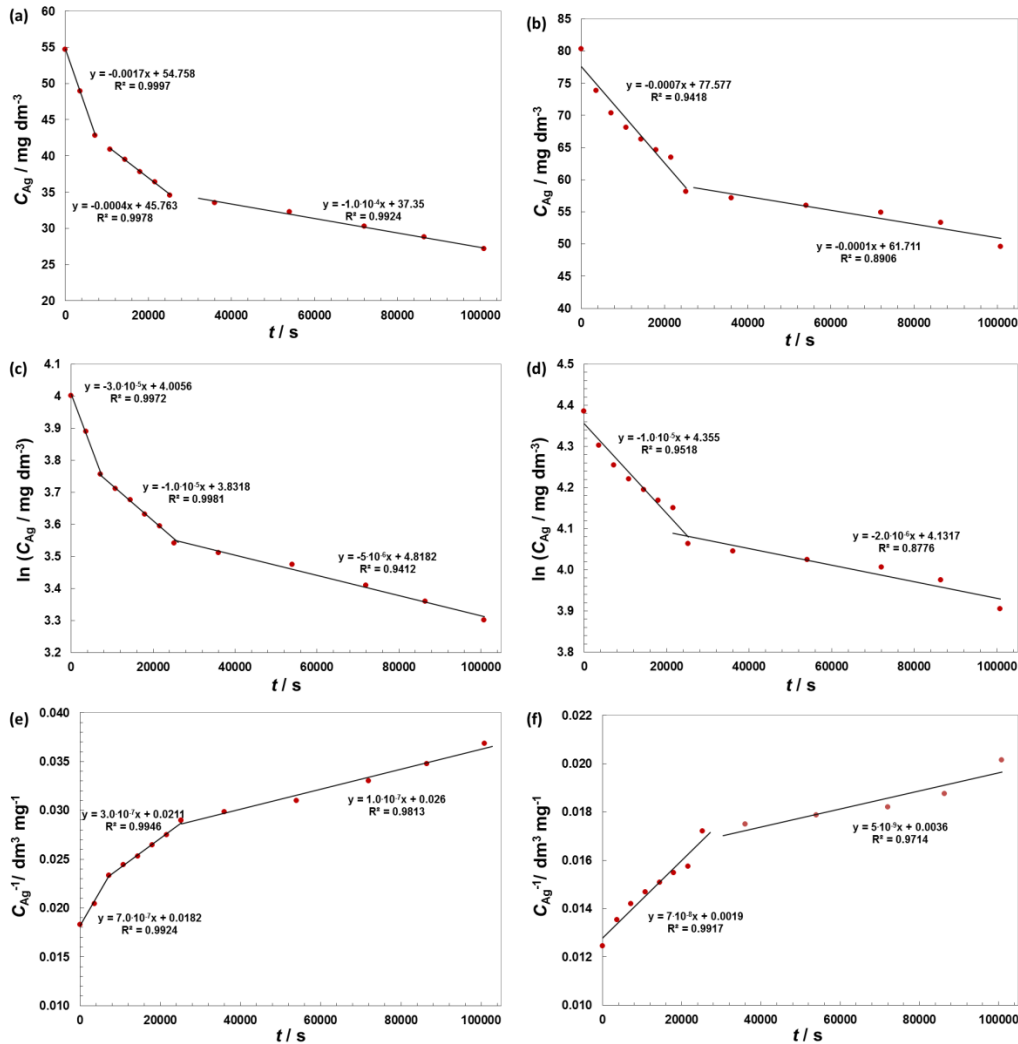


Fig. 6. Different models of silver release for (a,c,e) 0.25Ag/PVA/0.1CHI/Gr and (b,d,f) 0.25Ag/PVA/0.5CHI/Gr hydrogels: (a,b) zero, (c,d) first and (e,f) second order kinetics.

Finally, one of the most important properties of next-generation wound dressing materials is certainly their antibacterial activity. The requirements for a wound dressing are usually such that it needs to provide a long lasting antibacterial effect and sustained release of the active component to the wound area, in order to efficiently combat the colonization of bacteria. Especially critical are the first 24–48 h, when bacteria usually begin to form a biofilm and therefore it is imperative to achieve the most efficient antibacterial action in this period. This effect can also be accomplished by synergistic action of several antibacterial components, as is the case with chitosan-containing hydrogels with AgNPs [13,17,40,56]. Chitosan is a known intrinsically bactericidal polymer [7,57], whereas AgNPs act as a main agent that is to be released gradually for long-term protection of the wound. Furthermore, graphene has also been shown to be a potential antibacterial agent in certain cases [22,28,34,58]. One of the main culprits for wound infections is *Staphylococcus aureus* species [59], which normally inhabits the human skin, but can wreak havoc if it infects a wound. Another bacterial strain often found in wound infections is the Gram-negative *Escherichia coli*. Table 3 shows the results

of quantitative antibacterial suspension tests against *S. aureus* and *E. coli* for 0.25Ag/PVA/0.1CHI/Gr and 0.25Ag/PVA/0.5CHI/Gr hydrogels [17]. It can be observed that both hydrogels exhibited significant antibacterial activity after only 15 min, causing significant reduction in CFU counts of around 1 logarithmic unit. Furthermore, the hydrogel with higher CHI content (0.25Ag/PVA/0.5CHI/Gr), caused faster inhibition of bacterial viability after 15 min, compared to 0.25Ag/PVA/0.1CHI/Gr, pointing to strong influence of CHI on the hydrogel bactericidal action. After 15 min, there were 0.021×10^5 CFU ml^{-1} *S. aureus* cells remaining in the presence of 0.25Ag/PVA/0.5CHI/Gr, compared to 0.26×10^5 CFU ml^{-1} for 0.25Ag/PVA/0.1CHI/Gr [17]. In addition, 0.25Ag/PVA/0.5CHI/Gr destroyed *E. coli* cells more effectively (1.12×10^5 CFU ml^{-1}), compared to 0.25Ag/PVA/0.1CHI/Gr (6.03×10^5 CFU ml^{-1}) [17]. Thus, highly effective protection against bacteria was accomplished by chitosan-containing hydrogels, with both samples causing 100% destruction of bacterial cells after only 1 h, indicating significant synergy between CHI and AgNPs antibacterial action [13,17].

Table 3. Antibacterial test in suspension for 0.25Ag/PVA/0.1CHI/Gr and 0.25Ag/PVA/0.5CHI/Gr hydrogels with silver nanoparticles against *Staphylococcus aureus* and *Escherichia coli* – bacterial survival rates expressed as the number of colony forming units per milliliter (CFU ml^{-1}) [17]

| | Number of bacterial cells (10^5 CFU ml^{-1}) | | |
|----------------------|---|------------------|-----|
| | | <i>S. aureus</i> | |
| | 0 h | 15 min | 1 h |
| 0.25Ag/PVA/0.1CHI/Gr | 0.95 | 0.26 | 0 |
| 0.25Ag/PVA/0.5CHI/Gr | 0.95 | 0.021 | 0 |
| | | <i>E. coli</i> | |
| | 0 h | 15 min | 1 h |
| 0.25Ag/PVA/0.1CHI/Gr | 16.6 | 6.03 | 0 |
| 0.25Ag/PVA/0.5CHI/Gr | 16.6 | 1.12 | 0 |

CONCLUSIONS AND OUTLOOK

In this review, we have covered the existing research regarding poly(vinyl alcohol)/chitosan hydrogel wound dressings, reinforced by graphene filler and with silver nanoparticles, incorporated via *in situ* electrochemical synthesis method. Graphene, as a versatile material with many interesting properties has been shown to significantly improve mechanical properties of PVA and PVA/CHI hydrogels, and has even shown an indication of improved AgNPs stability in graphene-containing hydrogels. The electrochemical synthesis route is a very promising and green method to obtain silver

nanoparticles directly inside the polymer matrix of a hydrogel. The AgNPs obtained by electrochemical route were shown to exhibit very small sizes (in the 2–10 nm range) and their concentration inside the hydrogel matrix can be tailored to suit the requirements of the wound dressings. Chitosan was also shown to exert a great influence on the synthesis yield, as well as on the stability and antibacterial activity of AgNPs. Hydrogels containing chitosan were shown to exhibit burst release of silver during a longer period of 7 days, which would ensure the longevity of the dressing. Furthermore, the hydrogels with CHI and AgNPs have displayed enhanced antibacterial

efficiency and bactericidal action against *S. aureus* and *E. coli* after only 1 h incubation, indicating strong synergistic effect of the polymer and the metallic component.

In perspective, hydrogel wound dressings generally are excellent alternatives for chronic wound treatments, and especially those based on PVA or chitosan. These materials have displayed exceptional tailorability of their mechanical, physico-chemical and biological properties that can be controlled by the addition of inorganic fillers such as graphene and silver nanoparticles. Importantly, hydrogels have exhibited the possibility for controlled and sustained release of the active antibacterial component, which could provide the necessary long-term infection protection to the wound area and suppress the dangerous biofilm formation. All in all, these materials show very attractive potential for wound dressing applications and next stage in research should be *in vivo* feasibility studies to confirm improvements in wound healing.

Acknowledgements: The authors thank the Ministry of Education, Science and Technological Development of the Republic of Serbia for funding.

REFERENCES

1. K. C. Broussard, J. G. Powers, *Am. J. Clin. Dermatol.*, **14**, 449 (2013).
2. J. S. Boateng, K. H. Matthews, H. N. E. Stevens, G. M. Eccleston, *J. Pharm. Sci.*, **97**, 2892 (2008).
3. J. G. Powers, L. M. Morton, T. J. Phillips, *Dermatol. Ther.*, **26**, 197 (2013).
4. E. A. Kamoun, E. R. S. Kenawy, X. Chen, *J. Adv. Res.*, **8**, 217 (2017).
5. S. R. Stauffer, N. A. Peppas, *Polymer.*, **33**, 3932 (1992).
6. F. Croisier, C. Jerome, *Eur. Polym. J.*, **49**, 780 (2013).
7. E. I. Rabea, M. E.-T. Badawy, C. V. Stevens, G. Smagghe, W. Steurbaut, *Biomacromolecules*, **4**, 1457 (2003).
8. S. Agnihotri, S. Mukherji, S. Mukherji, *Appl. Nanosci.*, **2**, 179 (2012).
9. Y. Murali Mohan, K. Lee, T. Premkumar, K. E. Geckeler, *Polymer*, **48**, 158 (2007).
10. D. Simões, S. P. Miguel, M. P. Ribeiro, P. Coutinho, A. G. Mendonça, I. J. Correia, *Eur. J. Pharm. Biopharm.*, **127**, 130 (2018).
11. N. Duran, M. Duran, M. B. de Jesus, A. B. Seabra, W. J. Favaro, G. Nakazato, *Nanomedicine Nanotechnology, Biol. Med.*, **12**, 789 (2016).
12. C. Liao, Y. Li, S. C. Tjong, *Int. J. Mol. Sci.*, **20**, 1 (2019).
13. K. Nešović, A. Janković, T. Radetić, M. Vukašinović-Sekulić, V. Kojić, L. Živković, A. Perić-Grujić, K. Y. Rhee, V. Mišković-Stanković, *Eur. Polym. J.*, **121**, 109257 (2019).
14. M. M. Abudabbus, I. Jevremović, K. Nešović, A. Perić-Grujić, K. Y. Rhee, V. Mišković-Stanković, *Compos. Part B Eng.*, **140**, 99 (2018).
15. K. Nešović, V. Kojić, K. Y. K. Y. Rhee, V. Mišković-Stanković, *Corrosion*, **73**, 1437 (2017).
16. S. F. Wang, L. Shen, W. De Zhang, Y. J. Tong, *Biomacromolecules*, **6**, 3067 (2005).
17. K. Nešović, A. Janković, A. Perić-Grujić, M. Vukašinović-Sekulić, T. Radetić, L. Živković, S. J. Park, K. Yop Rhee, V. Mišković-Stanković, *J. Ind. Eng. Chem.*, **77**, 83 (2019).
18. R. Surudžić, A. Janković, M. Mitrić, I. Matic, Z. D. Juranić, L. Živković, V. Mišković-Stanković, K. Y. Rhee, S. J. Park, D. Hui, *J. Ind. Eng. Chem.*, **34**, 250 (2016).
19. J. Guo, L. Ren, R. Wang, C. Zhang, Y. Yang, T. Liu, *Compos. Part B Eng.*, **42**, 2130 (2011).
20. J. H. Lee, J. Marroquin, K. Y. Rhee, S. J. Park, D. Hui, *Compos. Part B Eng.*, **45**, 682 (2013).
21. K. Geim, K. S. Novoselov, *Nat. Mater.*, **6**, 183 (2007).
22. H. Ji, H. Sun, X. Qu, *Adv. Drug Deliv. Rev.*, **105**, 176 (2016).
23. P. Avouris, *Nano Lett.*, **10**, 4285 (2010).
24. S. K. Behura, C. Wang, Y. Wen, V. Berry, *Nat. Photonics*, **13**, 312 (2019).
25. Y. Zhang, Y. An, L. Wu, H. Chen, Z. Li, H. Dou, V. Murugadoss, J. Fan, X. Zhang, X. Mai, Z. Guo, *J. Mater. Chem. A*, **7**, 19668 (2019).
26. C. Aphirakaramwong, N. Phattharasupakun, P. Suktha, A. Krittayavathananon, M. Sawangphruk, *J. Electrochem. Soc.*, **166**, A532 (2019).
27. S. K. Krishnan, E. Singh, P. Singh, M. Meyyappan, H. S. Nalwa, *RSC Adv.*, **9**, 8778 (2019).
28. L. Fan, J. Yi, J. Tong, X. Zhou, H. Ge, S. Zou, H. Wen, M. Nie, *Int. J. Biol. Macromol.*, **91**, 358 (2016).
29. S. Faghihi, M. Gheysour, A. Karimi, R. Salarian, *J. Appl. Phys.*, **115**, 083513 (2014).
30. S. R. ur Rehman, R. Augustine, A. A. Zahid, R. Ahmed, A. Hasan, *2019 41st Annu. Int. Conf. IEEE Eng. Med. Biol. Soc.*, 3943 (2019).
31. J. Lu, Y. S. He, C. Cheng, Y. Wang, L. Qiu, D. Li, D. Zou, *Adv. Funct. Mater.*, **23**, 3494 (2013).
32. N. H. Ali, M. C. I. M. Amin, S. F. Ng, *J. Biomater. Sci. Polym. Ed.*, **30**, 629 (2019).
33. Z. Fan, B. Liu, J. Wang, S. Zhang, Q. Lin, P. Gong, L. Ma, S. Yang, *Adv. Funct. Mater.*, **24**, 3933 (2014).
34. R. Ma, Y. Wang, H. Qi, C. Shi, G. Wei, L. Xiao, Z. Huang, S. Liu, H. Yu, C. Teng, H. Liu, V. Murugadoss, J. Zhang, Y. Wang, Z. Guo, *Compos. Part B Eng.*, **167**, 396 (2019).
35. S. Yang, X. Zhang, D. Zhang, *Int. J. Mol. Sci.*, **20**, 4395 (2019).
36. X. Y. Chen, H. R. Low, X. Y. Loi, L. Merel, M. A. Mohd Cairul Iqbal, *J. Biomed. Mater. Res. - Part B Appl. Biomater.*, **107**, 2140 (2019).
37. R. Surudžić, A. Janković, N. Bibić, M. Vukašinović-Sekulić, A. Perić-Grujić, V. Mišković-Stanković, S. J. Park, K. Y. Rhee, *Compos. Part B Eng.*, **85**, 102 (2016).
38. M. M. Abudabbus, I. Jevremović, A. Janković, A.

- Perić-Grujić, I. Matić, M. Vukašinović-Sekulić, D. Hui, K. Y. Rhee, V. Mišković-Stanković, *Compos. Part B Eng.*, **104**, 26 (2016).
39. K. Nešović, M. M. Abudabbus, K. Y. Rhee, V. Mišković-Stanković, *Croat. Chem. Acta*, **90**, 207 (2017).
40. K. Nešović, A. Janković, V. Kojić, M. Vukašinović-Sekulić, A. Perić-Grujić, K. Y. Rhee, V. Mišković-Stanković, *Compos. Part B Eng.*, **154**, 175 (2018).
41. K. Nešović, A. Janković, T. Radetić, A. Perić-Grujić, M. Vukašinović-Sekulić, V. Kojić, K. Y. Rhee, V. Miskovic-Stankovic, *J. Electrochem. Sci. Eng.*, **10** (2) 185 (2019).
42. G. Kapoor, S. Saigal, A. Elongavan, *J. Anaesthesiol. Clin. Pharmacol.*, **33**, 300 (2017).
43. S. Prabhu, E. K. Poulose, *Int. Nano Lett.*, **2**, 32 (2012).
44. J. R. Morones, J. L. Elechiguerra, A. Camacho, K. Holt, J. B. Kouri, J. T. Ram, M. J. Yacaman, *Nanotech*, **16**, 2346 (2005).
45. E. M. Luther, Y. Koehler, J. Diendorf, M. Epple, R. Dringen, *Nanotechnology*, **22**, 375101 (2011).
46. J. Stojkowska, D. Kostić, Ž. Jovanović, M. Vukašinović-Sekulić, V. Mišković-Stanković, B. Obradović, *Carbohydr. Polym.*, **111**, 305 (2014).
47. Z. Jovanovic, A. Radosavljevic, J. Stojkowska, B. Nikolic, B. Obradovic, Z. Kacarevic-Popovic, V. Miskovic-Stankovic, *Polym. Compos.*, **35**, 217 (2014).
48. J. Liu, L. Cui, N. Kong, C. J. Barrow, W. Yang, *Eur. Polym. J.*, **50**, 9 (2014).
49. O. J. Bothoko, S. S. Ray, J. Ramontja, *Eur. Polym. J.*, **102**, 130 (2018).
50. S. Shang, L. Gan, C. W. M. Yuen, S. X. Jiang, N. M. Luo, *Compos. Part A Appl. Sci. Manuf.*, **68**, 149 (2015).
51. J. Shen, M. Shi, N. Li, B. Yan, H. Ma, Y. Hu, M. Ye, *Nano Res.*, **3**, 339 (2010).
52. J. Ma, J. Zhang, Z. Xiong, Y. Yong, X. S. Zhao, *J. Mater. Chem.*, **21**, 3350 (2011).
53. Slistan-Grijalva, R. Herrera-Urbina, J. F. Rivas-Silva, M. Avalos-Borja, F. F. Castellon-Barraza, A. Posada-Amarillas, *Physica E*, **27**, 104 (2005).
54. X. Cai, M. Lin, S. Tan, W. Mai, Y. Zhang, Z. Liang, Z. Lin, X. Zhang, *Carbon*, **50**, 3407 (2012).
55. C. M. de Moraes, B. A. Lima, A. F. de Faria, M. Brocchi, O. L. Alves, *Int. J. Nanomedicine*, **10**, 6847 (2015).
56. M. Kozicki, M. Kołodziejczyk, M. Szykowska, A. Pawlaczyk, E. Leśniewska, A. Matusiak, A. Adamus, A. Karolczak, *Carbohydr. Polym.*, **140**, 74 (2016).
57. S. H. Lim, S. M. Hudson, *J. Macromol. Sci. - Polym. Rev.*, **43**, 223 (2003).
58. C. M. Santos, M. C. R. Tria, R. A. M. V. Vergara, F. Ahmed, R. C. Advincola, D. F. Rodrigues, *Chem. Commun.*, **47**, 8892 (2011).
59. T. Taylor, C. Unakal, Staphylococcus Aureus. [Updated 2019 Mar 27]. *StatPearls [Internet]. Treasure Isl. StatPearls Publ. 2019 Jan-*. Available from <https://www.ncbi.nlm.nih.gov/books/NBK441868> [Accessed 19.01.2020.], (2019).

Electroless copper-based layers deposition on anodized aluminum

V. S. Milusheva ^{*1,2}, B. R. Tzaneva ¹, M. Chr. Petrova ², B. I. Stefanov ¹

¹Department of Chemistry, Technical University of Sofia, 8 Kliment Ohridski Blvd., 1000 Sofia, Bulgaria

²Department of Electrochemistry and Corrosion, Institute of Physical Chemistry-Bulgarian Academy of Science, Acad. G. Bonchev Str., Blok 11, 1113 Sofia, Bulgaria

Received December 02, 2019; Accepted February 22, 2020

This work is an investigation on neutral electrolytes for electroless copper and copper (I) oxide plating of anodized aluminum. The plating electrolytes were based on copper (II) sulfate and phosphorous acid (H_3PO_3) as a reducing agent. It was investigated the influence of factors, such as Cu^{2+} concentration (0.024 – 0.048 mol/L) and pH (5 – 8) of the copper plating bath on the thickness, morphology and phase composition of the coatings, as well as kinetics of the electroless coating growth. The thickness and deposition rates of the coatings were determined gravimetrically and by X-ray fluorescence analysis. Electroless layer morphology was studied by optical and scanning electron microscopy. Crystallographic information and element composition depth profiles were examined by XRD and EDX analyzes respectively. Optimal deposition rates were achieved with electrolytes with Cu^{2+} concentration of 0.04 mol/L. Metallic copper layers were only formed at pH 5, while copper (I) oxide (Cu_2O) was formed at higher pH and the underlying mechanism was proposed.

Keywords: electroless deposition, copper, copper (I) oxide, anodic aluminum oxide

INTRODUCTION

Anodic aluminum oxide (AAO) has a variety of applications, e.g. in optics and electronic industry, where it is used as a dielectric layer in printed circuit boards (PCB) manufacturing. In this particular application it is also needed to create electrically conductive (usually copper-based) or semiconducting layers on the AAO surface [1-5]. Typically, this is achieved through vacuum technology, such as chemical or physical vapor deposition methods (CVD, PVD). These approaches, however, require expensive equipment and produce relative thin layers. An alternative approach allowing for fast deposition of metallic layers on dielectric surfaces is electroless deposition. This method has a number of advantages over vacuum methods. It is inexpensive and requires simpler equipment; allows for deposition on both conductive and non-conductive substrates; and uniform layers are obtained regardless of surface profile [6].

The electroless copper plating bath has two main components – a copper salt and a suitable reducing agent. Conventional

electrolytes for electroless copper deposition, however, can be aggressive towards AAO, which is unstable in highly acidic or alkaline solutions, as well as when chloride ions are present in the solution [7]. Usually formaldehyde, or formaldehyde-based derivatives, are used as a reducing agent for copper deposition [8, 9] and copper (I) oxide [10, 11], in order to achieve fast deposition rates and good mechanical stability of the as-prepared coatings. The catalytic oxidation rate of formaldehyde increases with hydroxide concentration and is most effective at $\text{pH} > 11$, thus making formaldehyde-based deposition chemistry unsuitable for metallization of AAO. There are a few examples of neutral electroless copper deposition electrolytes in the literature, which are still not used in practical applications [12, 13].

In this paper we present a novel electrolyte suitable for electroless copper deposition on AAO, employing phosphorous acid (H_3PO_3) as a reducing agent. Main focus of the study was investigating the effects of pH and Cu^{2+} ion concentrations on

* To whom all correspondence should be sent.

E-mail: v.milusheva@tu-sofia.bg

the deposition rate and morphology of the electroless deposited layers onto the AAO surface. This is a continuation of previous studies done in our group, where weakly alkaline electroless copper plating baths, based on sodium hypophosphite were employed on ABS and AAO substrates [14]. In this case it was observed the formation of copper (I) oxide on the AAO surface.

Copper (I) oxide (cuprous oxide, Cu_2O) is a n-type semiconductor with unique optical and electrical properties, which finds promising applications for solar energy conversion, photocatalytic oxidation, catalysis and sensors [15, 16]. It can also easily react with oxygen in moist atmosphere which implies promising applications in electrocatalytic applications, such as ORR [17, 18]. Yan et al [17] also show that the electrical conductivity of Cu_2O nanoparticles can be improved by the addition of highly conductive carbon-based materials, such as graphene.

EXPERIMENTAL

AAO samples 20x10 mm in dimensions were prepared by anodization of 100 μm thick Al-foil (99.0% purity). Prior anodization it was treated in 40 g/L NaOH solution. Anodization was carried using 20% H_2SO_4 electrolyte and a Voltcraft®4050 potentiostat set to 20V and current density up to 10 mA/cm^2 . Temperature was set to 15 $^\circ\text{C}$ and the duration of anodization was 100 min, resulting in an anodized layer of 12 μm . Active sites catalysing the electroless Cu deposition were created on the AAO surface by soaking the samples in Pd^{2+} solution.

The electrolytes for electroless copper deposition were based on phosphorous acid reducing agent and Cu^{2+} copper precursor salt. To study effects of Cu^{2+} concentration it was varied in the range 0.024 – 0.048 mol/L. The effect of pH was studied by adjusting the pH of the electrolyte in the range 5.0 – 8.0 with 10M NaOH. Details about the electrolyte composition and deposition conditions are listed in Table 1.

Copper-based coating thickness was determined employing X-Ray Fluorescence (XRF - Fischerscope HDAL) analysis and is noted as h_{XRF} . The obtained XRF results were compared with those determined

Table 1: Composition of electroless plating bath and summary of operating conditions for deposition on AAO

| Substances | Concentration (mol/L) |
|---|--------------------------|
| $\text{CuSO}_4 \cdot 5\text{H}_2\text{O}$ | 0.024 – 0.048 |
| $\text{H}_3\text{PO}_3 \cdot \text{H}_2\text{O}$ | 0.33 – 0.6 |
| $\text{Na}_3\text{C}_6\text{H}_5\text{O}_7 \cdot 5,5\text{H}_2\text{O}$ | 0.058 – 0.1 |
| H_3BO_3 | 0.56 – 1.00 |
| Operation conditions | |
| pH | 5.0 – 8.0 |
| Temperature, $^\circ\text{C}$ | 60 |

gravimetrically (h_{grav}) by weighing measurement the samples before and after the electroless deposition on an analytical scale (0.1 mg precision) and using Eq.1:

$$h_{\text{grav}} = \frac{\Delta m}{D \cdot S} \quad (1)$$

where Δm is the increase of samples mass due to the copper-based layer; D is the density of copper (8.96 g/cm^3) or of copper (I) oxide (6.0 g/cm^3); and S is the geometric area of the samples (4 cm^2).

Surface morphology of the copper-based layers was determined via optical microscopy (Optika XDS-3MET) and scanning electron microscopy (SEM, JEOL JSM 733) equipped with EDS detector (INKA). Crystallographic information was obtained by X-Ray Diffraction (XRD, PANanalytical Empyrean, Pixel 3D multichannel detector at Cu $K\alpha$) and diffractograms were obtained in the 10-100 $^\circ$ 2θ range, 0.01 $^\circ$ resolution.

RESULTS AND DISCUSSION

Influence of Cu^{2+} concentration on electroless deposition rates

The influence of increasing the Cu^{2+} concentration in the electroless deposition electrolytes is summarized as layer thickness values listed Table 2 (for 60 $^\circ\text{C}$ and pH 6.5). Data is presented for samples, where the deposition time was limited to 20 min. In the range 0.027 – 0.035 mol/L the XRF determined thickness increases linearly in the range 0.393 – 0.486 μm , which is the highest achievable thickness at these conditions. Increasing the Cu^{2+} concentration past 0.035 mol/L, and up to 0.048 mol/L, does not affect the kinetics of electroless deposition.

Optical microscopy observation of the electroless coated samples at x500

magnification show that at lower Cu^{2+} concentrations (0.027 mol/L) uneven coatings with uncoated areas were observed, while increasing the concentration to 0.035 mol/L the AAO surface was evenly coated within the same duration of electroless deposition (20 min). An attempt to improve the uniformity of the copper-based coating at lower Cu^{2+} concentrations (0.024 mol/L) was made by increasing the deposition bath temperature from 60 °C to 70 °C. In this case visible copper layer were obtained; however, the rate of deposition was unsatisfactory with only 0.2 μm being deposited within 1h (determined by XRF). Thus, it can be concluded that Cu^{2+} affects deposition rates more than temperature and the optimal conditions for electroless copper deposition in our case are: 60 °C and 0.04 mol/L Cu^{2+} concentration in the electrolyte.

Table 2. Thickness of the electroless copper-based layer (determined gravimetrically or via XRF), obtained for 20 min deposition time (pH 6.5, 60 °C) for several Cu^{2+} concentrations

| Cu^{2+} , mol/L | 0.027 | 0.030 | 0.035 | 0.040 | 0.048 |
|------------------------------------|-------|-------|-------|-------|-------|
| $h_{\text{grav.}}$, μm | 0.573 | 0.597 | 0.689 | 0.687 | 0.691 |
| h_{XRF} , μm | 0.393 | 0.424 | 0.486 | 0.436 | 0.449 |

Influence of pH on electroless deposition rates

The influence of pH of the electrolyte on the copper-based layer thickness and on the deposition rate was studied by comparing results at pH 5, pH 6.5 and pH 8 with a Cu^{2+} concentration of 0.04 mol/L. The results are summarized in Table 3 and Fig. 1 respectively.

Table 3. Time-dependence of the electroless Cu-based layer thickness (determined gravimetrically or via XRF) for different electroless copper plating bath pH

| Time of deposition, min | | 5 | 10 | 20 | 30 | 60 |
|-------------------------|------------------------------------|-------|-------|-------|-------|-------|
| pH=5.0 | h_{XRF} , μm | 0.055 | 0.069 | 0.154 | 0.105 | 0.067 |
| | $h_{\text{grav.}}$, μm | 0.303 | 0.585 | 0.687 | 1.250 | 1.476 |
| pH=6.5 | h_{XRF} , μm | 0.167 | 0.310 | 0.451 | 0.619 | 0.955 |
| | h_{XRF} , μm | 0.112 | 0.134 | 0.157 | 0.165 | 0.186 |

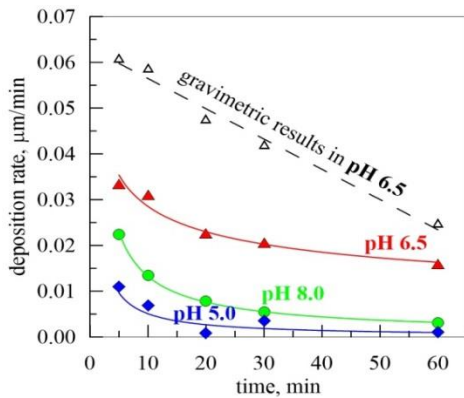


Fig. 1. Time-dependence of the deposition rate of the electroless copper-based layer (0.04 mol/L Cu^{2+} , pH 6.5, 60 °C) at pH 5.0, 6.5, and 8.5. As obtained by XRF (solid lines) and gravimetric (dashed line).

Visible layers with various colour were observed in all three cases, however, both increasing and decreasing the pH had a detrimental effect on its deposition rate. A maximum thickness of 1 μm was obtained in electrolyte with pH 6.5 after 60 min of

deposition. Thus, pH 6.5 was found to be the optimal condition.

According to XRF thickness results the rate deposition decrease flowing a power equation: $\ln(\text{rate})=a + b.\ln(\text{time})$

It can be observed that the copper-based layer grows rapidly during the first minutes of deposition, which is followed by a rapid decrease in deposition rate.

Morphology, composition and structure of deposited electroless copper layer

Figure 2 presents optical micrographs of the electroless deposited layers taken after 5, 10, 30, and 60 min. During the first 5 min finely dispersed crystalline nuclei were formed (Fig. 2a) with their density being the highest around irregularities and deep crevices on the anodized aluminum surface. This can be explained by a higher concentration of Pd-catalytic centers around these surface features and respectively higher rates of electroless deposition of

copper there. The number of copper nucleation sites increases during the first 10 min until the entire surface is coated, however their size remains constant until then (Fig. 2b). Crystalline growth of the copper nuclei is only observed after the surface is completely coated – then visible 3D crystals can be registered (Fig. 2c). This observation implies that the Pd catalytic centers exhibit higher activation to the phosphorous acid oxidation, compared to the autocatalytic effect on the reaction by the deposited copper-based layers. It also confirms our observation that the copper deposition rate progressively decreases proportionally with the area of uncoated AAO surface and inversely with increasing the amount of deposited crystals. After 1h, the AAO surface is completely coated with pyramidally shaped red-orange crystals. The initial morphology of the Al-foil surface, preserved after anodization, is still visible during the first 5 min, however it is completely masked by the electroless deposited layer afterwards. It can be concluded that the electroless copper-based deposition at pH 6.5 is completed in two stages – the first step being the formation of Cu nucleus on Pd catalytic centers and then – their growth after the catalytic surface is completely covered in copper compounds.

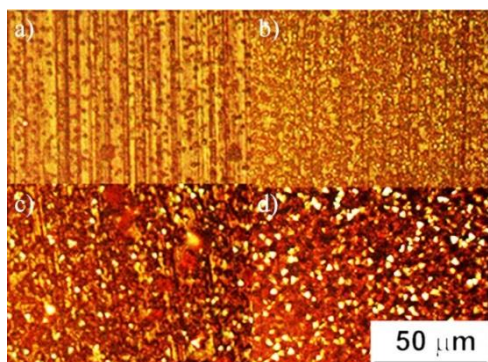


Fig. 2. Optical micrographs of electroless plated AAO (0.04 mol/L Cu^{2+} , pH 6.5, 60°C) at different time-frame, a) 5 min; b) 10 min; c) 30 min; d) 60 min

Figure 3 shows SEM micrographs of the surface morphology and cross-section of AAO after electroless deposition for 30 min (0.04 mol/L Cu^{2+} , pH 6.5). It can be seen clearly that the deposited layer consists of densely packed crystals with pyramidal

structure and relatively narrow size distribution 2÷4 μm , completely coating the AAO surface. The size uniformity of the features of the electroless-deposited layer confirms our expectations that the growth mechanism consists of two stages, as described in the paragraph above.

EDX data obtained at two points across the copper coating cross-section (Fig. 3b) shows that copper completely penetrates the AAO layer down to the pores bottom. The results for elemental composition measured by EDX throughout the entire 12 μm AAO pore depth are presented in Fig. 3b in wt.%. Negligible amounts of phosphorus (0.15 wt.%) was detected only in one of EDX measurements and suggests that its presence is only due to surface adsorption of the reducing agent (H_3PO_3), rather than chemical binding inside the copper layer during its deposition.

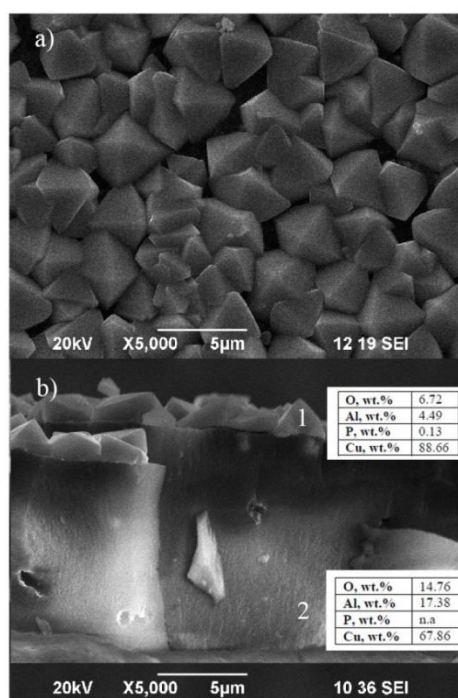


Fig. 3. SEM images of electroless deposited copper (I) oxide on AAO for 30 min at pH 6.5: (a) top and (b) cross-section view.

Figure 4 shows XRD diffraction patterns of electroless deposited layers by the $\text{Cu}^{2+}/\text{H}_3\text{PO}_3$ electrolyte at pH 5, 6.5, and 8. Metallic copper was only formed at pH 5, as shown by its characteristic diffraction peaks at 2θ 43.3°, 50.3°, and 74.2°. The peaks are

very weak and indicative of cubic copper crystals in various crystallographic orientations [18].

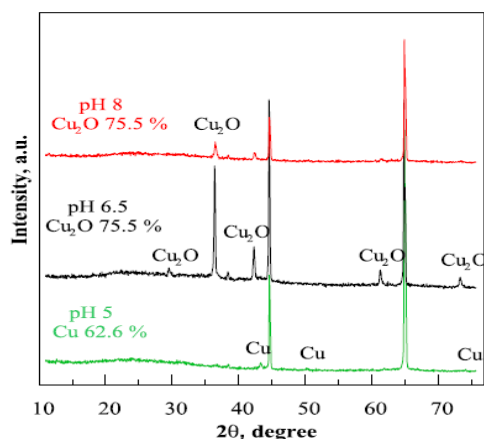
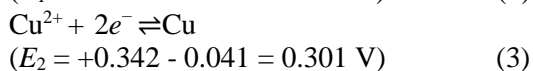
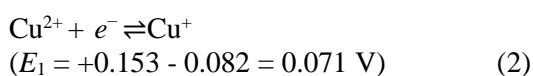


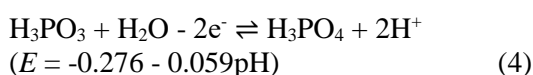
Fig. 4. XRD pattern of electroless copper-based layers grown on anodic aluminum oxide at pH 5.0, 6.5 and 8.0

At higher pH 6.5 and 8.0 new diffraction peaks are observed at 2θ 29.6°, 36.6°, 42.3°, 61.3° and 73.5°, which suggest the formation of Cu_2O . Similar results are found in the literature. According to Kobayashi et al [19] these peaks correspond to cubic Cu_2O . The highest intensity of the Cu_2O peaks is obtained at pH 6.5, suggesting also highest crystallinity at this condition. Therefore, in tables 2 and 3 the thickness of the deposited layers at pH 6.5 was calculated gravimetrically h_{grav} considering only the presence of copper (I) oxide.

At Cu^{2+} concentration of 0.04 mol/L, which was determined to be optimal for the highest rate of electroless layer deposition the reduction potentials for Cu^{2+} should be more negative than [20]:

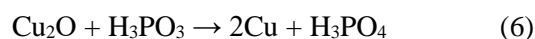
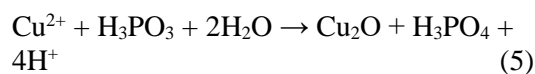


The oxidation potential of phosphorous acid (H_3PO_3) to phosphoric acid (H_3PO_4) is pH dependent [21]:

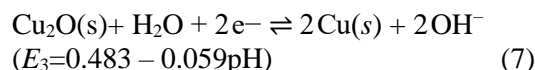


While sufficient to reduce Cu^{2+} through both pathways, (2) and (3), the complete reduction should be favoured, however, it is only observed at pH 5 in our experiments. Nevertheless, according to the Pourbaix

diagram of the process, when $\text{pH} > 5$ the Cu_2O formation reaction will be favoured. Hence, we can assume that the reduction of Cu^{2+} by H_3PO_3 goes according to the following two-step mechanism:



In the pH interval 5 – 12 the reduction potential for $\text{Cu}_2\text{O}/\text{Cu}$ is:



It is also pH dependent and the slope of the equation (7) is the same as the one for the H_3PO_3 oxidation (equation 4). Therefore, at pH 6.5 the reduction potential of Cu_2O and the oxidation potential of H_3PO_3 are 0.0997 and -0.6595 V vs. SHE, respectively. XRD data, however, suggests that reaction (6) has a negligible yield in our case and the process stops at Cu_2O .

According to Zhang et al [21] the morphology of the Cu_2O layer prepared by electroless deposition is determined by the deposition bath temperature. At 50 °C octahedral crystals are observed ca. 110 nm in diameter. In their publication TEM analysis is also made showing crystallographic growth favouring the formation of {111} facets [22].

CONCLUSIONS

We present a study on the electroless deposition of copper-based layers onto anodic aluminium oxide (AAO) surface. The deposition was achieved by using pH neutral electrolyte (pH 5 – 8) compatible with AAO. The effect of pH and Cu^{2+} ion concentrations was investigated in order to achieve optimal deposition rates and phase composition. The optimal deposition rate was achieved at Cu^{2+} concentration of 0.04 mol/L, pH 6.5, and 60°C temperature, where uniform cubic copper (I) oxide crystals were obtained on the entire surface of the AAO substrate. It was found that adjusting the pH affects the phase composition of the deposited copper layer, leading to formation of metallic copper at pH 5 and predominantly Cu_2O at $\text{pH} > 5$.

Acknowledgements: This research has been carried out within the project KII 06-H29/1

“Functional nanocomposite layers based on anodic aluminium oxide and its metallization” funded by the National Science Found (Bulgaria).

REFERENCES

1. Ch.-W. Hsu, Zh.-D. Chou, and G.-J. Wang, *J. Microelectromechanical systems*, **19**, 849 (2010).
2. S. Thongmee, H.L. Pang, J. Ding, J.B. Yi, J.Y. Lin, Proc 2th IEEE International Nanoelectronics Conference (INEC 2008) (2008), p.1116.
3. J. Cui, Y. Wu, Y. Wang, H. Zheng, G. Xu, X. Zhang, *Appl. Surf. Sci.*, **258**, 5305 (2012).
4. G.D. Sulka, A. Brzozka, L. Zaraska, M. Jaskula, *Electrochim. Acta*, **55**, 4368 (2010).
5. Ch. Hong, L. Chu, W. Lai, A.-Sh. Chiang, W. Fang, *IEEE Sensors journal*, **11**, 3409 (2011).
6. Ch. Decker, *Plating & Surface Finishing*, **82**, 48 (1995).
7. B.R. Tzaneva, *Bulg. J. Chem.* **2**, 61 (2013).
8. M. Georgieva, G. Avdeev, D. Stoychev, M. Petrova, *Transactions of the IMF*, **93**, 97 (2015).
9. S. Nakahara, Y. Okinaka, H. Straschil, *J. Electrochem. Soc.*, **136**, 1120 (1989).
10. K. Phasuksom, W. Prissanaroon-Ouajai, N. Brack, P. Pigram, *Adv. Mater. Research*, **802**, 262 (2013).
11. M.D. Susman, Y. Feldman, A. Vaskevich, I. Rubinstein, *ACS Nano*, **8**, 162 (2014).
12. Q. Li, P. Xu, B. Zhang, H. Tsai, S. Zheng, G. Wu, H.L. Wang, *J. Phys. Chem. C*, **117**, 13872 (2013).
13. F. Matsui, Y. Yamamoto, *US Patent* 5 298 058 (1994).
14. V. Milusheva, M. Georgieva, B. Tzaneva, M. Petrova, Proc. of IEEE XXVII International Scientific Conference Electronics - ET, Sozopol, Bulgaria, 2018, p. 1 (DOI 10.1109/ET.2018.8549651).
15. M. Wang, J. Huang, Z. Tong, W. Li, J. Chen, *J. Alloys Compd*, **568**, 26 (2013).
16. S. Deng, V. Tjoa, H.M. Fan, H.R. Tan, D.C. Sayle, M. Olivo, S. Mhaisalkar, J. Wei, C.H. Sow, *J. Am. Chem. Soc.*, **134**, 4905 (2012).
17. X. Y. Yan, X. L. Tong, Y. F. Zhang, X. D. Han, Y. Y. Wang, G. Q. Jin, Y. Qin, X. Y. Guo, *Chem. Commun.*, **48**, 1892 (2012).
18. JCPDS: 4-0836
- 19 Y. Kobayashi, Y. Abe, T. Maeda, Y. Yasuda, T. Morita, *J. Mater. Res. Technol.*, **3**, 114 (2014).
20. P. Vanýsek "Electrochemical Series" in: Chemistry and Physics: 93rd Edition, W.M. Haynes (ed.), CRC press, Taylor&Francis Group, New York, 2012, p. 5.
21. N. Koura, in: Electroless Plating: Fundamentals and Applications: G. O. Mallory, J. B. Hajdu (eds.), William Andrew, Orlando, 1990, p. 448.
22. X. Zhang, Y. Zhang, H. Huang, J. Cai, K. Ding, S. Lin, *New Journal of Chemistry*, **42**, 458 (2018).

Electrophoretic deposition of boehmite particles to improve the anti-corrosion behavior of anodized aluminum alloy 2024-T3

Florent Caubert¹, Pierre-Louis Taberna¹, Laurent Arurault^{1*}, Benoît Fori²

¹*CIRIMAT, Université de Toulouse, CNRS, UT3 Paul Sabatier, Bât. CIRIMAT, 118 route de Narbonne, 31062 Toulouse cedex 9, France*

²*Mécaprotec Industries, 34 Boulevard Joffrery, 31605 Muret Cedex, France*

Received December 11, 2019; Accepted January 27, 2020

The purpose of this study was to prepare and evaluate a new two-step sealing process for a porous and tortuous anodic film, prepared on aluminum alloy (AA) 2024-T3, to ensure anti-corrosion properties. This process involves a cathodic electrophoretic deposition of boehmite particles, followed by a hydrothermal post-treatment. This two-step sealing was evaluated through three industrial tests (dye-spot, continuity and salt spray) and the low frequency resistance. Such sealing of the anodic film on AA 2024-T3 showed promising anti-corrosion behavior, suggesting a real potential interest of this innovative process for future industrial applications.

Keywords: Aluminum, porous anodic film, boehmite particles, electrophoretic deposition, hydrothermal post-treatment, sealing

INTRODUCTION

Due to their good mechanical properties and low density, aluminum alloys (AA), are intensively used in the aircraft industry [1,2], as with AA 2XXX (Al-Cu) or 7XXX (Al-Zn). However, Al-Cu alloys, for instance AA 2024, show a low corrosion resistance [3,4]. They therefore require an additional corrosion protection, usually obtained by (electro) chemical processes (i.e. typically anodizing and sealing), usually involving chemical solutions including hexavalent chromium-based compounds. Such compounds are known to be classified as being both highly toxic and carcinogenic and their use is limited by recently adopted European standards (REACH). So, to protect AA 2024 for instance, new alternatives have been studied and developed, such as new anti-corrosion coatings prepared via the sol-gel route [5], with corrosion inhibitors [6-10], as well as new green sealing of anodic films [11,12]. Electrophoretic deposition (EPD) of nanoparticles, from organic or aqueous media, could provide an interesting alternative since it is simple and cheap. In this process, particles migrate under the influence of an electric field and are deposited onto an electrode [13,14]. Organic media are usually used [15,16] due to their wide voltage range of electrochemical stability. For instance, Fori et al. [17,18] successfully filled a porous anodic film prepared on AA 1050 using SiO₂ nanoparticles dispersed in an isopropyl alcohol solution. But, for environmental reasons, the aqueous medium

appears to offer a good alternative to avoid pollution. Despite a limited cell voltage due to water electrolysis, some previous studies [19-21] showed a significant incorporation of nanoparticles (SiO₂ and PTFE and AlOOH respectively) inside porous anodic films prepared on aluminum substrates. However, these results were obtained on pure aluminum substrates (99.99 % and 99.5 %) with anodic films showing straight pores, contrary to the tortuous porosity obtained when AA 2024 is anodized. Moreover, in previous studies [19-21], phosphoric acid-based electrolytes are used to perform anodizing to obtain the largest main pore diameter. However, the usual hydrothermal sealing of such anodic films prepared in phosphoric acid-based electrolyte is problematic [22] as compared with other types of anodic films.

There are now two main challenges:

- the first is to deposit nanoparticles on, and ideally in, the tortuous anodic film prepared on AA 2024 substrate,

- the second is to study a new process to seal the anodic film prepared in phosphoric acid-based electrolyte.

The present work aimed to develop a two-step sealing process for a tortuous anodic film prepared by anodizing of AA 2024-T3 in a phosphoric acid electrolyte. This sealing is implemented by direct electrophoretic deposition of boehmite nanoparticles dispersed in an aqueous solution on/into a tortuous anodic film, followed by a hydrothermal treatment. The resulting coatings are then characterized by FEG-SEM observations, and

* To whom all correspondence should be sent.

E-mail: arurault@chimie.ups-tlse.fr

evaluated through the low frequency resistance (50 mHz) – a good approximation of the polarisation resistance –, as well as using three standard industrial tests, i.e. salt spray, loss of absorptive power and continuity.

EXPERIMENTAL

Preparation

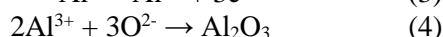
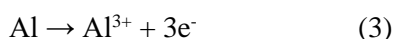
An aluminum alloy 2024-T3 substrate (compound of 4.5 % Cu, 1.5 % Mg, 0.6 % Mn, 0.2 % Fe, 0.08 % Zn, 0.06 % Si, 0.01 % Cr and 0.03 % Ti) was prepared following a three-step procedure (degreasing, etching and acid neutralization). Firstly, the aluminum sheet (20 x 20 x 1 mm or 80 x 1250 x 1 mm for industrial tests) was degreased using ethanol. The sample was then cleaned firstly in an alkaline aqueous solution (sodium triphosphate and borax) for 20 min at 60 °C (reaction 1).



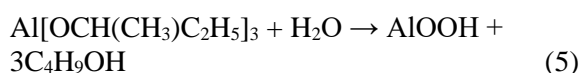
Secondly, sample was then immersed in a sulfonitro-ferric acidic solution for 5 min at room temperature (reaction 2).



After being rinsed in deionized water ($10^6 \Omega \cdot \text{cm}$), the aluminum sheet was used as an anode and a lead plate (50 x 40 x 2 mm) as a cathode. The specimen was anodized at constant voltage (70 V for 60 min) in a phosphoric bath (40 g.L⁻¹, i.e. 0.48 mol.L⁻¹) at 25 °C (reactions 3 and 4). Finally, the obtained anodic film was fully rinsed in deionized water.



The first step of the sealing process involved a constant cathodic electrophoretic deposition of boehmite particles dispersed in an aqueous solution. A colloid suspension of boehmite nanoparticles in aqueous media was initially synthesized. This suspension was prepared by hydrolysis of an aluminum alkoxide following the Yoldas process [23] (reaction 5).



An excess of deionized water ($\text{H}_2\text{O}/\text{Al} = 100$) at 85 °C was then immediately added to 25.3 g of aluminum tri-sec-butoxide ($\text{Al}(\text{OC}_4\text{H}_9)_3$) while stirring for 15 min. The white sol obtained was peptized by adding 0.2 mol of nitric acid (HNO_3) per mole of alkoxide to improve particle dispersion. The mixture was then continuously stirred at 85°C

for 24 h. The final concentration was around 0.5 mol.L⁻¹.

Electrophoretic impregnation of particles was then performed (10 V, 15 min) with the anodized aluminum substrate as the cathode, while a lead foil, located at about 2.5 cm from the cathode, was used as the anode. After being air dried for about 30min, a hydrothermal post-treatment (deionized water at 98 °C, 2 h) was performed as the second sealing step.

Characterizations and industrial tests

Surface and cross-sectional views of the coatings were performed using a Field Emission Gun Scanning Electron Microscope (FEG-SEM JEOL JSM 6700F).

The Stokes diameter of the nanoparticles and zeta potential of the particles were measured by Dynamic Light Scattering using a ZS90 Malvern nanosizer with zetasizer software.

The low frequency resistance (R_{LF}) of the samples was monitored for 240 h in a solution of NaCl (0.05 mol.L⁻¹) and Na₂SO₄ (0.5 mol.L⁻¹) at room temperature. A low concentration of chloride was chosen to limit the rapid corrosion attack, while sodium sulphate was chosen as a supporting electrolyte. A three-electrode electrochemical cell was used, with a platinum foil as a counter-electrode and a saturated calomel electrode as the reference electrode. The low frequency resistance was measured using an SP-150 BioLogic Science Instrument. It corresponds to the real part of the impedance measured at 50 mHz at open current potential; a RMS voltage amplitude of $\pm 50 \text{ mV}_{\text{eff}}$ was applied.

Loss of absorptive power of the anodic films was evaluated by a dye-spot test according to ISO 2143 standard, while their continuity was evaluated with an acidic copper solution according to NF A 91410 standard. Additionally, salt spray tests were conducted for 24 h, according to EN ISO 2143 standard.

RESULTS AND DISCUSSION

After anodizing

Characteristics of the bare anodic film

FEG-SEM views (Figure 1) show that the bare porous anodic film (i.e. before electrophoretic deposition) typically has a thickness of $1.2 \pm 0.3 \mu\text{m}$. Although this thickness is low, the continuity test is compliant (Table 1) and so attests that the resulting anodic film is homogeneous and evenly covers the whole metal substrate.

Table 1. Results of both industrial continuity and dye-spot tests

| Steps of the process | Dye-spot test | Continuity test |
|--|---------------|-----------------|
| Anodizing | Grade 2 | Conform |
| Anodizing + hydrothermal post-treatment | Grade 2 | Conform |
| Anodizing + constant EPD + hydrothermal post-treatment | Grade 0 | Conform |

FEG-SEM views (Figure 1) additionally show that the porosity is extremely tortuous, much more so than the porosity obtained using purer 1050 aluminum alloy, in agreement with previous studies [24,25]. Despite the real difficulty in distinguishing the pores, their average diameter was estimated to

be in the range of 30-50 nm. Unsurprisingly in this case, Grade 2 is obtained with a dye-spot test (Table 1), meaning that ink is impregnated into pores of the anodic film, indicating that the pores are not closed.

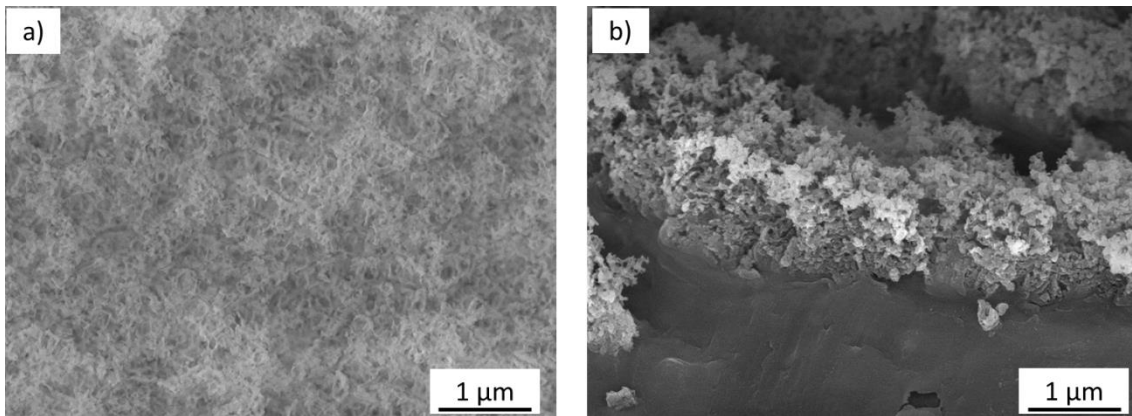


Fig. 1. FEG-SEM a) surface view and b) cross-sectional view of the bare porous anodic film, prepared (70V, 60 min, $[H_3PO_4]=40 \text{ g.L}^{-1}$, 25°C) on AA 2024-T3

Corrosion behavior of the bare anodic film

Evaluation of the low frequency resistance was then performed in a solution including NaCl (0.05 mol.L^{-1}) and Na_2SO_4 (0.5 mol.L^{-1}), as a function of the immersion time (Figure 2). In comparison with the raw substrate, the anodized substrate shows a high low frequency resistance (about $1 \times 10^5 \Omega.\text{cm}^2$) at the beginning of immersion ($t = 0 \text{ h}$), proving the positive intake of the anodic film against corrosion. However, its resistance decreases and reaches a minimum (at about $1 \times 10^3 \Omega.\text{cm}^2$) after 100 h of immersion (i.e. more than four days), meaning that the chloride corrosive ions penetrate through the barrier layer. This result is explained mainly by the opened pores and the thinness ($1.2 \pm 0.3 \mu\text{m}$) of the bare anodic film, especially its barrier layer (lower than 100 nm). After 100 h, the bare anodic film shows the same behavior as the substrate, corrosion being generalized and the anodic film failing to further protect the AA substrate.

After the two-step sealing process Characteristics of the sealed film

Diffusion Light Scattering analysis showed an average hydrodynamic diameter for the boehmite

particles equal to $35 \pm 15 \text{ nm}$, while from zeta potential measurement it came out at $+2.7 \times 10^{-4} \text{ cm}^2.\text{V}^{-1}.\text{s}^{-1}$ as particle electrophoretic mobility. This positive value shows that it is possible to perform a cathodic electrophoretic deposition (here at 10 V), thus avoiding any further oxidation of the metal substrate, i.e. electrodisolution or over-oxidation of the aluminum [26]

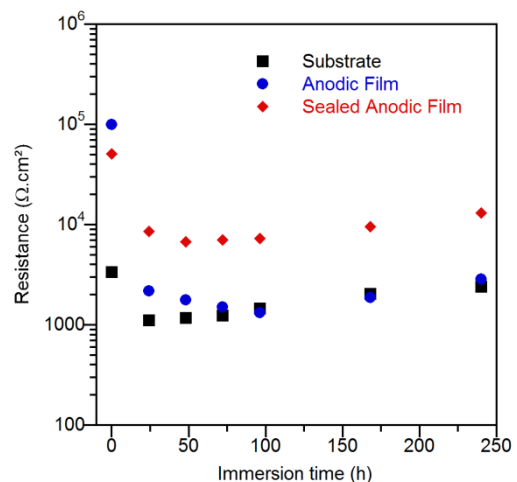


Fig. 2. Low frequency resistance values as a function of the immersion time

FEG-SEM views (Figure 3) show that electrophoresis alone induced a mainly top-surface deposit, although some of the smallest particles (about 20 nm) could be incorporated into the pores (30-50 nm).

The influence of the second sealing step, i.e. hydrothermal post-treatment (after the EPD), was then studied. FEG-SEM views (Figure 4) show complete sealing of the anodic film, both inside and on the top of the anodic film. On its top surface (Figure 4b), a typical “sand rose” structure is observed, attesting to the aluminum hydroxide formation. The continuity test gave a correct result (Table 1), meaning that the film is homogeneous and crack-free. In addition, after hydrothermal post-treatment, Grade 0 is obtained using the dye-spot test, since no color persists at the surface after removal of the dye-spot.

This result unambiguously proves that the pores are globally closed, in agreement with the FEG-SEM views (Figure 4).

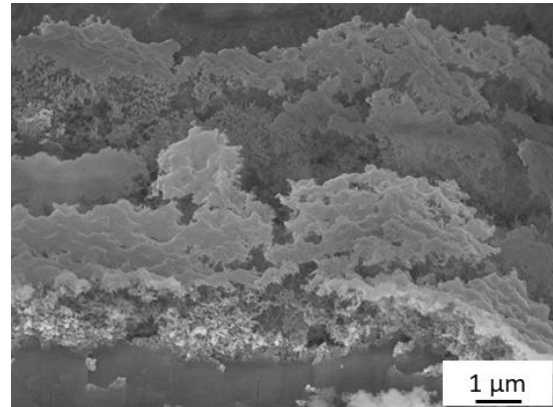


Fig. 3. FEG-SEM cross-sectional view of the anodic film after constant EPD (10 V, 15 min)

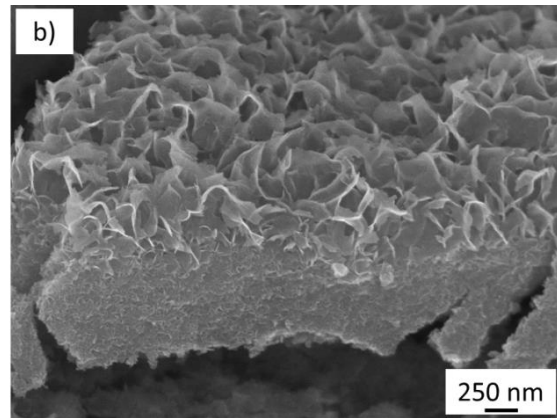
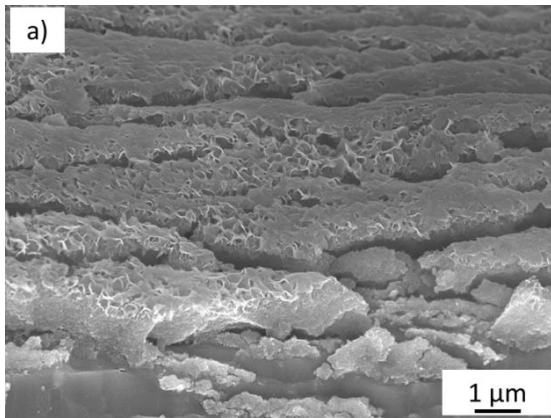


Fig. 4. FEG-SEM cross-sectional views of the anodic film after constant EPD (10 V, 15 min) followed by the hydrothermal post-treatment (deionized water at 98 °C, 2 h)

This result, i.e. complete sealing of the porosity, tends to prove either modification of particles on and inside the anodic film, or the film's transformation under hydrothermal conditions. To test these hypotheses, the same hydrothermal treatment was performed directly on the bare anodic film, i.e. without electrophoretic deposition. FEG-SEM views (Figure 5) show that no change can be observed in comparison with the bare anodic film (Figure 1). Moreover, while the industrial continuity test remains compliant (Table 1), grade 2 is again obtained with the industrial dye-spot test, proving that the pores are still partially unclosed following the hydrothermal treatment alone. Thus, in these conditions the usual hydrothermal sealing fails to occur, meaning there is no fast hydration of the pore walls of the bare anodic film. These results confirm the difficulty, for an anodic film prepared in phosphoric acid electrolyte, of sealing under the usual hydrothermal conditions [27]. This behavior can be explained by the incorporation of phosphate

ions into the anodic film during its formation, largely inhibiting the latter's hydration [22]. The phosphate ions are indeed incorporated into the film in the form of aluminum phosphate AlPO_4 [28,29], which is thermo-dynamically stable. Davis et al. [22] showed that the AlPO_4 top-layer slowly dissolves and that this dissolution is the rate-limiting step inducing greater hydration resistance and thus impeding rapid sealing of the anodic film pores. In all events, our results clearly show that the electrophoretic deposition of boehmite particles allows the complete sealing of the tortuous anodic film prepared in phosphoric acid electrolyte on AA 2024-T3 to be achieved. In this case, the electrophoretic process followed by a hydrothermal post-treatment could jointly accelerate aluminum phosphate dissolution, thus allowing the hydration of the pore walls from alumina (Al_2O_3) to boehmite (AlOOH) (at $T > 80^\circ\text{C}$) and subsequent interaction with the electrodeposited boehmite particles.

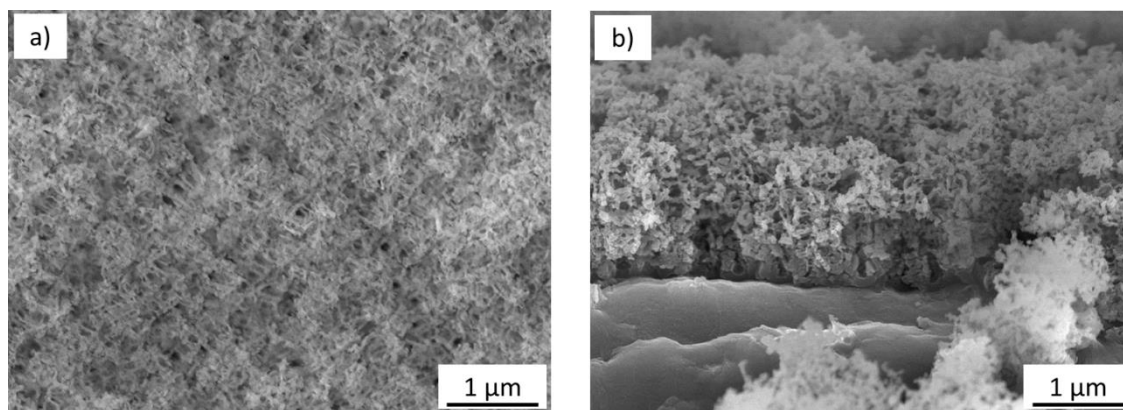


Fig. 5. FEG-SEM a) surface view and b) cross-sectional view of the anodic film after the hydrothermal post-treatment (deionized water at 98°C, 2h)

Corrosion behavior of the sealed film

Sealed film shows a similar behavior (Figure 2) compared with the bare anodized substrate for the first 50 h of immersion, with the low frequency resistance initially being high (about $5 \times 10^4 \Omega \cdot \text{cm}^2$). The R_{LF} of the sealed film then decreases but remains higher (about $8 \times 10^3 \Omega \cdot \text{cm}^2$) compared with the value obtained with the bare anodic film. After 50 h and up to 240 h (i.e. 10 days), the low frequency resistance of the sealed film slowly increases, significantly remaining higher than the value corresponding to the bare anodic film. Thus, this two-step sealing process clearly provides a barrier slowing down the penetration of corrosive species across the anodic film, and significantly improving the anti-corrosion behavior of AA 2024-T3.

Anodized samples with and without electrophoretic impregnation, but each time

followed by the same hydrothermal post-treatment, were then characterized using the salt spray test. Figure 6 shows photographs of samples after a salt spray exposure for 24 h. Anodized samples without impregnation and with hydrothermal post-treatment are completely corroded (Figure 6a), whereas anodized samples with impregnation and identical post-treatment show only a few pits (Figure 6b). These results clearly indicate that this two-step sealing process, including electrophoretic deposit before hydrothermal post-treatment, successfully improves corrosion resistance of anodized AA 2024-T3. However, corrosion performances still fail to meet industrial requirements from the duration point of view; although the process can advantageously replace currently used techniques, it still needs to be optimized.

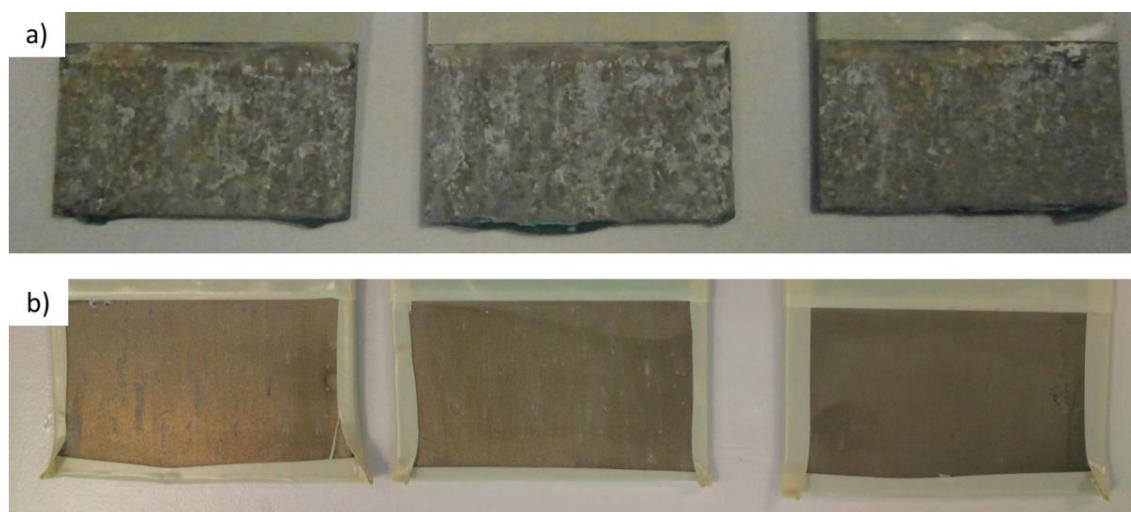


Fig. 6. After 24 h of salt-spray test, photographs of a) the anodic film after the hydrothermal post-treatment (deionized water at 98 °C, 2 h), and of b) the anodic film after constant EPD (10 V, 15 min) followed by the hydrothermal post-treatment

CONCLUSIONS

Anodizing of AA 2024-T3 was performed in phosphoric acid solution, with the resulting bare anodic film showing a low thickness ($1.2 \pm 0.3 \mu\text{m}$) and tortuous porosity. Despite these conditions, the bare anodic film, and especially its barrier layer, provides a first level of protection against corrosion. To boost this protection, a constant cathodic electrophoretic deposition of boehmite particles ($\varnothing_{\text{particles}} = 35 \pm 15 \text{ nm}$) dispersed in an aqueous media was conducted, with the resulting deposit being mainly located on the surface. The process was completed by a second step, i.e. an additional hydrothermal post-treatment allowing the anodic film to be completely sealed. Finally, low frequency resistance characterization and three additional tests highlight positive and promising performances against corrosion thanks to the two-step sealing process. The results still fail to meet industrial expectations but the future use of pulsed electrophoresis could possibly offer a promising optimization technique to improve incorporation of the boehmite particles within the tortuous anodic film and thus enhance its anti-corrosion protective behavior.

Acknowledgements: The present work was carried out as a part of the ECOREV project. The Regional Council of Midi-Pyrénées and Mecaprotec Industries are gratefully acknowledged for the financial support (No. 11052675) they provided for this project.

REFERENCES

1. A.S. Warren, Developments and challenges for Aluminum – a Boeing perspective, *Materials Forum.*, **28**, 24 (2004).
2. T. Dursun, C. Soutis, Recent developments in advanced aircraft aluminium alloys, *Materials and Design.*, **56**, 862 (2014).
3. F. Snogan, C. Blanc, G. Mankowski, N. Pèbère, Characterisation of sealed anodic films on 7050 T74 and 2214 T6 aluminium alloys, *Surf. Coat. Technol.*, **154**, 94 (2002).
4. M.C. Vasco, A.N. Chamos, Sp.G. Pantelakis, Effect of environment's aggressiveness on the corrosion damage evolution and mechanical behavior of AA 2024-T3, *Fatigue and Fracture of Engineering Materials and Structures.*, **40**, 1551 (2017).
5. M.L. Zheludkevich, R. Serra, M.F. Montemor, I.M. Miranda Salvado, M.G.S. Ferreira, Corrosion protective properties of nanostructured sol–gel hybrid coatings to AA2024-T3, *Surf. Coat. Technol.*, **200**, 3084 (2006).
6. M.L. Zheludkevich, R. Serra, M.F. Montemor, K.A. Yasakau, I.M.M. Miranda Salvado, M.G.S. Ferreira, Nanostructured sol–gel coatings doped with cerium nitrate as pre-treatments for AA2024-T3: Corrosion protection performance, *Electrochimica Acta.*, **51**, 208 (2005).
7. M. Schem, T. Schmidt, J. Gerwann, M. Wittmar, M. Veith, G.E. Thompson, I.S. Molchan, T. Hashimoto, P. Skeldon, A.R. Phani, S. Santucci, M.L. Zheludkevitch, CeO₂-filled sol–gel coatings for corrosion protection of AA2024-T3 aluminium alloy, *Corros. Sci.*, **51**, 2304 (2009).
8. N. Pirhady Tavandashti, S. Sanjabi, Corrosion study of hybrid sol–gel coatings containing boehmite nanoparticles loaded with cerium nitrate corrosion inhibitor, *Prog. Org. Coat.*, **69**, 384 (2010).
9. J.B. Cambon, J. Esteban, F. Ansart, J.P. Bonino, V. Turq, S.H. Santagneli, C.V. Santilli, S.H. Pulcinelli, Effect of cerium on structure modifications of a hybrid sol–gel coating, its mechanical properties and anti-corrosion behavior, *Mater. Res. Bull.*, **47**, 3170 (2012).
10. L.E. Morales Palomino, Z. Paszti, I. Vieira Aoki, H. Gomes de Melo, Comparative investigation of the adhesion of Ce conversion layers and silane layers to a AA 2024-T3 substrate through mechanical and electrochemical tests, *Materials Research.*, **10**(4), 399 (2007).
11. X. Yu, C. Cao, Electrochemical study of the corrosion behavior of Ce sealing of anodized 2024 aluminum alloy, *Thin Solid Films*, **423**, 252 (2003).
12. B. Priet, G. Odemer, C. Blanc, K. Giffard, L. Arurault, Effect of new sealing treatments on corrosion fatigue lifetime of anodized 2024 aluminium alloy, *Surface and Coatings Technology*, **307**, 206 (2016).
13. O. Van der Biest, L.J. Vandeperre, Electrophoretic Deposition of Materials, *Annu. Rev. Mater. Sci.*, **29**, 327 (1999).
14. L. Besra, M. Liu, A review on fundamentals and applications of electrophoretic deposition (EPD), *Prog. Mater. Sci.*, **52**, 1 (2007).
15. E. Antonelli, R. Santos da Silva, Electrophoretic deposition of BaTi_{0.85}Zr_{0.15}O₃ nanopowders, *Materials Research*, **16**(6), 1344 (2013).
16. R. Dula Corpuz, J. Rayala Albia, Electrophoresis fabrication of ZnO/ZnO–CuO composite for ammonia gas sensing, *Materials Research*, **17**(4), 851 (2014).
17. B. Fori, P.L. Taberna, L. Arurault, J.P. Bonino, C. Gazeau, P. Bares, Electrophoretic impregnation of porous anodic aluminum oxide film by silica nanoparticles, *Colloids Surf.A: Physicochem. Eng. Asp.*, **415**, 187 (2012).
18. B. Fori, P.L. Taberna, L. Arurault, J.P. Bonino, Decisive influence of colloidal suspension conductivity during electrophoretic impregnation of porous anodic film supported on 1050 aluminium substrate, *J. Colloid Interface Sci.*, **413**, 31 (2014).
19. K. Kusdianto, M. Nazli Naim, K. Sasaki, I. Wuled Lenggoro, Immobilization of colloidal particles into sub-100 nm porous structures by electrophoretic methods in aqueous media, *Colloids Surf. A: Physicochem. Eng. Asp.*, **459**, 142 (2014).

20. J. Escobar, L. Arurault, V. Turq, Improvement of the tribological behavior of PTFE-anodic film composites prepared on 1050 aluminum substrate, *Appl. Surf. Sci.*, **258**, 8199 (2012).
21. F. Caubert, P.L. Taberna, L. Arurault, Innovating pulsed electrophoretic deposition of boehmite nanoparticles dispersed in an aqueous solution, into a model porous anodic film, prepared on aluminium alloy 1050, *Surface and Coatings Technology*, **302**, 293 (2016).
22. G.D. Davis, T.S. Sun, J.S. Ahearn, J.D. Venables, Application of surface behaviour diagrams to the study of hydration of phosphoric acid-anodized aluminium, *J. Mater. Sci.*, **17**, 1807 (1982).
23. B.E. Yoldas, Alumina gels that form porous transparent Al₂O₃, *J. Mater. Sci.*, **10**, 1856 (1975).
24. J.P. Dasquet, D. Caillard, E. Conforto, J.P. Bonino, R. Bes, Investigation of the anodic oxide layer on 1050 and 2024T3 aluminium alloys by electron microscopy and electrochemical impedance spectroscopy, *Thin Solid Films*, 371, 183 (2000).
25. I. Pires, L. Quintino, R.M. Miranda, Performance of 2024-T3 Aluminium Adhesive Bonded Joints, *Mater. Manuf. Process.*, **20**, 175 (2005).
26. G. Zamora, L. Arurault, P. Winterton, R. Bes, Impact of the type of anodic film formed and deposition time on the characteristics of porous anodic aluminum oxide films containing Ni metal, *Chem. Pap.*, **65**(4), 460 (2011).
27. J.W. Diggle, T.C. Downie, C.W. Goulding, Anodic oxide films on aluminum, *Chem. Rev.*, **69**, 365 (1969).
28. F. Le Coz, L. Arurault, S. Fontorbes, V. Vilar, L. Datas, P. Winterton, Chemical composition and structural changes of porous templates obtained by anodising aluminium in phosphoric acid electrolyte, *Surface and Interface Analysis*, **42**, 227 (2010).
29. F. Le Coz, L. Arurault, L. Datas, Chemical analysis of a single basic cell of porous anodic aluminium oxide templates, *Materials Characterization*, **61**, 283 (2010).

Investigation of the structure of copper coatings obtained by chemical deposition from formaldehyde-free solution on dielectrics

M. Georgieva^{1,2*}, G. Avdeev², V. Milusheva^{1,2}, D. Lazarova², M. Petrova²

¹ *Bulgaria1 Technical University of Sofia, Sofia 1797, 8 "Kl. Ohridski" bul*

² *Institute of Physical Chemistry – Bulgarian Academy of Sciences, Acad. G. Bonchev Str., Blok 11, 1113 Sofia, Bulgaria*

Received December 03, 2019; Accepted January 09, 2020

Copper coatings are obtained by chemical deposition from formaldehyde-free, weakly alkaline copper plating bath, which is non-toxic and non-aggressive to a large part of the dielectrics. The present paper reports the results from investigations of the morphology, microstructure and micro-texture of the copper coatings. The influence of the concentration of Cu^{2+} ions and reducing agent ($\text{NaH}_2\text{PO}_2 \cdot \text{H}_2\text{O}$) as well as pH, temperature and deposition time on the thickness of the copper coatings is studied. The chemical composition of the coatings is defined using EDS analysis. The thickness of the copper coatings is determined by XRF analysis. Morphology of the coatings is examined by scanning electron (SEM) and optical microscopy. The obtained copper coatings could find application as layers on metal and non-metal samples, in the production of new materials for the electronics, energetics, fine mechanics, optics and printed circuit boards with covered holes.

Keywords: chemical deposition, copper coatings, formaldehyde-free, weakly alkaline solution, microstructure, dielectrics

INTRODUCTION

Chemical copper plating is widely used for deposition of copper layers on various dielectric materials and semiconductors in order to obtain decorative and functional properties. The copper coatings are widely used in electronics for formation of conductive images or opening holes in the production of printed circuit boards and integrated circuits [1-5]. Formaldehyde or its derivatives are traditionally used reducing agents in solutions for chemical copper deposition because of the excellent mechanical properties of the deposited copper coatings and their high deposition rate [6, 7]. Unfortunately, these solutions exhibit some disadvantages [8, 9]. One of them is that the catalytic oxidation of the formaldehyde increases with increasing hydroxide concentration and by this reason, these solutions are effective at pH above 11. However, the high pH is incompatible with some dielectric materials and photo-resists used in the photolithography processes. For this reason, the research in this topic is focused at development chemical copper solutions that do not contain formaldehyde or its derivatives [10-14]. Alternative reducing agents are proposed as follows: borohydride [15], Co (II) [16], sodium hypophosphite [17-22] and others. Among them, sodium hypophosphite is an attractive reducing agent because the final solutions are relatively inexpensive and safe to use. However, sodium hypophosphite is widely used as a reducing agent in

the chemical deposition of some metals such as nickel or cobalt, but not in copper deposition. The reason is that its reducing ability is not catalyzed by the copper [16-19]. A way to compensate the poor catalytic activity of copper is to add nickel ions to the solution. As a result, a joint deposition of the both metals occur with a minimum amount of nickel into the copper coating. The role of the nickel is to catalyze the oxidation of sodium hypophosphite and to maintain the continuous deposition of copper, depending on the molar ratio of $\text{Ni}^{2+}/\text{Cu}^{2+}$ [23].

The deposition of copper layers from such solutions is well discussed in the literature, however there is no detailed studies on the influence of working conditions and the major components of the solution on their morphology.

The purpose of the present work is to investigate the process of chemical copper deposition from formaldehyde-free copper bath with reduced alkalinity. Sodium hypophosphite is used as a reducing agent in the copper bath. The influence of its concentration, the concentration of copper ions in the solution, pH, temperature and duration of deposition on the morphology, microstructure and micro-texture of chemically deposited copper coatings is studied. The optimal conditions for use of this non-toxic and slightly aggressive copper bath are established.

EXPERIMENTAL

Novodur PM/2C type ABS (Acrylonitrile-

* To whom all correspondence should be sent.

E-mail: mggeorgieva@tu-sofia.bg

butadiene-styrene, manufactured by Bayer, Germany) sample with an area of 0.1 dm² was used as substrate. Before deposition, the ABS substrates were preliminary treated by using the technological scheme shown in Fig. 1 [24-25].

The electroless copper plating solution used was with the following composition: CuSO₄·5H₂O as copper ion source and sodium hypophosphite as reducing agent. Their concentrations were varied within the limits according to Table 1. In addition, the following compounds were added to the solution: sodium citrate (16 g L⁻¹) as

The diffraction patterns of the samples were recorded on multipurpose diffractometer system Epyrean (PANalytical) equipped with a multichannel detector (Pixel 3D), Cu anode and operated at 45kV-40mA. Phase analysis and calculation of the crystallites size and micro strains were performed in HighScore (Plus) software version 4.5 (2016), by PANalytical B.V., Almelo,

The Netherlands. The morphology of the coatings was defined by Scanning Electron Microscopy (SEM, JEOL JSM 733, Japan) images. The elemental composition was analyzed by Energy Dispersive Spectroscopy (EDS) /INCA/. The surface roughness of the ABS details was measured by AFM analysis (Nano Scope V system - Bruker Ltd, Germany).

RESULTS AND DISCUSSION

1. X-ray structural studies

The obtaining of chemically deposited copper coatings with certain physical-mechanical properties, such as fine dispersion, hardness, elasticity, internal tensions, etc., depends on their crystal structure. In this regard, in order to identify the factors that influence these properties, it is important to carry out systematic studies of the shape, location, size of the grains and their preferential orientation, depending on

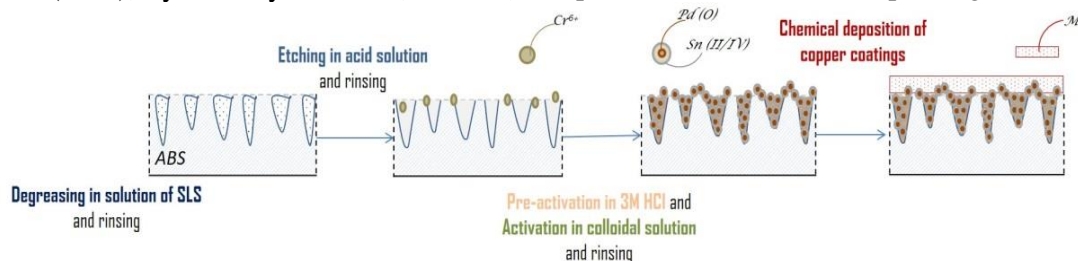


Fig. 1. Technological scheme for preliminary treatment of ABS substrates

complexing agent and boric acid (30 g L⁻¹) as buffer solution. The pH was adjusted using 10M NaOH or H₂SO₄ to a final value of 8.0 to 10.0. The temperature was kept in the range of 50 to 70 °C, and the deposition time was in limits from 5 to 30 min. The plating was performed in 250 ml electroless copper solution with continuous stirring.

The thickness of the copper coatings is determined by XRF analysis (XRF - Fischerscope HDAL). The microstructural parameters of the copper deposits were investigated using X-ray diffraction (XRD), the conditions of chemical deposition of the copper layers. In literature, information about such studies is useful but rather poor [26-27].

In order to identify the relationship between the deposition conditions and the structural characteristics of the layers obtained, a full-profile fitting method was used. The diffraction patterns of the samples were recorded in an appropriate mode in order to determine the parameters of the lattice, the average crystallites size and the strains after each change in the solution composition and the deposition regime. The Maud [28-31] and HighScore plus 4.5 [32] programs were used

independently for the calculations. When layers with small thicknesses (small amounts of irradiated volume) were used, only one well-expressed peak of the copper was most commonly observed on the diffraction patterns. Therefore, the data of the lattice parameters and the average crystallites size were calculated only on the basis of this peak. For size-strain standard were used LaB6 and SRM 660c.

The effect of the following factors on the structure and on the thickness of the layers obtained was studied: concentration of Cu²⁺-ions, concentration of the reducing agent (NaH₂PO₂·H₂O), pH, temperature and deposition time. The data are shown in Table 1.

The data for the imperfection of the coatings due to the accumulation of various defects (twins-, points- and linears-) are expressed as strains in percentages and they are obtained using the profile fitting of the diffraction lines.

1.1. Effect of the concentration of Cu²⁺-ions in the solution

In Fig. 2a, the diffraction patterns of deposited copper layers at different concentrations of Cu²⁺-ions in the solution are presented, based on which

in Table 1 the microstructural parameters are determined.

As it is obvious from the data shown in Fig. 2a and Table 1, changing the concentration of copper sulfate in the range from 1 to 10 g L⁻¹ and

maintaining the ratio between the other components leads to an increase in the size of the elementary building blocks of the copper coating and to an acceleration of its growth.

Table 1: Dependence of the microstructural parameters and the thickness of the copper coating on the concentration of Cu²⁺-ions and the reducing agent in the solution, the temperature, the pH and the deposition time

| | Lattice parameter <i>a</i> , [Å] | Crystallite size <i>D</i> , [nm] | Micro Strain <i>ms</i> , [%] | Thickness of the copper coatings <i>δ</i> , [μm] |
|---|--|----------------------------------|------------------------------|--|
| Concentration of CuSO₄·5H₂O, g L⁻¹ (first column) | | | | |
| 1 | 3.6216(4) | 10,1 | 0.936(3) | 1.16 |
| 10 | 3.6188(3) | 65,4 | 0.192(2) | 1.93 |
| 30 | 3.6177(2) | 43,8 | 0.262(4) | 0.62 |
| 50 | Coating consisting most probably of a mixture of Cu ₂ O and CuO | | | 0.63 |
| Concentration of NaH₂PO₂·H₂O, g L⁻¹ (first column) | | | | |
| 1 | An amorphous coating consisting most probably of copper | | | 0.33 |
| 10 | An amorphous coating consisting most probably of a mixture of Cu and Cu(OH) ₂ | | | 0.39 |
| 30 | 3.6188(3) | 65,4 | 0.192(2) | 1.93 |
| 50 | 3.6193(5) | 18,2 | 0.044(5) | 0.59 |
| pH of the solution (first column) | | | | |
| 8.0 | 3.6059(3) | 14,9 | -0.067(1) | 0.37 |
| 8.5 | 3.6140(4) | 20,3 | -0.068(2) | 0.78 |
| 9.0-9.3 | 3.6188(3) | 65,4 | 0.192(2) | 1.93 |
| 9.5 | 3.6142(2) | 25,1 | -0.063(4) | 1.27 |
| 10.0 | 3.6154(3) | 75,9 | 0.147(3) | 1.25 |
| Temperature of the solution, °C (first column) | | | | |
| 50 | 3.6241(2) | 9,2 | 0.066(3) | 0.51 |
| 60 | 3.6098(2) | 19,5 | 0.134(4) | 0.57 |
| 70 | 3.6188(3) | 65,4 | 0.192(2) | 1.93 |
| 80 | 3.6081(3) | 26,3 | 0.266(5) | 0.54 |
| Deposition time, min (first column) | | | | |
| 5 | 3.6201(4) | 42,0 | 0.142(3) | 0.70 |
| 10 | 3.6146(2) | 24,2 | 0.131(2) | 0.71 |
| 20 | 3.6188(3) | 65,4 | 0.192(2) | 1.93 |
| 30 | 3.6107(2) | 18,6 | 0.257(4) | 0.82 |
| Air stirring of the solution (first column) | | | | |
| Without | 2.0974(2) | 65,3 | 0.193(4) | 0.59 |
| With | 3.6188(3) | 65,4 | 0.192(2) | 1.93 |

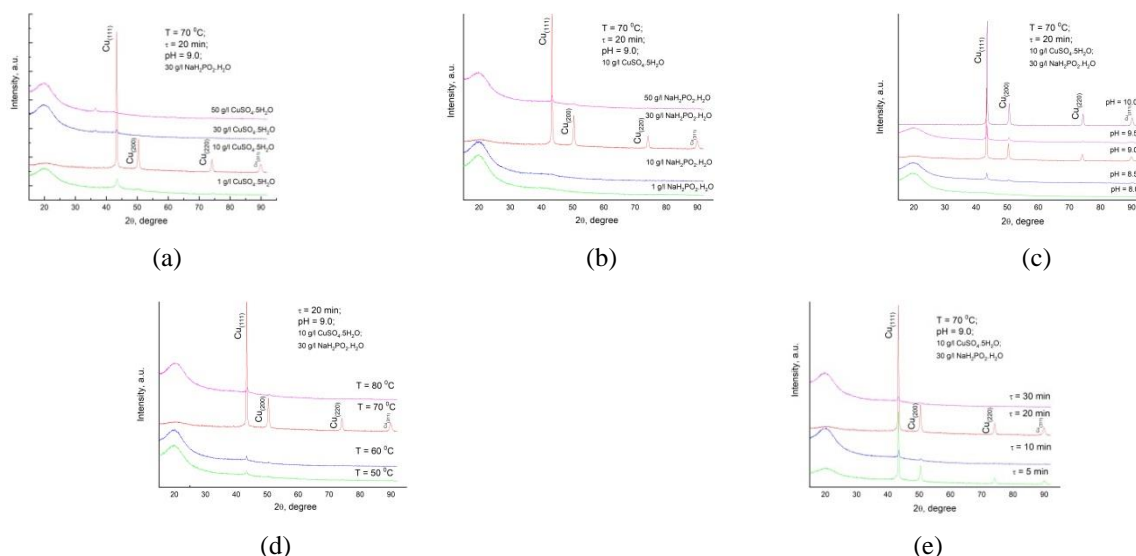


Fig. 2: XRD-pattern obtained at different: a) concentrations of copper sulfate in the solution; b) concentrations of sodium hypophosphite in the solution; c) pH values of the copper solution; d) temperatures of the solution; e) deposition times.

The change in the concentration of copper sulfate in this range also leads to an increase of the size of the crystallites, as well as to an around three-fold increase in the thickness of the coating. The internal strains in the coating increase in proportion to the increasing concentration of the copper ions. Further increase in the concentration of the basic salt to above 10 g L^{-1} leads to a significant decrease in the thickness of the coatings, and at 50 g L^{-1} , a coating, most probably consisting of a mixture of Cu_2O and CuO , is even observed. The results reveal that the deposition process is limited primarily by the diffusion of the copper ions, respectively complexes, and a concentration of 10 g L^{-1} of copper sulfate can be considered optimal (all subsequent studies have been conducted with this concentration).

1.2. Influence of the concentration of the reducing agent (sodium hypophosphite) in the solution

In Fig. 2b, the diffraction patterns of deposited copper layers are shown. They are obtained by varying the concentration of the reducing agent ($\text{NaH}_2\text{PO}_2 \cdot \text{H}_2\text{O}$) in the solution and keeping the ratio between the other components. The data for the microstructural parameters are summarized in Table 1.

The analysis of the obtained data shows that as the concentration of $\text{NaH}_2\text{PO}_2 \cdot \text{H}_2\text{O}$ in the solution increases to 30 g L^{-1} , the size of the copper crystals forming the coating increases significantly, after which it decreases. Moreover, at low reducing agent concentrations of up to 10 g L^{-1} , amorphous coatings are observed, most likely consisting of a mixture of Cu and $\text{Cu}(\text{OH})_2$. These effects are probably related to the change in the effective concentration of the reducing copper ions near the active centers. At concentrations of the reducing agent higher than 30 g L^{-1} , diffusion restrictions begin to emerge with respect to the delivery of the reducing copper ions and as a result, the size of the growing crystallites decreases.

As the concentration of the reducing agent increases, the internal strains increase too, although to a lesser extent. Based on the analysis of the results, an optimal level of concentration of the reducing agent of 30 g L^{-1} is determined.

1.3. Influence of the pH of the solution

In Fig. 2c, the diffraction patterns of deposited copper layers at different pH values of the solution are shown, on the basis of which the

microstructural parameters were calculated (Table 1).

As seen from the obtained data, the diffraction pattern is clear, unambiguously confirming the quality of the layers obtained. As the pH of the copper electrolyte increases, a gradual increase in the intensity of the peaks and narrowing of their profile is observed. After the processing of the diffraction patterns, the data show that as the pH increases, the lattice parameters begin to approach the equilibrium parameters for Cu , measured at 296 K ($a = 3.6140 \text{ \AA}$) [ICSD:627113, ICDD:98-062-7113], and the crystallites size increases almost twice. As can be seen in the Table 1, the internal strains increase too, though insignificantly. The chosen alkalinity of the solution at which the tests are performed is $\text{pH} = 9.0\div 9.3$.

1.4. Influence of the temperature of the solution for chemical copper plating

The effect of the temperature of the solution on the quality of the coatings was monitored using XRD analysis. The—diffraction patterns are presented in Fig. 2d, and the results of the profile analysis are summarized in Table 1.

As the temperature of the solution increases, an approximation of the lattice parameter of the deposited copper to the equilibrium parameter ($a = 3.6140 \text{ \AA}$) [ICSD:627113, ICDD:98-062-7113] is observed, and the size of the crystals increases significantly, which is accompanied by an increase in the internal strains. The temperature also has a favorable effect on the deposition rate of the copper coating, which rises almost three times in the range of $50\text{-}70 \text{ }^\circ\text{C}$. On the basis of the obtained results, temperature of $70 \text{ }^\circ\text{C}$ is chosen as optimal one.

1.5. Influence of the deposition time for chemical copper plating

The effect of the deposition time on the quality of the coatings was evaluated using XRD analysis. The diffraction patterns are presented in Fig. 2e, and the results of the profile analysis are summarized in Table 1.

As seen from the data shown in Fig. 2e and Table 1, the diffraction pattern is clear, unambiguously confirming the quality of the layers obtained. A gradual increase in the intensity of the peaks and narrowing of their profile at longer deposition times is observed.

All investigations were performed with the use of air stirring, as from the obtained results shown in Table 1 it can be concluded that when applying air

stirring of the solution (air flow at a rate of 100ml/min in 250 ml of solution), the crystalline size remains the same, but the thickness of the copper coating is much higher.

2. Electron-microscopic studies

Figure 3 shows the morphology of a chemical copper coating deposited from formaldehyde-free solution at different pH values.

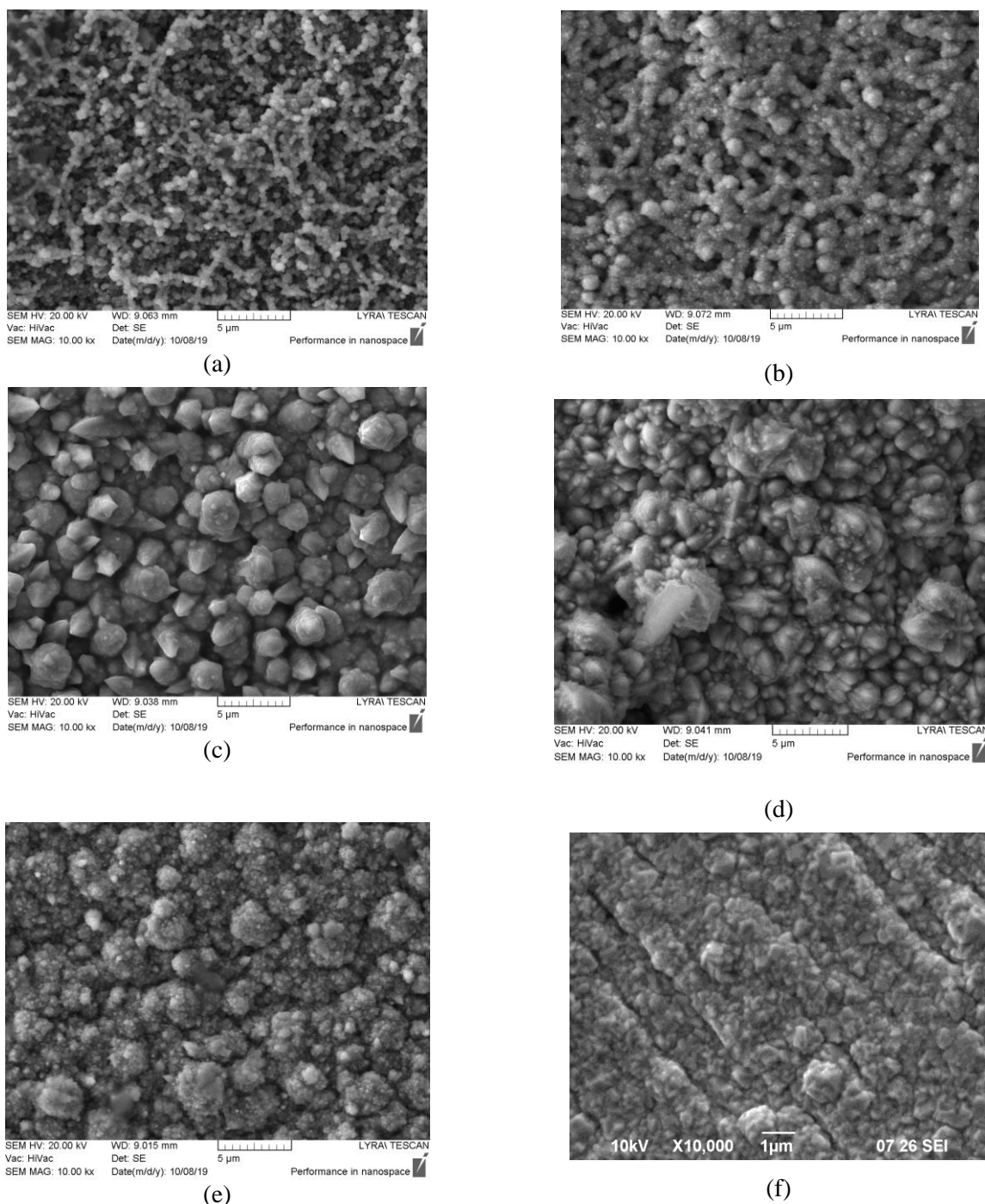


Fig. 3: SEM images of the surface of a chemical copper coating deposited in a formaldehyde-free copper bath at: a) pH =8.5($\tau_{\text{deposition}} = 20$ min); b) pH = 9.5($\tau_{\text{deposition}} = 20$ min); c) pH = 9.0($\tau_{\text{deposition}} = 20$ min); d) pH = 10.0($\tau_{\text{deposition}} = 20$ min); e) pH = 9.0($\tau_{\text{deposition}} = 5$ min); f) chemical copper coating deposited in a trilonic solution ($\tau_{\text{deposition}} = 20$ min).

Figure 3 shows that as the alkalinity of the electrolyte increases, the morphology of the copper coatings becomes more uniform and with clearly shaped agglomerates of single crystals. At low pH

values (Fig. 3a, b), a mesh structure with very small-sized particles is observed (0.1 – 0.5 μm).

SEM-images of the typical surface morphology and structure of a chemical copper coatings deposited in the selected optimal formaldehyde-free

solution at two deposition times (Fig. 3 c, e). These images are compared to the morphology of a chemical copper coating deposited in the most commonly used in the practice copper trilonic solution (Fig. 3 f).

As seen, the copper coating obtained from formaldehyde-free solution at a deposition time of 20 min (Fig. 3 c) is built of pyramidal particles with dimensions of ~ 1 - 3 μm . They are evenly spaced on the surface of the polymer. The lines along which the hydrogen, released during the reduction of the copper ions, moved are clearly outlined. At a deposition time of 5 min, the copper coating obtained from formaldehyde-free solution (Fig. 3e) is built from pyramidal particles with dimensions of ~ 0.01 - 0.1 μm , which form agglomerates several times larger in size. This morphology resembles the morphology of the copper coating obtained from the commercial trilonic solution (Fig. 3f).

EDS-analysis of the ABS polymer treated in a copper formaldehyde-free solution with different pH-values and at two deposition times reveals that there is no significant change in the copper content of the layers (Table 2).

As the copper layers obtained are of a small thickness, the presence of other elements in the substrate is excluded.

3. Roughness

AFM-studies were performed regarding the roughness of not treated ABS sample and treated ABS sample by: chemical copper deposition in a formaldehyde-free solution under the optimal conditions determined by XRD- and SEM-analyzes and by chemical copper deposition in a commercial high-alkaline trilonic solution (Fig. 4). After chemical metallization, the treated samples show considerably greater

Table 2: EDS analysis of ABS polymer treated in a copper formaldehyde-free solution with different alkalinity (pH) and at two deposition times

| Sample | Plating composition | | |
|-------------------------------|---------------------|--------|-------|
| | Wt.%Cu | Wt.%Ni | Wt.%P |
| pH = 8.5; τ = 20 min | 86.89 | 4.22 | 0.27 |
| pH = 9.0; τ = 5 min | 88.76 | 4.70 | 0.52 |
| pH = 9.0; τ = 20 min | 89.78 | 3.31 | 0.14 |
| pH = 9.5; τ = 20 min | 90.29 | 3.11 | 0.12 |
| pH = 10.0; τ = 20 min | 89.06 | 4.68 | 0.26 |

roughness than that of the not treated sample. The roughness values are as follows: not treated sample

- Ra = 28.95 nm; a sample chemically metallized in a formaldehyde-free solution - Ra = 460.02 nm; a sample chemically metallized in a commercial trilonic solution - Ra = 174.23 nm.

CONCLUSIONS

The influence of the composition and working conditions of a formaldehyde-free copper bath with reduced alkalinity on the morphology, microstructure and micro texture of chemically deposited copper coatings on ABS samples is studied by X-ray structural and electron-microscopic analyzes. The X-ray patterns show that at the optimal concentrations of the components of the solution (10 g.L⁻¹ CuSO₄.5H₂O and 30 g.L⁻¹ NaH₂PO₂.H₂O) and working conditions (pH = 9.0 – 9.3; T = 70 °C; air agitation), the diffraction pattern is clear, unambiguously confirming the quality of the layers obtained. Well pronounced peaks with a narrow profile are observed. The chemically deposited copper layers deposited in a formaldehyde-free copper solution differ significantly from those deposited in a commercial trilonic solution:

- In the case of chemical coatings deposited in a formaldehyde-free copper solution, the crystallites size is 65 nm and the size of the agglomerates is 1-3 μm ;
- In the case of chemical layers deposited in a trilonic solution, the crystallites size is around 33 nm and the size of the agglomerates is 0.1-0.5 μm .

Significant differences are also established in the structural parameters of the two types of copper coatings, as well as in their roughness and texture.

Acknowledgements: This research was carried out within the Project KP 06-N29/1 "Functional nanocomposite layers based on anodic aluminium oxide and its metallization" funded by the National Science Fund (Bulgaria).

REFERENCES

1. M. Šalkauskas, A. Vaškelis, *Chemical Metallizing of Plastics* (in Russian) (Khimiya, Leningrad) (1985).
2. L-M Luo, Z-L Lua, X-M Huang, X-Y Tana, X-Y Ding, J-G Cheng, L. Zhu, Y-CWu, *Surf.Coat. Technol.*, **251** (2014).
3. Y. Okinaka, T. Osaka, *Wiley-VCH Verlag GmbH*, (Weinheim, Germany) **3**, (1993).
4. A. Vaškelis, D. Satas, A.A. Tracton, *Coatings Technology Handbook*, (Marcel Dekker, New York), (2001).
5. R. Seeböck, H. Esrom, M. Charbonnier, M. Romand, U. Kogelschatz, *Surf. Coat. Technol.*, **142** (2001).
6. M. Matsuoka, J. Murai, and C. Iwakura, *J. Electrochem. Soc.*, **139**, (1992).
7. S. Nakahara, Y. Okinaka, and H. Straschil, *J. Electrochem. Soc.*, **136**, (1989).

8. I. Ohno, O. Wakabayashi, S. Haruyama, *J. Electrochem. Soc.*, **132**, (1985).
9. M. Schlesinger, M. Paunovic, *Modern Electroplating* (John Wiley & Sons), (2000).
10. A. Hung and K. M. Chen, *J. Electrochem. Soc.*, **136**, 72 (1989).
11. J. Rangarajan, K. Mahadevaiyer, W. P. Gregory, U.S. Pat. 4,818,286 (1989).
12. D. H. Cheng, W. Y. Xu, Z. Y. Zhang, and Z. H. Yiao, *Plat. Surf. Finish.*, **95**, 34 (1997).
13. A. Hung, *Plat. Surf. Finish.*, **75**, 62 (1988).
14. L. D. Burke, G. M. Bruton, J. A. Collins, *Electrochim. Acta*, **44** (1467), (1998).
15. A. Vaskelis, R. Juskenas, J. Jaciauskiene, *Electrochim. Acta*, **43**, (1998).
16. C.H. Lee, J.J. Kim, *J. Vac. Sci. Technol.*, **23** A (2005).
17. M. Cherkaoui, A. Srhiri, E. Chassaing, *Plat. Surf. Finish.*, **79** (1992).
18. J.G. Gaudiello, G.L. Ballard, *IBM J. Res. Dev.*, **37** (1993).
19. L.D. Burke, G.M. Bruton, J.A. Collins, *Electrochim. Acta*, **44** (1998).
20. S. Armyanov, O. Steenhout, N. Krasteva, J. Georgieva, J.L. Delplancke, R. Winand, J. Vereecken, *J. Electrochem. Soc.*, **143** (1996).
21. E. Valova, S. Armyanov, J.L. Delplancke, R. Winand, O. Steenhout, J. Vereecken, *J. Electrochem. Soc.*, **143** (1996).
22. C.J. Chen, K.L. Lin, *J. Electrochem. Soc.*, **146** (1999).
23. J. Li, H. Hayden, P.A. Kohl, *Electrochim. Acta*, **49** (2004).
24. Ek. Dobrova et al., BG Patent № 65604/16.04 (2009).
25. Ek. Dobrova et al., BG Patent № 66574/28.07 (2017).
26. R. Brüning, B. Muir, E. McCalla, É. Lempereur, F. Brüning, J. Etzkorn, *Thin Solid Films*, **519** (13), (2011).
27. M. Georgieva, G. Avdeev, D. Stoychev, M. Petrova, *Trans. Inst. Metal Finishing*, **93** (2), (2015).
28. L. Lutterotti, *Nuclear Inst. Methods Phys Res.*, **B 268** (2010).
29. L. Lutterotti, M. Bortolotti, G. Ischia, I. Lonardelli, H.R. Wenk, *Z. Kristallogr. Suppl.*, **26** (2007).
30. L. Lutterotti, Maud, *CPD Newsletter*, (IUCr) No. 24, December, 2000.
31. I. Salzmann, R. Resel, *J. Appl. Cryst.*, **37** (2004).
32. Thomas Degen, Mustapha Sadki, Egbert Bron, *J. Powder Diffraction*, **29** (S2), (2014).

Bending rigidity of lipid bilayers in electrolyte solutions of sucrose

Victoria Vitkova*¹, Christophe Minetti², Angelina Stoyanova-Ivanova¹

¹*Georgi Nadjakov Institute of Solid State Physics, Bulgarian Academy of Sciences, 72 Tzarigradsko Chaussee Blvd., 1784 Sofia, Bulgaria*

²*Université libre de Bruxelles, Service de Chimie Physique EP CP 165/62, 50 Avenue Franklin Roosevelt, 1050 Bruxelles, Belgium*

Received November 20, 2019; Accepted December 02, 2019

The morphology and dynamics of lipid bilayers are related to their mechanical parameters such as the bending elasticity and the intermonolayer friction. The thermal shape fluctuation analysis of nearly spherical giant lipid vesicles has been established as a versatile tool for the non-invasive measurement of the membrane bending modulus. We applied this method for probing the membrane mechanics in electrolyte solutions of sucrose. The bending rigidity of lipid membranes in aqueous solutions of mono-, di- and polysaccharides was quantified by means of a holographic tool that allows performing quantitative phase measurements for reconstituting the vesicle shape. The analysis of the time autocorrelations of vesicles' diameters along the optical axis yields the membrane tension and bending modulus. The obtained results indicate that the presence of sodium chloride modifies the effect of sucrose on the bending rigidity of lipid bilayers. Our finding is discussed in the light of the calorimetric and molecular dynamics data in the literature about the ion-induced modification of the membrane interactions with this disaccharide. We present further evidences about the softening of lipid bilayers in sucrose-containing aqueous environment.

Keywords: Lipid bilayers, bending elasticity, holographic microscopy, carbohydrates, sodium chloride

INTRODUCTION

Lipid bilayers (or membranes) are biomimetic, two-dimensional liquid crystalline structures, readily obtainable in laboratory conditions. The strong interest towards them is due in a great extent to the potential of their application in biomolecular electronics [1,2], drug delivery, cryo- and biopreservation in food industry and medicine [3,4]. The experimental and theoretical investigation of the fundamental physicochemical properties of lipid bilayers with different chemical compositions and in various aqueous environments represents an important step to the realization of numerous applications. A significant part of the experimental and theoretical studies on model lipid membranes aims at clarifying the role of the lipid environment on the membrane proteins and other functional inclusions in membranes. At present, it is known that the physical state of membranes (composition, structure, elasticity, surface charge, etc.) determines the deformability of the lipid matrix, which is substantial in the cases, when the activity of the guest molecule is governed by its conformational changes. On the other hand, the ability of lipid bilayers to deform easily, when external forces are applied, for example in hydrodynamic flows, underlies the successful use of functionalized lipid structures in pharmacology for transporting medicinal substances into the bloodstream of human organisms [3]. Hence, it is of importance to investigate all factors impacting

the membrane deformability. In aqueous medium, lipid bilayers spontaneously form closed structures, which in the case of unilamellar objects with characteristic sizes of the order of tens of micrometers are known as giant unilamellar vesicles (GUVs), successfully applied to probe the membrane properties [5] as well as cell hydrodynamics in flows [6]. Following elaborated experimental protocols, GUVs are readily prepared in laboratory conditions with good control of the chemical composition of membranes and bathing solutions. Advanced experimental methods have been developed so far for the measurement of the membrane bending rigidity [7-10]. The thermal shape fluctuation analysis (TSFA) or flicker spectroscopy applied on GUVs is one of the most elaborated ones [11,12]. After the approach based on the Fourier decomposition of the thermal fluctuations of the vesicle radius [12,13] the fluctuation spectroscopy method has been further refined with the introduction of Legendre analysis of the autocorrelation function of the vesicle contour and accounting for the white noise contribution to the calculation of the membrane bending modulus [11,13]. Here we study single-component, electrically neutral phosphatidylcholine membranes to determine the membrane bending modulus in aqueous solutions of carbohydrates as well as in electrolyte solutions of sucrose.

* To whom all correspondence should be sent.

E-mail: victoria@issp.bas.bg

EXPERIMENTAL

A Giant unilamellar vesicles (GUVs) were prepared from two phosphatidylcholine (PC) lipids, namely 1-stearoyl-2-oleoyl-sn-glycero-3-phosphocholine (SOPC) or 1-palitoyl-2-oleoyl-sn-glycero-3-phosphocholine (POPC) (Avanti Polar Lipids Inc., AL, USA) by means of the well-established electroformation method [14, 15]. Methanol and chloroform (for analysis grade) used for dissolving the lipid were provided from Fluka Inc. (Germany). Sodium chloride was purchased from Sigma-Aldrich (Germany). An electroformation chamber with two indium tin oxide (ITO)-coated glass plates, separated by a silicone spacer, was used. The spacers of the experimental chamber for the preparation of GUVs were made from polydimethylsiloxane (PDMS) – from Dow Corning (Germany). The 0.5 mm-thick (CoverWell®) spacers that were utilized in the observation chamber were provided by Sigma-Aldrich Inc. (USA). The detailed procedure of GUVs' electroformation has been described in detail elsewhere [16]. Sucrose solutions with the desired concentration of sugar and 0.01 mol/L of NaCl were prepared with bidistilled water from a quartz distiller.

The shape of a bent tension-free membrane is characterized by its principal curvatures $c_1 = 1/R_1$ and $c_2 = 1/R_2$, where R_1 and R_2 are respectively, the largest and the smallest radii of curvature in two mutually orthogonal directions. To the second order, the density of the bending energy is given by the expression

$$g_s = (1/2)k_c(c_1 + c_2 - c_0)^2 + \bar{k}_c c_1 c_2,$$

where k_c and \bar{k}_c are the moduli of curvature (bending) and saddle curvature with dimension of energy, and c_0 is the so-called spontaneous curvature. It vanishes, for symmetrical membranes as in the cases studied here [17].

For measurements by digital holographic microscopy vesicular suspensions were prepared so that the vesicle membranes enclose 0.2 mol/l of sucrose in water, while the suspending medium was the iso-osmolar aqueous solution of glucose containing 1 wt% of the biocompatible polymer of glucose, dextran. Sucrose and dextran were provided by Sigma-Aldrich Chemie (Germany), while glucose was purchased from Merck (Germany). Bidistilled water with pH~5.5 was used for the preparation of sucrose and glucose solutions. The measurements of the membrane bending rigidity were performed at room temperature (~22°C).

The observations of the vesicles' shape fluctuations were conducted by means of an

inverted microscope Axiovert 100 (Zeiss, Germany). The visualization of the membrane fluctuations was carried out in phase contrast regime, using an oil-immersed objective (100x, NA 1.25). The image-recording was performed using a CCD camera (C3582, Hamamatsu Photonics, Japan). The video signal from the camera was fed to a frame grabber board (DT3155, Data Translation, USA, 768x576 8-bit pixels, pixel size: 0.106 $\mu\text{m}/\text{pix}$). For each chosen vesicle, at least several hundred images were captured once per second and processed for deducing the bending elasticity modulus and membrane tensions [11, 18]. The stroboscopic illumination of the observed vesicles, synchronized with the camera, permitted the fastest modes of fluctuations to be recorded and processed [19].

A particularly important step in the image treatment consisted in precisely locating the position of the vesicle contour (Figure 1), corresponding to the equatorial cross-section of the vesicle with the focal plane of the microscope in each image from the recorded sequence of snapshots.

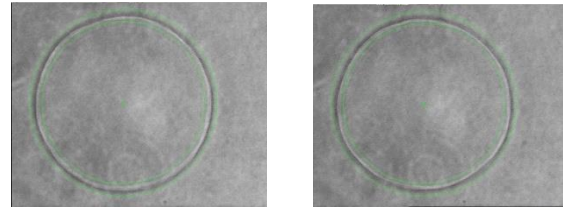


Fig. 1. Phase-contrast images of a POPC vesicle ($R_v = 19.5 \mu\text{m}$) for the analysis of the thermal shape fluctuations of the vesicle contour; 7 s time lapse.

Optical techniques providing information about the fluctuations of vesicle membranes are developed to increase the precision of the bending rigidity measurements as in the case of digital holographic microscopy (DHM) [20]. The vesicle fluctuations were monitored and recorded using a microscopic holographic system described in details elsewhere [21]. The DHM approach utilizes the knowledge of the optical complex amplitude, namely amplitude and phase, to refocus numerically each slide in the experimental volume. In the experimental procedure, the vesicles were slightly defocused for a better visualization. As a result the optical phase map of the vesicles might be distorted because they do not correspond to the focus plane of the vesicle. Dry objectives (Olympus, Japan) with magnification $\times 20$ and numerical aperture NA 0.3 were applied to achieve the appropriate optical resolution. The experimental parameters of our set-up are the following: laser wavelength of 633 nm; pixel size of 208 nm; frame

rate of 24 frames per second with exposure time of 200 μ s. The measured phase $\phi(x, y)$ is related to the vesicle diameter, d and the refractive index difference, Δn , between the fluid, enclosed by the vesicle membrane and the surrounding aqueous solution.

$$\phi(x, y) = \frac{2\pi}{\lambda} d \Delta n \quad (1)$$

The first step of the processing consists in the determination of the focus plane of each vesicle. The focus plane was determined by scanning along the optical axis a region of interest around the object under investigation and by computing for each plane the gradient of the amplitude modulus. Once the focus plane determined, we calculated the amplitude and the phase map in this plane. Due to the phase periodicity unwrapping procedure was applied in order to remove the discontinuities (phase jumps) with a period of 2π . The background phase, defined as the phase obtained when no object is present in the field of view, was approximated by a bi-dimensional quadratic phase map. For every studied vesicle the background phase map was fitted on the basis of the phase map in a neighborhood region where no objects were present. The numerical processing of the images consisted in removing the non-uniform background by successive segmentation and background fitting until the resulting background is completely flat and uniform as shown in Figure 2. In the present study only the fluctuations of the vesicle diameter laying on the optical axis of the microscope were extracted and analyzed. Hence, a segmentation process is performed on the vesicle to extract its contour and determine its center. The value of the phase in the center of the vesicle, proportional to the vesicle radius, is then deduced. Its time autocorrelation function is related to the bending modulus and the lateral tension of vesicle membrane. The experimentally acquired data for the fluctuations of the vesicle diameter with time were fitted with the theoretical expression for the autocorrelation function. The fit yielded the values of the two free parameters, which are the bending modulus and the lateral membrane tension for every analyzed vesicle [20].

The DHM method was applied for the evaluation of the bending elasticity modulus of SOPC membranes in aqueous solutions of 0.2 mol/L of sucrose.

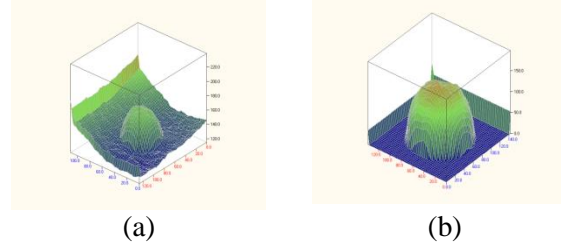


Fig. 2. (a) vesicle with non-uniform background; (b) flat and uniform background after numerical processing (see text); $R_{\text{ves}}=8.11\pm 0.05 \mu\text{m}$

For the static thermal shape fluctuation analysis (TSFA) following Bivas et al. [13] we calculate the time average of the normalized angular autocorrelation function of the vesicle contour's radius (Figure 1) at N angular directions as described in detail elsewhere [11]:

$$\xi(\gamma, N) = \left\langle \frac{1}{2\pi R_v} \int_0^{2\pi} [R(\varphi, t) - R_v][R(\varphi + \gamma, t) - R_v] d\varphi \right\rangle \quad (2)$$

where R_v is the volume of a sphere with volume equal to the vesicle volume. The function expressed by (2) is decomposed into a series with respect to Legendre polynomials with amplitudes depending on the bending elasticity modulus and the mechanical tension of the vesicle membrane. For the calculation of the bending constant we follow the fitting procedure described in detail in [11].

RESULTS AND DISCUSSION

Less than 10% of all recorded and processed vesicles satisfied the criteria of acceptance [6, 11] thus providing an ensemble of eleven vesicles with goodness of fit higher than 0.1, used for the evaluation of the membrane bending modulus as described in detail in [20]. This experimental result is presented in Figure 3 (open circle). It is comparable to the values of the bending constant of phosphatidylcholine membranes published in the literature [22, 23].

Fig. 3 recapitulates the experimental data acquired so far for the bending modulus of phosphatidylcholine bilayers in aqueous solutions of sucrose. Three experimental methods utilizing GUVs have been applied for quantifying the bending rigidity of lipid bilayers. Shape fluctuation spectroscopy data are presented in Figure 3 with full circles in pure water and at 50 mM of sucrose [16]. The full triangle stands for the result from the shape fluctuation analysis at 20 mM of sucrose, reported in [24]. As shown in [11] accounting for the white-noise contribution to fluctuations of the vesicle contour, $\Delta R^{\text{noise}}(\varphi, t)$, yields 30%-higher value of the bending modulus, which could be the

origin of the shift between the value reported in [24] and our results [16]. The open circle in Figure 3 corresponds to our DHM result for the bending modulus of PC membranes in carbohydrate-containing aqueous solutions. The obtained value is lower than the bending constant of PC bilayers in pure water, which is in accordance with the softening effect of sugars on lipid membranes reported earlier [6, 16, 25, 26].

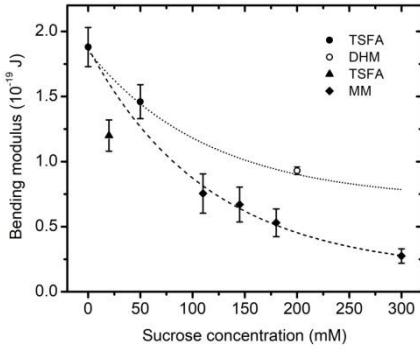


Fig. 3. Bending modulus of phosphatidylcholine bilayers in aqueous solutions of sucrose acquired by different experimental methods: TSFA – thermal shape fluctuation analysis (full circles [16], triangle [24]); DHM – digital holographic microscopy (open circle, this study); MM – mechanical micromanipulation (full squares [25]).

The relative reduction in the bending modulus measured by fluctuation analysis is smaller than the k_c decrease obtained by GUVs micromanipulation (MM) [25]. The absolute values of the bending modulus in the micropipette study are lower than the values presented here and the sources of these differences being of various origins are discussed in [16]. Lower apparent bending modulus is expected from mechanical micromanipulation measurements without “pre-stressing” of vesicles [27] due to the contribution of the hidden area of the vesicle membrane [28]. Disregarding the white noise’s contribution to the recorded fluctuations of the vesicle membrane, or a possible non-stationarity of vesicles due to uncontrolled deflation during measurements, or the non-uniformity of the mean vesicle’s radius over all angular directions, could be responsible for the divergence of the bending rigidity values reported in previous fluctuation analysis studies in the literature. As pointed out in [16] measures have been taken to overcome the method-related side contributions to the reported values of the membrane bending rigidity deduced from GUVs’ shape fluctuations analysis.

We further develop the approach proposed in [25] for fitting the micromanipulation data with an

empirical exponential-decay equation (the dashed line in Figure 3) of the type:

$$k_c(c) = k_{c,min} + \Delta k_c \exp(-c/c_0) \quad (3),$$

where c is the sucrose concentration in the bulk phase, $k_{c,min}$ stands for the minimum value of the bending modulus, $\Delta k_c = k_c(0) - k_{c,min}$, and c_0 is the sucrose concentration at which the bending modulus decreases with $\sim 2\Delta k_c/3$ compared to its value in pure water $k_c(0)$. The fitting procedure with eqn. (3) yields $k_{c,min} = (0.151 \pm 0.004)10^{-19}$ J, $\Delta k_c = (1.73 \pm 0.06)10^{-19}$ J, $c_0 = (115 \pm 11)$ mM with goodness of fit (coefficient of determination) nearly 1.

TSFA and DHM data set of only three sucrose concentrations are not sufficient to perform the fitting procedure but nevertheless comparing the experimental data with an exponential-decay curve of the same type as Eqn. (3) and parameters $k_{c,min} = 0.73 \times 10^{-19}$ J, $\Delta k_c = 1.15 \times 10^{-19}$ J, $c_0 = 115$ mM, gives a qualitatively satisfying description of the observed sucrose concentration-dependent trend.

A possible explanation of the experimental result that the bending modulus obtained from micropipette aspiration without pre-stressing of GUVs, was measured to decrease more steeply would be the hypothesis of that the hidden area of the vesicle membrane increases at higher sucrose concentrations. In a previous study we measured also the stretching elasticity of PC monolayers in sucrose solutions via mechanical micromanipulation of emulsion droplets [25]. Our results revealed the strong influence of sucrose dissolved in the water environment on the stretching elasticity modulus of phosphatidylcholine monolayers.

We performed a series of TSFA measurements to probe the membrane mechanics in sucrose salt solutions.

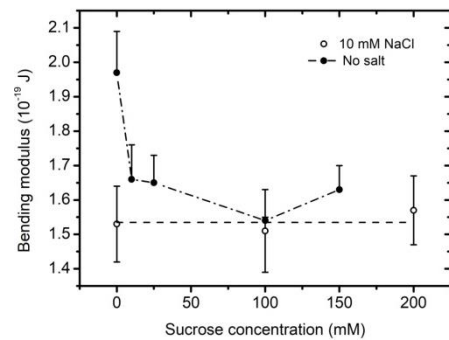


Fig. 4. Bending modulus of POPC bilayers in aqueous solutions of sucrose and NaCl at concentrations: 10 mM (open circles, dashed line) and 0 mM (full circles, dash-dotted line).

The membrane bending elasticity measured in sucrose solutions containing 10 mM of NaCl is independent of the disaccharide concentration in the aqueous surroundings as shown in Figure 4 (open circles, dashed line). This result can be considered in the light of the ion-induced modification of sucrose-phosphatidylcholine hydrogen bond (HB) network, reported in the literature [29, 30]. Molecular dynamics (MD) simulations and Fourier-transformed infrared (FTIR) spectroscopy studies revealed that the capability of disaccharides to replace water molecules [31] and to create a water-like HB network in the lipid surrounding contributes to retaining of the molecular properties of lipids [32]. The analysis of MD simulation results has provided evidences that the HB network of PC and sucrose is partially disrupted in the presence of NaCl ions [30].

CONCLUSIONS

The physicochemical properties of lipid structures are studied in relation to many biomedical applications including drug vectorization, liposome-based developments in beauty industry, cryopreservation and desiccation control in food industry and medicine. In the present work, unilamellar lipid vesicles with quasispherical shape and diameters of the order of tens of micrometers, GUVs, were used for the measurement of the bending elasticity modulus of single-component phosphatidylcholine bilayers at different sucrose concentrations in the surrounding aqueous environment. We reported on the determination of the bending rigidity of phosphatidylcholine membranes in electrolyte solutions containing carbohydrate molecules by means of experimental techniques utilizing GUVs. Using an empirical approach we analyzed the experimental data collected from micromanipulation measurements, thermal shape fluctuation spectroscopy and digital holographic microscopy on GUVs. For the assessment of the membrane bending modulus in aqueous solutions of mono-, di- and polysaccharides, we applied digital holographic microscopy based on quantitative phase measurements on fluctuating giant unilamellar vesicles and the subsequent analysis of the fluctuations of the vesicle diameter along the optical axis of the microscopic imaging system. The fully automated data treatment and the potential to reconstitute the tri-dimensional shape of lipid vesicles are only some of the advantages of the holographic approach for evaluating the bending constant of lipid bilayers.

Acknowledgements: The authors thank Prof. Yu. A. Ermakov for the enlightening discussions. Financial support from the National Science Fund of Bulgaria (Grant DN08-7/2016), WBI, FRS-FNRS and the Bulgarian Academy of Sciences is acknowledged.

REFERENCES

1. P. Facci, Biomolecular Electronics. 2014, Amsterdam: Elsevier Inc.
2. A. G. Petrov, The Lyotropic State of Matter: Molecular Physics and Living Matter Physics. 1999, Amsterdam: Gordon & Breach. 549.
3. T. M. Allen, P.R. Cullis, *Science*, **303**, 1818 (2004).
4. B. Stark, G. Pabst, R. Prassl, *Eur. J. Pharm. Sci.*, **41**, 546 (2010).
5. R. Dimova, in Advances in Planar Lipid Bilayers and Liposomes, A. Iglič (ed), vol. 16, Elsevier: Burlington. 2012.
6. V. Vitkova, C. Misbah, in Advances in Planar Lipid Bilayers and Liposomes, A. Iglic (ed), vol. 14, Academic Press: Burlington. 2011, p. 258-292.
7. M.B. Schneider, J. T. Jenkins, W. W. Webb, *Biophys. J.*, **45**, 891 (1984).
8. M. Kummrow, Helfrich, W., *Phys. Rev. A*, **44**, 8356 (1991).
9. E.A. Evans, *Biophys. J.*, **14**, 923 (1974).
10. R. Dimova, *Adv. Colloid Interface Sci.*, **208**, 225 (2014).
11. J. Genova, V. Vitkova, I. Bivas, *Phys. Rev. E*, **88**, 022707 (2013).
12. M.D. Mitov, J. F. Faucon, P. Méléard, P. Bothorel, in Advances in Supramolecular Chemistry, G. W. Gokel (ed), vol. 2, JAI Press Inc.: Greenwich, CT. 1992, p. 93-139.
13. I. Bivas, P. Hanusse, P. Bothorel, J. Lalanne, O. Aguerre-Chariol, *J. Physique*, **48**, 855 (1987).
14. M. Angelova, D.S. Dimitrov, *Progress in Colloid and Polymer Science*, **76**, 59 (1988).
15. V. Vitkova, K. Antonova, G. Popkirov, M.D. Mitov, Y.A. Ermakov, I. Bivas, *J. Phys. Conf. Ser.*, **253**, 012059 (2010).
16. D. Mitkova, V. Vitkova, *Russ. J. Electrochem.*, **52**, 1172 (2016).
17. W. Helfrich, *Z. Naturforsch.*, **28c**, 693 (1973).
18. M.D. Mitov, J.F. Faucon, P. Meleard, P. Bothorel, G.W. Gokel (ed), vol. 2, JAI Press Inc.: Greenwich. 1992, p. 93-139.
19. J. Genova, V. Vitkova, L. Aladgem, M.D. Mitov, *J. Optoel. Adv. Mater.*, **7**, 257 (2005).
20. C. Minetti, V. Vitkova, F. Dubois, I. Bivas, *Opt. Lett.*, **41**, 1833 (2016).
21. C. Minetti, T. Podgorski, G. Coupier, F. Dubois, Proc. SPIE 8429, 84291I (2012).
22. D. Marsh, *Chem. Phys. Lipids*, **144**, 146 (2006).
23. E. Evans, D. Needham, *J. Phys. Chem.*, **91**, 4219 (1987).
24. H.A. Faizi, S. L. Frey, J. Steinkuhler, R. Dimova, P.M. Vlahovska, *Soft Matter*, **15**, 6006 (2019).
25. V. Vitkova, J. Genova, M.D. Mitov, I. Bivas, *Mol. Cryst. Liq. Cryst.*, **449**, 95 (2006).

26. P. Shchelokovskyy, S. Tristram-Nagle, R. Dimova, *New J. Phys.*, **13**, 025004 (2011).
27. K. Olbrich, W. Rawicz, D. Needham, E. Evans, *Biophys. J.*, **79**, 321 (2000).
28. V. Vitkova, Genova, J., Bivas, I., *Eur. Biophys. J.*, **33**, 706 (2004).
29. C.C. Valley, J.D. Perlmutter, A. R. Braun, J.N. Sachs, *J. Membr. Biol.*, **244**, 35 (2011).
30. D. Bakarić, D. Petrov, Y.K. Mouvenccherya, S. Heißler, C. Oostenbrink, G.E. Schaumann, *Chem. Phys. Lipids*, **210**, 38 (2018).
31. M.C. Luzardo, F. Amalfa, A.M. Nunez, S. Diaz, A.C. Biondi de Lopez, E. A. Disalvo, *Biophys. J.*, **78**, 2452 (2000).
32. S. Leekumjorn, A.K. Sum, *J. Phys. Chem. B*, **112**, 10732 (2008).

Electrochemical polymerization and in situ characterization of PANI in presence of chemically modified graphene

A. Petrovski¹, P. Perica Paunović*¹, A. Grozdanov^{1,2}, A. T. Dimitrov¹, I. Mickova¹, G. Gentile², M. Avella²

¹Faculty of Technology and Metallurgy, Ss Cyril and Methodius University, RudjerBošković, 16, 1000 Skopje, R. Macedonia

²Institute for Chemistry and Technology of Polymers, National Research Council, Fabricato Olivetti 70, Pozzuoli, Napoli, Italy

Received October 27, 2019; Accepted January 21, 2020

The subject of this research is in situ study of the process of polyaniline (PANI) electro-polymerization in the presence of graphene. The Graphene was firstly purified/chemically modified, and then SEM/EDS analysis was performed in order to characterize the material. These results have shown that purification and chemical modification of the graphene, leads to formation of some complex groups which is good for interaction with polymers and formation of nanocomposites. In order to determine the conditions for electro-polymerization of aniline to PANI in the presence of graphene, electrochemical characterization was performed by means of cyclic voltammetry (CV) and steady state polarization (SS). The influence of different scan rates (10, 20, 50 and 100 mV.s⁻¹) was examined during the process of electro-polymerization and the double layer capacity of pure PANI (1.75 mF.cm⁻²) and nanocomposite with graphene (121.07 mF.cm⁻²) was calculated. The influence of the type of CNSs, different mass fractions (1%, 2%, 3% and 10 % wt. graphene vs. PANI) and two different pathways of introduction of graphene in PANI matrix on the electro-polymerization rate were analyzed. According to these results, it is confirmed that graphene acts as an incipient in the process of electro-polymerization and improves the electrical conductivity and the double layer capacity of PANI, which is suitable for various fields of applications of this nanocomposite.

Keywords: Electro-polymerization, polyaniline (PANI), graphene, cyclic voltammetry (CV), steady state polarization (SS)

INTRODUCTION

Within the conductive linear-backbone polymers such as polyacetylene, polypyrrole, polyindole and their copolymers, PANI shows the greatest attraction to the scientific community. It possesses unique properties such as good environmental stability, easy and low cost synthesis, electrical and electrochemical properties such as electrical conductivity, electrochemical activity, and possibility to adjust these properties during the synthesis and doping processes [1-3]. PANI can exist in five redox states, from which emeraldine base is the only electrical conductive form [4, 5], when is converted in emeraldine salt. PANI is appropriate for various fields of applications such as energy storage devices, electrochromic devices, supercapacitors, sensors etc. [4-6]. However, its application is constrained by some disadvantages such as poor mechanical properties and low process ability. Due to the nature of this polymer, it is very difficult to overcome these disadvantages and presents a big challenge to the scientific community. Different approaches have been tried to make PANI soluble; to obtain PANI suitable for processing in its liquid

state; to adjust its electrical conductivity during the doping process and researches have been done about the impact of the humidity on this properties [5-11]. All these researches show some promising results, but there are still some of its disadvantages left to explore.

One of the next steps in improving the applications of PANI is obtaining of PANI with graphene nanocomposites. One of PANI's useful properties is the interaction with polymers and forming of nanocomposites. PANI/graphene nanocomposites can be prepared using direct mixing methods, chemical or electrochemical polymerization [12]. All of these methods have their own advantages and disadvantages, but electrochemical polymerization has shown the best results in order to obtain pure PANI form without some residuals of the other redox states, which can affect the properties of the nanocomposite. This method is appropriate for direct electro-polymerization of the nanocomposites on screen printed electrodes with the possibility to control the thickness of the film and to control its properties, which is extremely useful for applications in electronics, electrochemical devices, sensors etc. [13].

* To whom all correspondence should be sent.

E-mail: pericap@tmf.ukim.edu.mk

In order to obtain good interfacial interactions between graphene and PANI, several authors propose previous functionalization of the graphene's surface in order to form some functional groups which are suitable for interaction with PANI, and therefore, the formation of stable nanocomposite [14, 15].

This work is done in order to characterize PANI/graphene nanocomposites using in situ electrochemical measurements in the process of electro-polymerization of PANI in the presence of graphene.

2. EXPERIMENTAL

2.1. Materials

For the experiments in this paper, aniline, sulfuric acid (H_2SO_4), nitric acid (HNO_3), hydrogen peroxide (H_2O_2), hydrogen fluoride (HF) and distilled water were used. The chemicals were supplied by Sigma Aldrich. All chemicals had p.a. purity, except the aniline which was purified by distillation. The graphene used was produced in the laboratory of the Faculty of Technology and Metallurgy in Skopje by exfoliation during molten salts electrolysis [16].

2.2. Purification and preparation of chemically modified graphene

For further use, the graphene was purified and then modified by standard procedures [17, 18]. The procedure comprises dispersing 10 g graphene nanoparticles in 300 ml distilled water and then exposing the dispersion to ultrasound for 30 minutes. After that, concentrated H_2O_2 was added to the dispersion to be used a 10 % solution and was stirred by magnetic stirrer for 2 h with 900 rpm. The dispersion was filtered through vacuum filter and the solid fraction was washed several times with boiled distilled water and with cold distilled water at the end. Further, the solid fraction was dispersed in concentrated solution (49 %) of HF, and after 1 h was filtered and washed as before. With this procedure, graphene was purified from some of the residuals such as unexfoliated graphite and some inclusions from the production process [16]. This was confirmed by SEM/EDS study. SEM observation was carried out by scanning electron microscope (SEM) FEI Quanta 200 using secondary electron detector and acceleration voltage of 30 kV.

In order to produce chemically modified graphene, purified graphene was treated with a mixture of concentrated H_2SO_4 and HNO_3 acids (volume ratio H_2SO_4 to HNO_3 was 3:1). Weight

ratio of graphene to acid solution was 100:1. The dispersion was stirred by magnetic stirrer for 12 h at 50 °C to get acid modified graphene. After that, the solution was centrifuged at 5000 rpm. The solid fraction was washed with distilled water several times to purify graphene from acid residuals [18].

2.3. Electrochemical cell and instrumentation

The experiments were carried out in 250 ml three-electrode one-compartment glass cell. The working electrode was platinum tile with active surface of 10 cm² and a platinum grid was used as counter electrode. As a reference electrode Saturated calomel electrode (SCE) was used. The polymerization electrolyte consists of 0.1 M aniline dissolved in 0.5 M H_2SO_4 .

The electrochemical characterization was performed by METROHM Autolab PGSTAT 128 N for CV and WENKING HC 500 for stationary polarizing investigations. All the experiments were carried out at room temperature.

3. RESULTS AND DISCUSSION

3.1. SEM/EDS analysis of graphene

Scanning electron microscopy was performed in order to study the graphene morphology and the effect of the purification/modification processes. Fig. 1 shows untreated graphene (Fig. 1-a), purified graphene by H_2O_2 and HF (Fig. 1-b) and chemically modified graphene by mixture of H_2SO_4 and HNO_3 (Fig. 1-c). As it can be seen, graphene flakes are with diameter from 1 to 20 μm . These variations of the diameter are attributed to the difficulty of controlling the interactions in the exfoliation process [19]. According to the literature [20], graphene shows high transparency from about 97.7 %. Xie and Spallas report [21] that it is impossible to count the flakes and analyze graphene layers using SEM, and this analysis is useful only for morphology investigations. According to this, analyzing the transparency of the graphene shown at Figure 1, one can conclude that there is a big variation of the number of layers into graphene flakes, but an accurate count cannot be done. Due to the transparency shown in Figure 1-a, there is a regions with unexfoliated graphite left in the material. The white dots left on the graphene flakes surface confirm this. Analyzing Figure 1-b, after treatment of the graphene with H_2O_2 and HF, there is no presence of white dots on the graphene flakes surface, and the transparency of the material is more uniform, which points out on efficient removal of the residuals from graphene. This is also confirmed with EDS, and the results are shown in Table 1.

Table 1. EDS analysis of graphene

| | C | O | Na | Cu |
|---|-------|-------|------|------|
| Unreacted graphene | 87.9 | 6.24 | 5.78 | 0.08 |
| Graphene treated with H ₂ O ₂ and HF | 89.51 | 5.07 | 5.29 | 0.13 |
| Graphene treated with H ₂ SO ₄ and HNO ₃ | 86.30 | 11.66 | 2.05 | / |

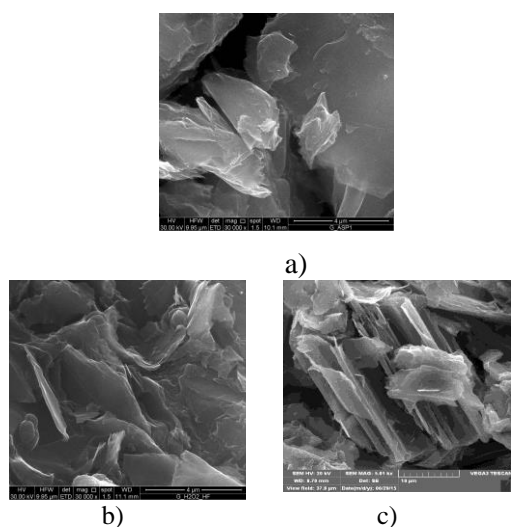


Fig. 1. TEM images of a) as-prepared graphene, b) purified graphene by H₂O₂ and HF and c) chemically modified graphene by mixture of H₂SO₄ and HNO₃.

Purification of graphene, leads to wrinkled structure that causes sheet folding [22]. Treating the graphene with strong acid solutions such as concentrated H₂SO₄ and HNO₃, causes edges cutting and gives a more uniform form of the flakes. In the graphene flakes shown in Figure 1-c, oxidized edges can be seen, which can be attributed to the formation of some amide and carbamide groups with hydroxyl and carboxyl groups. This results in the disruption of sp² bonds, transforming them into sp³ bonds. These transformed carbon centers results in the creation of electron-flow disruptions and the creation of an energy gap. In this way, the functionalization of multiple-layer graphene will change the electronic properties from near-metal into semiconducting [17,23]. These oxidized edges with formation of carboxyl and hydroxyl groups were also confirmed by EDS analysis. The results presented in Table 1, show

that there is a great increase of oxygen in the material which points out that the chemical modification leads to the formation of these groups on its surface as well as to the complete removal of the residuals such as Na and Cu. On the other hand, the introduction of sulfur in the material leads to some complex groups with carboxylic groups being formed. These transannular interactions can cause polarization of the carboxylic groups [24], which is helpful for the whole interaction with polymers and formation of composites. Also, within this phenomenon proton removal from some components occurs [25], which is useful for the application of graphene in some electrochemical devices.

3.2. Cyclic voltammetry (CV)

Cyclic voltammetry was performed in order to determine the redox processes of the electro-polymerization of aniline to polyaniline. Cyclic voltammograms were scanned in the potential region of -0.2 to 1 V with and without presence of graphene. Shown on Fig. 2 are the CV spectra recorded for the following electrolytes: i) 0.1 M aniline + 0.5 M H₂SO₄ and ii) 0.1 M aniline + 0.5 M H₂SO₄ + graphene 3 % wt. related to the weight of aniline.

Both spectra show the same eight characteristic peaks related to the corresponding redox reactions characteristic for oxidation/reduction in the aniline/polyaniline system [26]. These peaks are more intense and very well pronounced for the electrolyte including graphene, in comparison with the corresponding peaks for the electrolyte containing 0.1 M aniline + 0.5 M H₂SO₄. Positions of the corresponding peaks are presented in Table 2.

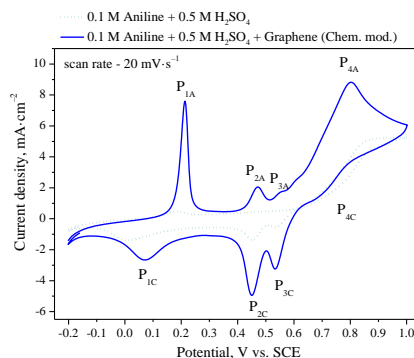


Fig. 2. Cyclic voltammograms of a) 0.1 M aniline + 0.5 M H₂SO₄ and b) 0.1 M aniline + 0.5 M H₂SO₄ + graphene 3 % wt. related to the weight of aniline.

Table 2 Position of characteristic peaks (V) registered by cyclic voltammetry.

| Electrolyte | P _{1A} | P _{1C} | P _{2A} | P _{2C} | P _{3A} | P _{3C} | P _{4A} | P _{4C} |
|---|-----------------|-----------------|-----------------|-----------------|-----------------|-----------------|-----------------|-----------------|
| 0.1 M Aniline + 0.5 M H ₂ SO ₄ | 0.184 | 0.023 | 0.473 | 0.450 | 0.553 | 0.530 | 0.889 | 0.64 – 0.78 |
| 0.1 M Aniline + 0.5 M H ₂ SO ₄ + Graphene (Chemically modified) | 0.214 | 0.072 | 0.471 | 0.450 | 0.559 | 0.533 | 0.802 | 0.64 – 0.78 |

The first step of oxidation of aniline is denoted with P_{1A}. It is attributed to the transformation of leucoemeraldine (basic oxidation state of PANI - completely reduced) to emeraldine (oxidation state of PANI - half oxidized). P_{1C} in cathodic region is attributed to the reverse transformation. For both electrolytes, the position of the peaks P_{1A} and P_{1C} is at different potentials (Table 1), which points out on the irreversibility of this redox reaction. The next redox pair P_{2A}/P_{2C} corresponds to the formation of secondary by products like benzoquinone and hydroquinone [26], and this also leads to overoxidation and degradation of PANI [27]. The redox pair P_{3A}/P_{3C} is ascribed to the transformation of p-aminophenol to benzoquinonemine and vice versa [27, 28]. Also, these redox reactions are irreversible according to the positions of the anodic and corresponding cathodic peaks (Table 1). The last oxidation peak P_{4A}, corresponds to the transformation of emeraldine oxidation state of PANI (half oxidized) to pernigraniline (completely oxidized state) [29, 30].

Due to the presence of carbon nanostructure in the electrolyte, the growth of the composite on the electrode is more intense. This can be attributed to higher electroconductivity and electroactivity of graphene that lead to faster electrons exchange between ions and the electrode [31]. Graphene also acts as a incipient in the system because of its large specific surface and accelerates the reaction rate.

The influence of the purification and modification of graphene on the reaction rate is shown on Fig. 3.

The presence of untreated graphene shows slightly higher current densities than those in the voltammogram of pure PANI. Purification of graphene causes further increase of the current densities related to the previous systems. The increase in current densities is more pronounced in cases where chemically modified graphene is used.

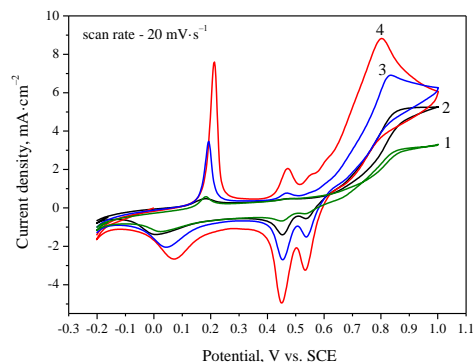


Fig. 3. Cyclic voltammograms of aniline in presence of chemically modified graphene (4), purified graphene (3), untreated graphene (2) and without presence of carbon nanostructure (1). Electrolyte: 0.1 M Aniline + 0.5 M H₂SO₄

This confirms the considerations from SEM/EDS analysis and shows that the purification and chemical modification of graphene leads to higher active surface area of the material and better electrical conductivity [31].

In order to determine the double layer capacitance of the produced nanocomposite and pure PANI, cyclic voltammetry measurements were performed at different scan rates: 10, 20, 50 and 100 mV·s⁻¹. The corresponding CV spectra of pure PANI (electrolyte: 0.1 M Aniline + 0.5 M H₂SO₄) is shown on Fig. 4. At the intersection of voltammograms in the region of charge and discharge of the electrochemical double layer, from the corresponding values of anodic and cathodic currents densities, the double layer capacity (C_{dl}) of the produced material can be determined, using the following equation [32]:

$$C_{dl} = \frac{di_{cap}}{d\left(\frac{\partial E}{\partial t}\right)} \quad (1)$$

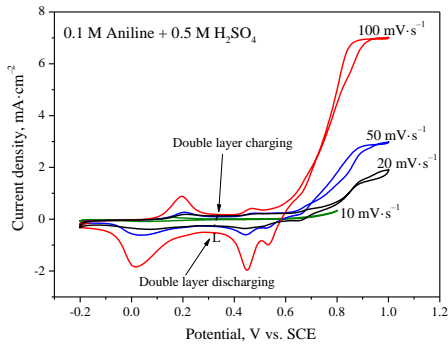


Fig. 4. Cyclic voltammograms of pure aniline (0.1 M aniline + 0.5 M H₂SO₄) at different scanning rates.

The current density of the electrochemical double layer i_{cap} at given scanning rate, is determined as the mean value of the absolute values of the anode and cathode currents at the potential of the intersection of the curves (line L). The dependence of the changes of i_{cap} on the scanning rate is a straightline whose slope represents the value of the double layer capacity, C_{dl} .

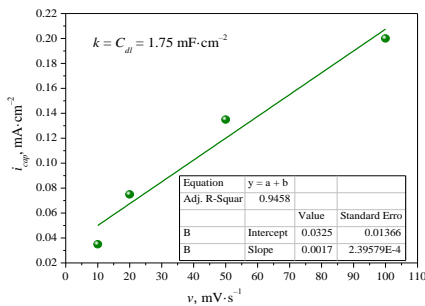


Fig. 5. Dependence of the changes of i_{cap} on the scanning rate for the system: 0.1 M Aniline + 0.5 M H₂SO₄.

This is presented in Fig. 5 and the calculated value for the capacity of the polyaniline is 1.75 mF.cm⁻².

Corresponding voltammogram for the system 0.1 M Aniline + 0.5 M H₂SO₄ + 3 wt. % of chemically modified graphene is shown in Fig. 6.

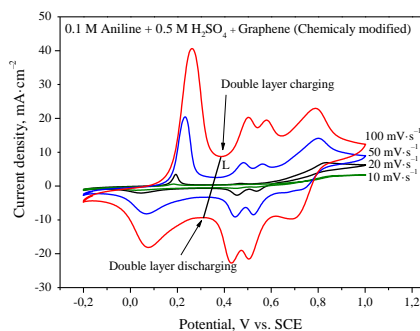


Fig. 6. Cyclic voltammograms of aniline with graphene (0.1 M aniline + 0.5 M H₂SO₄ + graphene 3 % wt.) at different scanning rates.

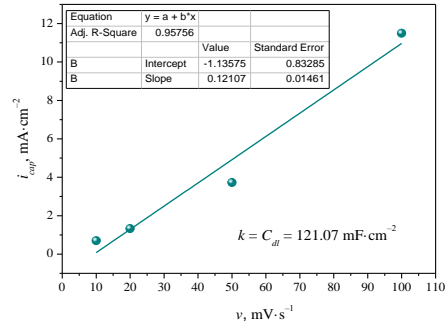


Fig. 7. Dependence of the changes of i_{cap} on the scanning rate for the system: 0.1 M Aniline + 0.5 M H₂SO₄ + graphene 3 % wt.

The calculated value for the double layer capacity of the polyaniline/graphene nanocomposite is 121.07 mF.cm⁻² (Fig. 7).

The double layer capacity increased for about 70 times in relation to the double layer capacity of the pure polyaniline. These results show that by incorporating of only 3 % chemically modified graphene in the polymer matrix, the electrochemical properties of the material can be improved up to several times. This is promising for application of these nanocomposites in electrochemical and energy storage devices [33-35].

3.3. Steady-state polarization measurements

As shown, nanocomposites which consist of PANI/graphene possess enhanced electrical properties. Several authors presented various effects of the graphene on the properties of the polymer matrix [36-39], and all point out that emeraldine's conductive form of PANI is the most appropriate for electrochemical applications and electronic devices. This research is done in order to obtain nanocomposite for sensing applications. Therefore, the produced material should have good electrical properties. In our previous work [40], steady-state polarization measurements have shown that PANI as emeraldine form can be produced at constant potentials in the region of 0.64–0.8 V. But, the optimal potential in electrolyte that contains 0.1 M Aniline + 0.5 M H₂SO₄ + graphene, was shown to be 0.75 V [40].

In this work, steady-state galvanostatic measurements were performed in order to determine the influences of different electrolysis conditions on the electro-polymerization of PANI/graphene nanocomposites at constant potential of 0.75 V.

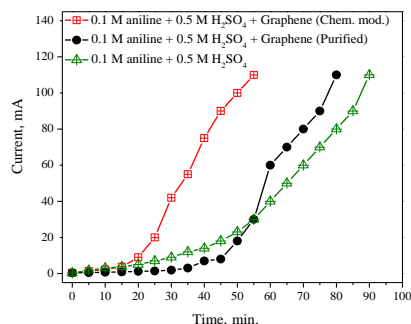


Fig. 8. Steady-state polarization curves for pure aniline and aniline with addition of differently treated graphene.

Firstly, the influence of purification and modification of graphene to the polymerization rate was studied. This is shown in Figure 8. The system with purified graphene at the beginning shows slower polymerization rate when compared to that of pure PANI, but later, the polymerization rate increases. Also, the change of current is non-linear until 60 mA, at which the nanocomposite was already formed, and further on the current shows linear changes. This is due to the wrinkled and folded structure of graphene as result of the purification process, which causes non-uniform forming of the polymer chains on the graphene surface [22]. This can be explained by the so called induction period [41-43], when embryos are created. Also, several successive processes of polymer chain formation occur such as oxidation of aniline to radical cations, oxidation of these radicals to oligomers and finally, forming of a macromolecule of PANI. After forming of the macromolecule of PANI, the polymerization process is stabilized [44]. This also confirms that graphene acts as an incipient in the electro-polymerization process, but that purification does not have much effect on the polymerization rate. By performing the chemical modification process of the graphene surface, a faster rate of polymerization is achieved and the linearity of the curve is more uniform. The polymerization rate is almost double than pure PANI. This shows that chemical modification of the graphene surface causes much better and stable conductivity than that of purified CNSs, due to the carboxyl and hydroxyl groups which allows better interactions with polymer matrix [45]. This is in accordance with the results of SEM/EDS and CV analysis. The influence of the mass fraction of graphene (1, 2, 3 and 10 % wt.) in the polymer matrix on electro-polymerization rate is shown in Figure 9 [46]. As can be seen, the electron exchange is faster with increasing the mass fraction of the nanofiller. This is result of

increasing of electrical conductivity of the nanocomposite.

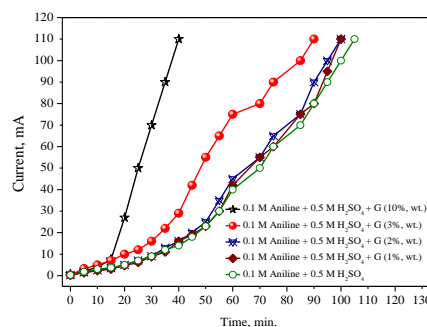


Fig. 9. Steady-state polarization curves for aniline with addition of different quantity of graphene.

Finally, two different pathways of introducing the graphene in the polymer matrix and their impact on the rate of polymerization were studied. The first pathway was introducing the graphene in PANI matrix through it previously being deposited on a platinum electrode, and subsequently PANI being deposited on a graphene film. The second pathway was introducing the graphene in the electrolyte and their mutual depositing with PANI on the platinum electrode. These results are shown in Figure 9. As it can be seen, the polymerization rate of the nanocomposites is higher when the nanostructure was previously deposited on a platinum electrode. This is attributed to the larger active surface area created on the platinum electrode, due to the presence of graphene [47, 48]. In contrary, when graphene was introduced in the electrolyte, the polymerization rate is lower, due to the fact that an induction period is necessary at first, to create a rough surface which would have a role of incipient and would initiate the polymerization process. Related to this, from the morphological aspect of the nanocomposites, using a first pathway of introducing the CNSs in the polymer matrix, a layer by layer structure is created, and the benefits of the carbon nanostructure do not come to the fore. Using the second pathway, when the CNSs are introduced in the electrolyte, compact nanocomposite with uniform distribution of CNSs trough the PANI matrix is produced, and a better material is obtained [5].

4. CONCLUSIONS

The investigations in this study were motivated by the idea to produce PANI/graphene nanocomposites by electrochemical polymerization, aimed for application in the manufacturing of sensors. The influences of the different process conditions were examined. According to the

presented results, the following conclusions can be drawn:

1. According to SEM/EDS analysis, purification of the graphene with H₂O₂ and HF leads to a wrinkled structure that causes sheet folding, while modification with strong acid solutions (H₂SO₄ + HNO₃), leads to edges cutting and gives more uniform form of the flakes. Also, the observed oxidized edges at the graphene flakes can be attributed to the formation of some amide and carbamide groups with hydroxyl and carboxyl groups. This is useful for application of graphene in some electrochemical devices.

2. CV measurements have shown that the presence of graphene in the electrolyte intensifies the growth of the nanocomposite on the electrode. Graphene acts as an incipient in the system because of its large specific surface area and accelerates the reaction rate. Incorporation of only 3 % chemically modified graphene in the polymer matrix, can improve the electrochemical behavior of the system (current density – electro-polymerization rate) up to several times.

3. Steady state polarization measurements confirmed that graphene acts as an incipient in the electro-polymerization process, but that purification does not have a great effect on the polymerization rate. The chemical modification of the CNSs surface have shown higher and more uniform polymerization rate and the polymerization rate is almost double than pure PANI. This also confirms that chemical modification of the graphene surface, improves the conductivity and stability of the material better than only purified graphene. This is due to the carboxyl and hydroxyl groups which allows better interactions with the polymer matrix and confirms previously stated conclusions from SEM/EDS and CV analysis.

4. From the results, the impact of graphene on the electrical conductivity of the nanocomposites can also be assessed. And here confirmed is that by increasing the graphene mass fraction from 1%, 2%, 3% up to 10 %, the electron exchange becomes faster, thus increasing the electrical conductivity of the nanocomposite.

5. Through analyzing the different pathways of introduction of graphene in the polymer matrix and their impact on the polymerization rate, it has been confirmed that the polymerization rate of the nanocomposites is greater when the nanostructure is previously deposited on a platinum electrode.

Acknowledgements: This research was performed under the FP7 Project COMMON SENS - "Cost-effective sensors, interoperable with international

existing ocean observing systems to meet EU policies requirements" (Project reference 614155).

REFERENCES

1. H. S. Nalwa, Handbook of Organic Conductive Molecules and Polymers. Wiley, New York, 1–4, 1997.
2. E. Hermelin, J. Petitjean, S. Aeiyaich, J. C. Lacroix, P. C. Lacaze, *J. App. Electrochem.*, **31**, 905 (2001).
3. C. H. Chen, *J. Appl. Polym. Sci.*, **89**, 2142 (2003).
4. M. Angelopoulos, R. Dipietro, W. G. Zheng, A. G. MacDiarmid, A. J. Epstein, *J Synth Met.*, **84**, 35 (1997).
5. R. Ansari, M. B. Keivani, *E-J Chem.*, **3**, 202 (2006).
6. J. Huang, S. Virji, B. Weiller, R. B. Kaner, *Chem. A Eur. J.*, **10**, 1314 (2004)
7. H. Pingsheng, Q. Xiaohua, L. Chune, *Synth. Met.*, **57**, 5008 (1993).
8. K. G. Neoh, E. T. Kang, S. H. Khor K. L Tan, *Polym. Deg. Stab.*, **27**, 107 (1990).
9. M. Angelopoulos, A. Ray, A. G. Macdiarmid, A. J. Epstein, *J. Synth. Met.*, **21**, 21 (1987).
10. G. M. Morales, M. C. Miras, C. Barbero, *Synth. Met.*, **101**, 686 (1996).
11. S. H. Kim, J. H. Seong, *J. Appl. Polym. Sci.*, **83**, 2245(2002).
12. P. Gajendran, R. Saraswathi, *Pure Appl. Chem.*, **80**, 2377 (2008).
13. B. Lakard, G. Herlem, S. Lakard, R. Guyetant, *Polym.*, **46**, 12233 (2005).
14. N. Liu, F. Luo, H. Wu, Y. Liu, C. Zhang, Y. Chen, *Adv. Funct. Mater.*, **18**, 1518 (2008).
15. T. Wei, G. Luo, Z. Fan, C. Zheng, J. Yan, C. Yao, W. Li, C. Zhang, *Carbon*, **47**, 2296 (2009).
16. C. Schwandt, T. A. Dimitrov, J. D. Fray, *J. of Electroanal. Chem.*, **647**,150 (2010).
17. C. Panatarani, N. Muthahhari, A. Rianto, J. M. Joni, *AIP Conf. Proc.*, **1719**, 030022 (2016).
18. E. Bekyarova, M. E. Itkis, P. Ramesh, C. Berger, M. Sprinkle, W. A. de Heer, R. C. Haddon, *J. Am. Chem. Soc.*, **131**, 1336 (2009).
19. M. Alanyahoglu, J. J. Segura, J. Oró-Solè, N. Casañ-Pastor, *Carbon*, **50**, 142 (2012).
20. Z. Yanwu, M. Shanthi, C. Weiwei, L. Xuesong, J. W. Suk, R. J. Poots, R. S. Ruoff, *Adv. Mat.*, **22**, 3906 (2010).
21. J. Xie, J. P. Spallas, *Micros. and Microanal.*, **19**, 370 (2013).
22. H. Zhang, P. X. Feng, *Carbon*, **48**, 359 (2010).
23. D. W. Boukhvalov, M. I. Katsnelson, *Nano Lett.*, **8**, 4373 (2008).
24. A. S. Mildvan, M. C. Scrutton, M. F. Utter. *J. Biol Chem.*, **241**, 3488 (1996).
25. C. E. Bowen, E. Rouscher, L. L. Ingraham, *Arch. Biochem Biophys.*, **125**, 865 (1968).
26. S. Pruneanu, E. Veress, I. Marian, L. Oniciu, *J. Mater. Sci.*, **34**, 2733 (1999).
27. K. H. Hassan, N. F. Atta, A., *Int. J. Electrochem. Sci.*, **7**, 11161 (2012).
28. J. Gu, S. Kan, Q. Shen, J. Kan, *Int. J. Electrochem. Sci.*, **9**, 6858 (2014).

29. B. O. Taranu, E. Fagadar-Cosma, I. Popa, N. Plesu, I. Taranu, *Digest J. Nanomat. and Biostruct.*, **9**, 667 (2014).
30. E. Genies, M. Lapkowski, J. Penneau, *J. Electroanal. Chem. Interfac. Electrochem.*, **249**, 97 (1988).
31. J. Q. Dong, Q. Shen, *J. Polym. Sci. Part B: Polym. Phys.*, **47**, 2036 (2009).
32. L. M. Da Silva, L. A. De Faria, J. F. C. Boodts, *Electrochim. Acta*, **47**, 395 (2001).
33. C. Peng, S. Zhang, D. Jewell, G. Z. Chen, *Prog. Nat. Sci.*, **18**, 777 (2008).
34. J. Zheng, H. Ma, X. He, M. Gao, G. Li, *Procedia Eng.*, **27**, 1478 (2012).
35. A. Kumar, V. Kumar, K. Awasthi, *J. of Polym. Plastics. Techn. and Eng.*, **57**, 70 (2017).
36. A. O. Al-Hartomy, A. A. Al-Ghamdi, A. S. F. Al Said, N. Dishovsky, R. Shtarkova, V. Iliev, *Appl. Polym. Comp.*, **2**, 59 (2014).
37. J. Zhu, H. Gu, Z. Luo, N. Haldolaarachige, D. P. Young, S. Wei, Z. Guo, *Langmuir*, **28**, 10246 (2012).
38. O. K. Park, N. H. Kim, G. H. Yoo, K. Y. Rhee, J. H. Lee, *Comp. Part. B: Eng.*, **41**, 2 (2010).
39. J. C. García-Gallegos, I. Martín-Gullón, J. A. Conesa, Y. I. Vega-Cantú, F. J. Rodríguez-Macías, *Nanotech.*, **27**, 015501 (2016).
40. A. Petrovski, P. Paunović, R. Avolio, M. E. Errico, M. Cocca, G. Gentile, A. Grozdanov, M. Avella, J. Barton, T. A. Dimitrov, *Mat. Chem. Phys.*, **185**, 83 (2017).
41. H. Yang, A. Bard, *J. Electroanal. Chem.*, **339**, 423 (1997).
42. S. Mu, J. Kan, J. Lu, L. Zhuang, *J. Electroanal. Chem.*, **446**, 107 (1998).
43. A. Malinauskas, J. Malinauskienė, *CHEMIJA*, **16**, 1 (2005).
44. N. Gospodinova, L. Terlemezyan, *Prog. Polym. Sci.*, **23**, 1443 (1998).
45. S. Niyogi, E. Bekyarova, M. E. Itkis, J. L. McWilliams, M. A. Hamon, R. C. Haddon, *J. Am. Chem. Soc.*, **128**, 7720 (2006).
46. N. H. Alamusi, F. Hisao, A. Satoshi, L. Yaolu, L. Jinhua, *Sens.*, **11**, 10691 (2011).
47. E. N. Konyushenko, J. Stejskal, M. Trchová, J. Hradil, J. Kovářová, J. Prokeš, M. Cieslar, J. Y. Hwang, K. H. Chen, I. Sapurina, *Polym.*, **47**, 5715 (2006).
48. Y. K. Zhou, B. L. He, W. J. Zhou, H. L. Li, *J. Electrochem. Soc.*, **151**, 1052 (2004).

Quaternary ammonium bromides as mild steel corrosion inhibitors in acid media

A. K. Popova*¹, A. A. Vasilev², N. Ivanova¹

¹Department of Physical Chemistry, University of Chemical Technology and Metallurgy, 8 “Kl. Ohridski” blvd., 1756 Sofia, Bulgaria

²Department of Pharmaceutical and Applied Chemistry, Faculty of Chemistry and Pharmacy, University of Sofia, 1 “James Baucher” blvd., 1126 Sofia, Bulgaria

Received December 16, 2019; Accepted January 22, 2020

Three quaternary ammonium bromides are used as inhibitors of mild steel corrosion in 1 M. Their behavior is studied with the application of gravimetric and potentiodynamic voltammetry methods. Additional gravimetric experiments are carried in 1 M aiming a comparison of the protective properties observed. Data referring to the adsorption of the compounds studied is obtained. It is found that it is well described by Frumkin adsorption isotherm. The information summarized leads to the conclusion that the inhibitive properties of the bromides investigated depend on their concentration and molecular structure.

Keywords: mild steel, acid corrosion, acid inhibition, adsorption

INTRODUCTION

Corrosion is a thermodynamically determined spontaneous process which proceeds most often following an electrochemical mechanism. It is based on two partial reactions – an oxidation of the metal and a reduction of the oxidizing agent [1-3].

The enormous material losses in the field of industry caused by corrosion make the latter a significant economic problem. That is why the elaboration of methods for corrosion protection is a research trend of great priority.

The use of corrosion inhibitors is an approach of great importance [4-6]. The efficiency of the compounds used as inhibitors depends directly on their molecular structure and ability to form a protective layer on the metal surface. In an acid medium the inhibition is exercised by a layer of the inhibitor's adsorbed molecules. The elucidation of a connection between the protective properties and the molecular structure of the organic substances used as inhibitors in aqueous acid solutions is of a profound interest [7-30].

Our former investigation show that the inhibitor activity depends essentially on the area of the adsorbed molecule and the spatial disposition of its substituents [31-34]. The effect of the electronic structure becomes evident when the behavior of inhibitors of approximately identical molecular area and planar structure is comparatively considered [33].

It is found that compounds of the group of the quaternary ammonium salts provide very good

protective properties [35-49]. This determines our interest and focus on them. The present communication refers to the continued investigation of the inhibiting properties of quaternary ammonium bromides in case of mild steel corrosion in 1 M and 1 M [34,50]. The molecular structure of the substances studied is chosen to outline the effect of the adsorbed species area through comparing the behavior of molecules of a different size and that of the electronic structure by juxtaposing compounds discriminated by the presence of S or O atom (Table 1). The compounds used in this investigation are specifically synthesized and studied for the first time as inhibitors in correspondence with the views pointed above [51].

EXPERIMENTAL

The mild steel used had the following chemical composition (wt%): 0.16 C, 0.35 Mn, 0.016 Si, 0.01 P, 0.029 S, 0.06 Cr, 0.10 Cu and Fe to balance the content.

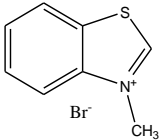
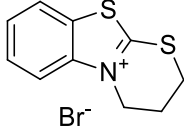
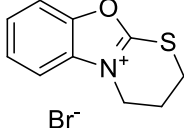
All compounds investigated (Table 1) were purified to an analytical purity grade confirmed by an elemental analysis and ¹H-NMR [51]. 1 M HCl and 1 M H₂SO₄ solutions were prepared using 35% HCl and 98% H₂SO₄ (pure for analysis) and doubly distilled water.

Two classical techniques were used to determine the corrosion inhibitor characteristics of the quaternary ammonium bromides – gravimetry and potentiodynamic voltammetry.

* To whom all correspondence should be sent.

E-mail: apopova@uctm.edu

Table 1. Investigated quaternary ammonium salts as inhibitors

| Compounds | Structural formulae | Abbre- viation | Molar mass |
|--|--|----------------|------------|
| 3-Methylbenzo[<i>d</i>]thiazol-3-ium bromide |  | MTB | 230.1 |
| 3,4-Dihydro-2H-benzo[4,5]thiazolo[2,3-b][1,3]thiazin-5-ium bromide |  | SS | 288.9 |
| 3,4-Dihydro-2H-benzo[4,5]oxazolo[2,3-b][1,3]thiazin-5-ium bromide |  | OS | 272.2 |

The gravimetric measurements were carried out at definite time intervals of 24h [34, 52] at a room temperature ($20 \pm 2^\circ\text{C}$) using an analytical balance (precision of ± 0.1 mg). The specimens of an area of 11.3 cm^2 were of a round shape to avoid edges effects attributed to high-speed corrosion proceeding. The preliminary treatment included pickling in a solution containing concentrated HNO_3 and H_2SO_4 at a volume ratio of 2:1, washing with distilled water and an ethanol-ether mixture. Three specimens were immersed simultaneously in every beaker containing 250 mL of the test solution.

The potentiodynamic polarization experiments were carried out in a conventional three-compartment electrochemical cell. A mild steel cylinder pressed into a Teflon holder served as a working electrode (WER). Its working area of 0.5 cm^2 remained precisely fixed. A saturated calomel electrode (SCE) connected through a salt bridge was used as a reference electrode, while platinum sheet acted as counter electrode. Prior to each experiment the WE was wet abraded with 600-grade emery paper, rinsed with distilled water and an ethanol-ether mixture. Then it was inserted immediately into the glass cell which contained 250 mL of the test solution.

EG&G Instruments PAR model 273 potentiostat monitored by an IBM personal computer via a GPIB-IIA interface and M342 software were used to run the tests as well as to collect and treat the experimental data.

The polarization curves were recorded from ca -250 mV to +130 mV vs. the measured corrosion potential E_{corr} with a scan rate of 0.2 mV/s starting one minute after the immersion of the WE in the test solution. The anodic (b_a) and cathodic (b_c) Tafel constants, the corrosion potential (E_{corr}) and

the corrosion current density (j_{corr}) were determined using PARCalc342 data analysis technique (based on the Stern-Geary kinetics equation [53]). The polarization resistance R_p was evaluated on the ground of the same polarization curves but using only the range from ± 10 mV vs. E_{corr} .

All plots and calculated parameters were mean values of at least five independent experiments. Standard deviations were also reported.

The inhibitor efficiency IE (%) was calculated from the gravimetric and potentiodynamic measurements using the relations:

$$IE(\%) = \frac{w_0 - w_i}{w_0} \times 100 \quad (1)$$

$$IE(\%) = \frac{j_{\text{corr},0} - j_{\text{corr},i}}{j_{\text{corr},0}} \times 100, \quad (2)$$

where w_0 and w_1 in $\text{g/m}^2\text{h}$ are the average corrosion rates in absence and presence of an inhibitor, while $j_{\text{corr},0}$ and $j_{\text{corr},i}$ are the corresponding corrosion current densities.

RESULTS AND DISCUSSION

3.1. Inhibiting efficiency

3.1.1. Gravimetric tests

The quaternary ammonium salts are studied in 1M HCl and 1M H_2SO_4 solutions of a wide concentration range. The highest possible concentration value is limited by the plateau reached in the corresponding concentration dependence of the inhibiting efficiency or the compound solubility (10^{-3} M for SS and 5×10^{-4} M in case of SO). The mean values of the corrosion rate, w ($\text{g/m}^2\text{h}$), and that the corresponding inhibiting efficiency, IE (%), evaluated in accordance with Eq. (1), are determined for each concentration

studied. Fig. 1 illustrates the results obtained in 1 M HCl medium, while Fig. 2 – those in 1 M H₂SO₄ solution. It is worth noting that the value of the surface coverage degree, θ , is plotted on the ordinate axis assuming that $IE(\%) = \theta \times 100$. The same data is used in adsorption characteristics determination.

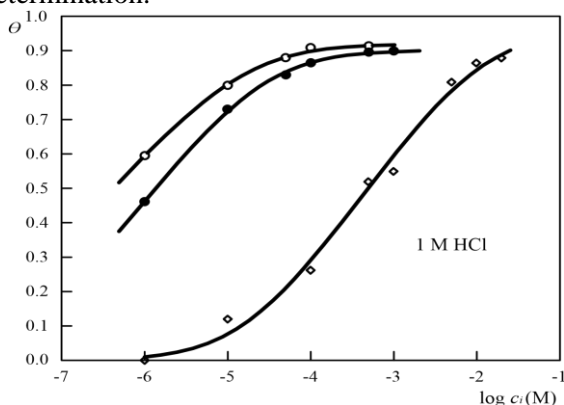


Fig.1. Inhibition efficiency and adsorption isotherms of quaternary ammonium bromides in 1 M HCl - experimental gravimetric data referring to OS (○), SS (●) and MTB (◇) and graphs presenting the adsorption isotherms evaluated.

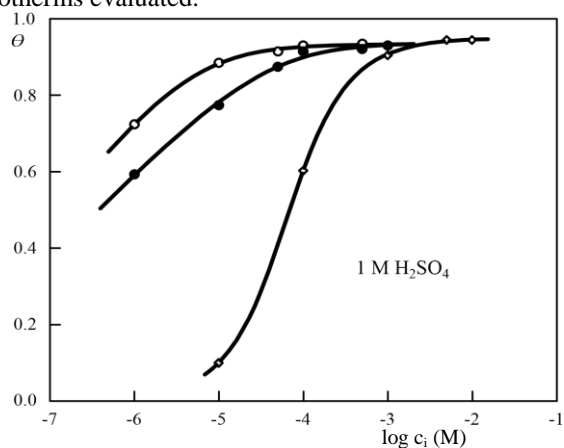


Fig 2. Inhibition efficiency and adsorption isotherms of quaternary ammonium bromides in 1 M H₂SO₄ - experimental gravimetric data referring to OS (○), SS (●) and MTB (◇) and graphs presenting the adsorption isotherms evaluated.

The figures pointed above show that the efficiency of the compounds studied depends on their concentration. It is seen that the protective effect increases initially with the increase of the concentration, c_i . It changes slightly upon reaching a definite concentration value accepted as an optimal one. The latter has a different characteristic value for each inhibitor. The difference in the inhibiting properties of the three compounds is obviously connected with the difference in their

molecular structure. It is more vividly expressed at low and medium concentration values.

The comparison of the inhibitors in 1 M HCl in view of the maximal efficiency reached leads to the following line:

OS (91.5%) \approx SS (90.0%) > MTB (88.0%).

At a concentration of 1×10^{-4} M the line changes to:

OS (91.0%) > SS (86.5%) > MTB (26.0%).

The same line is obtained at lower inhibitor concentrations as well.

The inhibitor's sequence following their highest efficiency in 1 M H₂SO₄ is as follows:

MTB (94.0%) \approx SO (93.0%) \approx SS (92.5%).

At a concentration of 1×10^{-4} M the line changes to:

OS (92.5%) \approx SS (91.0%) > MTB (60.0%)

The line is OS > SS > MTB at lower concentration values.

The results of the gravimetric investigation show that all three compounds have inhibitive properties in 1 M HCl and 1 M H₂SO₄. The latter results are slightly better than those in HCl. The difference is better outlined in presence of MTB.

OS provides the best protective properties in 1 M HCl in the whole concentration range studied. It is also the best inhibitor among those investigated in 1 M H₂SO₄ at the concentration values used. In fact MTB is slightly better but at concentrations higher than OS maximal concentration studied. The latter is in fact insoluble at these MTB concentrations.

The protective properties of OS and SS are quite similar in both media investigated with a slight dominance of OS.

3.1.2. Potentiodynamic voltammetry tests

The potentiodynamic voltammetry investigations are carried out in 1 M HCl at various concentrations of the inhibitors. The polarization curves recorded provide the determination of the electrochemical parameters as the corrosion current density, j_{corr} , the corrosion potential, E_{corr} , the cathodic and anodic Tafel slopes, b_c and b_a , correspondingly, the polarization resistance, R_p . The variation of the electrochemical parameters provides to follow the effect of the inhibitors on the kinetics of the corrosion process. The values obtained are listed in Table 2. Typical polarization curves are shown in Fig.3.

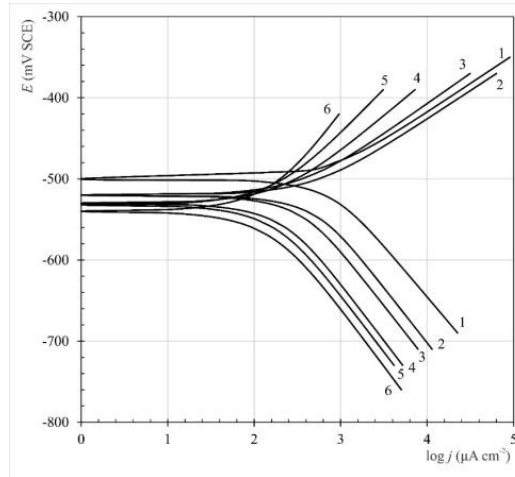


Fig. 3. Potentiodynamic polarization curves in presence of SS: 1 – 1 M HCl; 2 – 1×10^{-6} M; 3 – 1×10^{-5} M; 4 – 1×10^{-4} M; 5 – 5×10^{-4} M; 6 – 1×10^{-3} M.

Table 2. Electrochemical parameters obtained from the polarization curves of bromides studied

Methylbenzo[d]thiazol-3-ium bromide, MTB

| c_i (M) | E_{corr} (mV) | $-b_c$ (mV/dec) | b_a (mV/dec) | j_{corr} ($\mu\text{A}/\text{cm}^2$) | χ^2 | R_p ($\text{k}\Omega \text{ cm}^2$) \square | $j_{corr}^{R_p}$ ($\mu\text{A}/\text{cm}^2$) |
|--------------------|--------------------|--------------------|-------------------|---|---------------|--|---|
| 1MHCl | -498 ± 2 | 126 ± 4 | 71 ± 5 | 700 ± 50 | 5.0 ± 1.5 | 0.0340 ± 0.0050 | 690 ± 48 |
| 1×10^{-5} | -500 ± 3 | 128 ± 5 | 76 ± 7 | 728 ± 44 | 8 ± 3 | 0.0338 ± 0.0080 | 729 ± 61 |
| 1×10^{-4} | -498 ± 2 | 132 ± 5 | 81 ± 6 | 687 ± 45 | 9 ± 3 | 0.0349 ± 0.0071 | 651 ± 39 |
| 1×10^{-3} | -495 ± 1 | 136 ± 6 | 92 ± 4 | 441 ± 18 | 11 ± 2 | 0.0528 ± 0.0078 | 438 ± 21 |
| 5×10^{-3} | -491 ± 3 | 137 ± 4 | 98 ± 5 | 300 ± 14 | 12 ± 3 | 0.0835 ± 0.0063 | 292 ± 10 |
| 1×10^{-2} | -488 ± 1 | 135 ± 5 | 98 ± 3 | 228 ± 6 | 12 ± 4 | 0.1020 ± 0.0058 | 227 ± 7 |
| 2×10^{-2} | -488 ± 1 | 138 ± 4 | 100 ± 2 | 216 ± 4 | 10 ± 2 | 0.1156 ± 0.0049 | 217 ± 5 |

3,4-Dihydro-2H-benzo[4,5]thiazolo[2,3-b][1,3]thiazin-5-ium bromide, SS

| c_i (M) | E_{corr} (mV) | $-b_c$ (mV/de c) | b_a (mV/de c) | j_{corr} ($\mu\text{A}/\text{cm}^2$) | χ^2 | R_p ($\text{k}\Omega \text{ cm}^2$) | $j_{corr}^{R_p}$ ($\mu\text{A}/\text{cm}^2$) |
|--------------------|--------------------|------------------------|-----------------------|---|-------------|--|---|
| 1×10^{-6} | -520 ± 2 | 136 ± 3 | 70 ± 4 | 458 ± 47 | 35 ± 2 | 0.0516 ± 0.0084 | 464 ± 71 |
| 1×10^{-5} | -520 ± 3 | 136 ± 4 | 75 ± 4 | 315 ± 16 | 24 ± 4 | 0.0815 ± 0.0034 | 300 ± 19 |
| 1×10^{-4} | -530 ± 2 | 140 ± 4 | 89 ± 2 | 195 ± 12 | 6 ± 2 | 0.1047 ± 0.0055 | 207 ± 8 |
| 5×10^{-4} | -532 ± 2 | 140 ± 5 | 110 ± 7 | 160 ± 4 | 18 ± 1 | 0.1443 ± 0.0038 | 164 ± 2 |
| 1×10^{-3} | -540 ± 2 | 143 ± 4 | 145 ± 11 | 146 ± 6 | 5.7 ± 2 | 0.1639 ± 0.0050 | 148 ± 12 |

3,4-Dihydro-2H-benzo[4,5]oxazolo[2,3-b][1,3]thiazin-5-ium bromide, OS

| c_i (M) | E_{corr} (mV) | $-b_c$ (mV/de c) | b_a (mV/de c) | j_{corr} ($\mu\text{A}/\text{cm}^2$) | χ^2 | R_p ($\text{k}\Omega \text{ cm}^2$) | $j_{corr}^{R_p}$ ($\mu\text{A}/\text{cm}^2$) |
|--------------------|--------------------|------------------------|-----------------------|---|-------------|--|---|
| 1×10^{-7} | -510 ± 5 | 136 ± 3 | 69 ± 4 | 530 ± 51 | 9 ± 2 | 0.0484 ± 0.0014 | 551 ± 41 |
| 1×10^{-6} | -510 ± 4 | 131 ± 4 | 75 ± 4 | 337 ± 60 | 22 ± 4 | 0.0789 ± 0.0112 | 348 ± 29 |
| 1×10^{-5} | -513 ± 4 | 131 ± 5 | 96 ± 2 | 253 ± 32 | 65 ± 12 | 0.0819 ± 0.0075 | 266 ± 8 |
| 1×10^{-4} | -517 ± 2 | 139 ± 5 | 119 ± 7 | 179 ± 4 | 3 ± 1 | 0.1360 ± 0.0138 | 180 ± 2 |
| 5×10^{-4} | -526 ± 2 | 153 ± 4 | 165 ± 18 | 141 ± 5 | 4 ± 2 | 0.1719 ± 0.0130 | 142 ± 12 |

With concentration increase E_{corr} shifts in a positive direction in presence of MTB, while the presence of SS and OS brings about a shift in the opposite direction. The values of the Tafel slopes, b_c and b_a , increase with the increase of all compounds concentration. The highest values are obtained at the highest concentration of OS. The results pointed above lead to the conclusion that all compounds are in fact general mixed type inhibitors. MTB shows slightly better expressed anodic behavior, while that of SS and OS tends to the cathodic one.

The corrosion current density, which is a measure of the corrosion rate decreases with increase of the inhibitor's concentration, c_i . This is valid for all compounds studied. The inhibiting efficiency, IE (%), is evaluated on the ground of the values of j_{corr} with the application of Eq. (2). The dependence of IE (%) on c_i is presented in Fig. 4. It is evident that the inhibiting effect increases with the concentration increase in case of all compounds studied. This result is in correspondence with the gravimetric findings. It is worth noting that the values of IE (%) found potentiodynamically are generally lower than those obtained gravimetrically. This is most probably due to the different exposure time in the solution – it is 24 h in the course of the gravimetric tests, while the polarization curves are potentiodynamically recorded immediately after the electrode immersion. Irrespective of this difference the sequence of the inhibitors in respect to their efficiency stays unchanged.

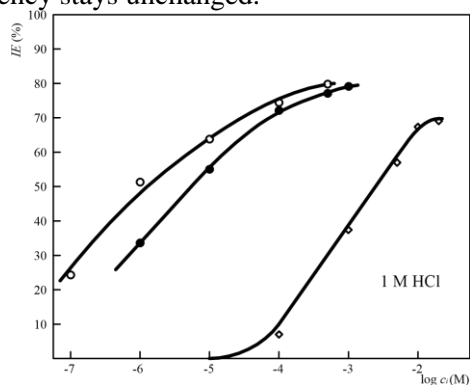


Fig. 4. Dependence of the inhibiting efficiency, IE (%), on the inhibitors concentration, c_i (M) obtained on the ground of the potentiodynamic voltammetric data obtained: OS (\circ), SS (\bullet) and MTB (\diamond).

Thus the inhibitors line obtained on the ground of the highest effect recorded at the highest available concentration is as follows: OS (79.8%) \approx SS (79.19%) $>$ MTB (69.1%).

At a concentration of 1×10^{-4} M the line becomes: OS (74.4%) \approx SS (72.1%) $>$ MTB (10.0%). At lower concentration the difference between the behavior of OS and that of SS becomes more distinct. It has to be underlined that the lines just presented coincide with those obtained gravimetrically in 1 M HCl.

The values of the polarization resistance, R_p , increase with the increase of the compounds' concentration. This is an additional verification of the protective properties improvement. The values of j_{corr} determined on the ground of the R_p - method almost coincide with those evaluated by the Tafel plot-method. This is so because identical polarization curves are used.

The results obtained with potentiodynamic voltammetry application show that OS has the best protective properties in the whole concentration range studied. It is closely followed by SS. It can be concluded that the molecular structure affects also the inhibitive properties displayed.

3.2. Adsorption parameters

The organic substances molecules or ions adsorption on the metal surface is the fundamental cause for decrease of the corrosion rate in an acid medium. The experimental results obtained provide to choose an appropriate adsorption isotherm, whose application leads in turn to the elucidation of some of the peculiarities of the adsorption process taking place.

In this study the degree of fractional surface coverage, θ , is calculated using the kinetic data obtained. The relation $\theta = IE$ (%) / 100 [11, 13, 54] is used. The value of IE (%) is obtained on the ground of the gravimetric measurements as it is assumed that the adsorption/desorption equilibrium is reached within the 24 h of specimens immersion in the solution. The adsorption isotherms of Langmuir, Frumkin and Temkin are usually applied [55] in the field. It is found that Frumkin's isotherm provides the best description of the adsorption data. It is usually presented in the form:

$$Bc = \frac{\theta}{1-\theta} \exp(-2a\theta), \quad (3)$$

where θ is the fractional surface coverage, a is the interaction parameter, c is the concentration, while B is an adsorption parameter, which has the meaning of the adsorption/desorption equilibrium constant. B is related to the standard free energy of adsorption, ΔG_{ads}^0 , in correspondence with the equation:

$$B = \frac{1}{55,5} \exp\left(-\frac{\Delta G_{ads}^0}{RT}\right) \quad (4)$$

The adsorption parameters are evaluated using the non-linear procedure based on the least squares method described in ref. [54]. The experimental points and the curves of the adsorption isotherms

calculated are shown in Figs. 1 and 2. It is seen that the curves correspond well to the experimental points. This is also evident from the values of the standard deviation. They, as well as all other adsorption parameters obtained for both acidic solutions used, are summarized in Table

3.

Table 3. Adsorption parameters determiner for quaternary ammonium bromides as inhibitors of mild steel corrosion.

| Compounds | MTB | SS | OS |
|--|----------------------|----------------------|----------------------|
| 1 M HCl | | | |
| log <i>B</i> | 4.04 | 6.76 | 7.48 |
| <i>a</i> | 1.54 | 1.65 | 2.17 |
| ΔG_{ads}^0 , kJmol ⁻¹ | -32.4 | -47.7 | -51.7 |
| Standard Deviation | 3.2x10 ⁻² | 5.1x10 ⁻³ | 5.5x10 ⁻³ |
| $-\log c_{\theta=0.5}$ | 4.71 | 7.47 | 8.42 |
| 1M H₂SO₄ | | | |
| log <i>B</i> | 4.04 | 7.86 | 7.90 |
| <i>a</i> | - 0.35 | 2.97 | 2.02 |
| ΔG_{ads}^0 , kJmol ⁻¹ | -32.5 | -53.88 | -54.11 |
| Standard Deviation | 2.5x10 ⁻³ | 8.4x10 ⁻² | 3.7x10 ⁻³ |
| $-\log c_{\theta=0.5}$ | 3.89 | 9.15 | 8.78 |

The interaction constant *a* has positive values for all compounds investigated in 1 M HCl. This indicates the presence of forces of attraction between the species adsorbed, which in fact facilitate the further adsorption proceeding in the monolayer.

The results referring to H₂SO₄ medium are similar. MTB is the only exclusion as constant *a* has a negative value (*a* = - 0.35) in this case. This is most probably due to *a* compensation effect - the attraction observed between the molecules adsorbed on the metal surface is partially compensated by the latter energetic inhomogeneity. This provides the formal validation of the Langmuir isotherm although the assumptions required in the course of its derivation are not present.

The values of ΔG_{ads}^0 are negative for all substances in both media investigated. This is a thermodynamic verification of the fact that the adsorption is spontaneously proceeding.

The juxtaposition of the inhibitors in view of the absolute value of ΔG_{ads}^0 obtained in their presence results in the following lines: OS > SS > MTB in 1 M HCl, while OS ≈ SS > MTB in 1 M H₂SO₄ medium. The same lines are obtained if the values of log*B* are taken into account. It is worth adding that this type of arrangement corresponds to the one

obtained on the ground of the inhibitor efficiency observed at a concentration value of 1x10⁻⁴ M.

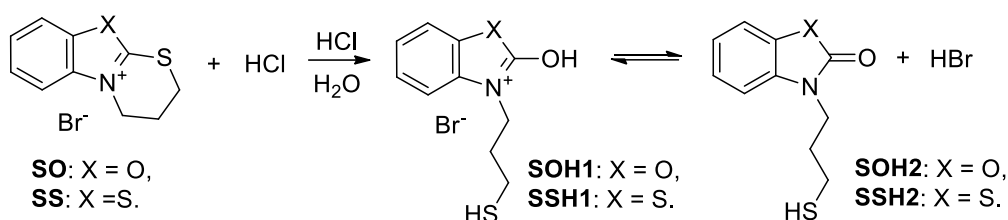
3.3. On the inhibiting activity/molecular structure relation

The different inhibiting properties shown by the three compounds obtained in the course of study with the application of different methods are due to the difference in their molecular structure.

The quaternary ammonium bromides dissociate in acidic solutions giving ammonium cations and a bromine anion, Br⁻. We assume that the cation structure determines the difference of the inhibitive properties. The effect of Br⁻ presence in the solution cannot be excluded because of this anion disposition to specific adsorption on the metal surface [4, 5]. This can result to a change of the surface charge or a synergistic effect, i.e. Br⁻ contribute to the inhibiting effect observed. On the other hand, Br⁻ can favor the adsorption by decreasing the cations repulsion in the adsorption layer (the positive values of the interaction adsorption parameter indicate actual attraction in the adsorption layer).

We assume that the juxtaposition of MTB on one hand and SS and OS on the other can outline the effect of the adsorbed species surface area (in fact of the cationic part in this case), while the

comparison between SS and OS can illustrate the dependence on the electron structure as both compounds have an almost identical surface area (the difference is determined by the dimensions of the S and O atom present). The experimental results show that MTB is a weaker inhibitor when compared to SS and OS at an identical concentration. This is most probably due to the smaller surface of its cationic part. The protective properties of OS are better than those of SS but the difference observed decreases with concentration increase. In view of the molecular structure only (Table 1) the inhibiting properties should be identical or a slightly better performance can be expected in case of SS as the S atom is a better electron couple donor when compared with the O atom.



Scheme 1

Furthermore the presence of the basic form of SS and OS in the solution cannot be excluded (the dihydrothiazonium ring is not ruptured in this case). The dynamic equilibria of the three forms of the compounds, i.e. SO, SOH1 and SOH2 on one hand, and SS, SSH1 and SSH2 on the other, determine the difference in the inhibitive properties displayed. Most probably they also affect the solubility observed.

At this stage of our investigations we assume a probability of Br^- specific adsorption on the metal surface in both acidic solutions. This brings about a negative charge to the surface and explains the relatively close inhibiting efficiency in both acids. This effect can also favor the physical adsorption of the molecules cationic part.

CONCLUSIONS

The three compounds investigated show protective properties in case of mild steel corrosion in 1 M HCl and 1 M H_2SO_4 . Their inhibiting effect increases with their concentration increase. OS acts as the best inhibitor in the concentration range from 1×10^{-6} M. It is closely followed by SS.

The adsorption of two of the bromides on the metal surface is described by the adsorption isotherm of Frumkin or that of Langmuir (MTB in 1 M H_2SO_4). Positive values of the constant of interaction are found in most of the cases, which

Why is this unexpected effect of the electronic structure? The cationic part of SS refers to a benzothiazole heterocycle containing fused dihydrothiazinium heterocycles at positions 2 and 3, while the cationic part of SO consists of a benzoxazole heterocycle with fused dihydrothiazinium heterocycle at the same positions, i.e. the substituents and their positions are identical. The dihydrothiazinium ring ruptures under the effect of the acidic aqueous medium and a propanethiole substituent appears at position 3 in the basic heterocycle of OS and SS. Thus two tautomeric forms appear which stay in a dynamic equilibrium. The first one refers to oxazole (SOH1) and oxazolone (SOH2), while the second one - to thiazole (SSH1) and thiazolone (SSH2).

indicates that the species adsorbed attract the adsorbing one facilitating the adsorption itself.

The results obtained show that the molecular structure affects essentially the inhibitive properties when compared at identical concentrations. It is not possible to conclude explicitly which parameters of the molecular structure are of predominating importance. In the case studied OS and SS change their structure and in fact three different species take part in the adsorption proceeding. We assume that physical adsorption of the molecules cationic parts takes place at the negatively charged metal surface.

REFERENCES

1. L. L. Shrier (ed.), Corrosion, Metallurgia, Moscow, 1981.
2. N. P. Zhuk, Course of Corrosion and Metal Protection (Russ.), Metallurgia, Moscow, 1976.
3. P. R. Roberge, Handbook of Corrosion Engineering, McCrow-Hill, N.Y., 2000.
4. S. M. Reshetnikov, Acid Corrosion Inhibitors of the Metals (Russ.), Khimia, Leningrad, 1986.
5. I.L. Rozenfeld, Corrosion inhibitors (Russ.), Khimiya, Moscow, 1977.
6. L.I. Antropov, E. M. Makushin, V. F. Panasenko, Metal Corrosion Inhibitors (Russ.), Technika, Kiev, 1981.
7. Z.A. Foroulis, in: Proceedings of 6th European Symposium on Corrosion Inhibitors, Ann. Univ. Ferrara, N. S. Sez. V, Suppl. N8, 1985.

8. F. Zucchi, G. Trabaneli, in: Proceedings of 7th European Symposium on Corrosion Inhibitors, Ann. Univ. Ferrara, N. S. Sez. V, Suppl. N9, 1990.
9. R.C. Ayers, N. Hackerman, J. Electrochem. Soc., **110**, 507 (1963).
10. T. Szauder, A. Brandt, Electrochim. Acta, **26**, (1981) 1209-1217.
11. J. de Damborenea, J. M. Bastidas and A. J. Vázquez, Electrochim. Acta, **42**, 455 (1997).
12. D.A. Lopez, S.N. Simison, S.R. de Sanchez, Electrochim. Acta, **48**, 845 (2003).
13. G. Moretti, G. Quartarone, A. Trassan, A. Zingales, Electrochim. Acta, **41**, 1971 (1996).
14. E. Garcia-Ochoa, J. Genesca, Surf. Coat. Technol., **184**, 322 (2004).
15. S.L. Li, Y.G. Wang, S.H. Chen, R. Yu, S.B. Lei, H.Y. Ma, De X. Lin, Corros. Sci., **41** 1769 (1999).
16. K. Babić-Samardžija, N. Hackerman, J. Solid State Electrochem., **9**, 483 (2005).
17. H. L. Wang, R.-B. Liu, J. Xin, Corros. Sci., **46**, 2455 (2004).
18. M. Özcan, I. Dehri. M. Erbil, Appl. Surf. Sci., **236**, 155 (2004).
19. H. Keleş, M. Keleş, I. Dehri, O. Serindağ, Colloids Surf. A: Physicochem. Eng. Aspects, **320**, 138 (2008).
20. M.S. Morad, Corros. Sci., **50**, 436 (2008).
21. E. Chaieb, A. Bouyanzer, B. Hammouti, M. Benkaddour, Appl. Surf. Sci., **246**, 199 (2005).
22. A. Dutta, S. K. Saha, P. Banerjee, D. Sukul, Corros. Sci., **98**, 541, (2015).
23. H. Zarrok, A. Zarrouk, R. Salghi, B. Elmahi, B. Hammouti, S.S. Al-Deyab, M. Ebn Touhami, M. Bouachrine, H. Oudda, H. Boukhris, Int. J. Electrochem. Sc., **8**, 11474 (2013).
24. Ostapenko, G.I., Gloukhov, P.A., Bunev, A.S., Corros. Sci., **82**, 265 (2014).
25. A. S. Fouda, A. H. Soliman, Prot. Met. and Phys. Chem. of Surfaces, **51**, 847 (2015).
26. I. B. Obot, A. Madhankumar, S.A. Umoren, Z. M. Gasem, J. Adhes. Sci. Technol., **29**, 2130, (2015).
27. H. M. Abd El-Lateef, Corros. Sci., **92**, 104, (2015).
28. D. Zhang, Y. Tang, S. Qi, H. Cang, G., Corros. Sci., **102**, 517, (2016).
29. E. Gutiérrez, J. A. Rodríguez, J. Cruz-Borbolla, J. G. Alvarado-Rodríguez, P. Thangarasu, Corros. Sci., **108**, 23 (2016).
30. A. Stoyanova, E. Slavcheva, Mater. Corros., **62**, 872 (2011).
31. A. Popova, M. Christov, S. Raicheva, E. Sokolova, Corros. Sci., **46**, 1333 (2004).
32. A. Popova, M. Christov, T. Deligeorgiev, Corrosion, **59**, 756, (2003).
33. A. Popova, M. Christov, A. Zwetanova, Corros. Sci., **49**, 2131, (2007).
34. A. Popova, M. Christov, A. Vasilev, A. Zwetanova, Corros. Sci. **53**, 679, (2011).
35. G. Schmitt, in: Proceedings of 6th European Symposium on Corrosion Inhibitors, Ann. Univ. Ferrara, N. S. Sez. V, Suppl. N. 8, 1985.
36. G. Schmitt, K. Bedburg, in: Proceedings of 9th International Congr. Metallic Corrosion, Toronto, 1984, p. 112.
37. K.F. Khaled, Appl. Surface Sci., **236**, 307 (2004).
38. L. Tang, X. Li, G. Mu, G. Liu, L. Li, H. Liu, Y. Si, J. Mater. Sci., **41**, 3063 (2006).
39. M.M. Saleh, A.A. Atia, J. Appl Electrochem., **36**, 899, (2006).
40. M.M. Saleh, Mat. Chem. Phys., **98**, 83, (2006).
41. L.G. Qiu, Y. Wu, Y.M. Wang, X. Jiang, Corros. Sci., **50**, 576, (2008).
42. X. Li, L. Tang, H. Liu, G. Mu, G. Liu, Mater. Lett., **2**, 2321, (2008).
43. A.A. Hermas, M.S. Morad, M.H. Wahdan, J. Appl. Electrochem., **34**, 95, (2004).
44. H. Ashassi-Sorkhabi, M. Es'haghi, Mat. Chem. Phys., **114**, 267, (2009).
45. R. Fuchs-Godec, Electrochim. Acta, **54**, 2171, (2009).
46. M. A. Hegazy, A. A. Nazeer, K. Shalabi, J. Mol. Liq., **209**, 419, (2015).
47. M. A. Hegazy, M. Abdallah, M. K. Awad, M. Rezk, Corros. Sci., **81**, 54 (2014).
48. M. A. Hegazy, A. M. Badawi, S. S. Abd El Rehim, W. M. Kamel, Corros. Sci., **69**, 110, (2013).
49. P. Mourya, P. Singh, A. K. Tewari, R. B. Rastogi, M. M. Singh, Corros. Sci., **95**, 71 (2015).
50. A. Popova, M. Christov, A. Vasilev, Corros. Sci., **49**, 3276, (2007).
51. T. Deligeorgiev, N. Gadjev, A. Vasilev, R. Drexhage, S. Yarmoluk, Dyes and Pigments, **70**, 185 (2006).
52. A. Popova, S. Veleva, S. Raicheva, React. Kinet. Catal. Lett., **85**, 99, (2005).
53. M. Stern, A.L. Geary, J. Electrochem. Soc., **104**, 56 (1957).
54. M. Christov, A. Popova, Corros. Sci., **46**, 1613, (2004).
55. B. Damaskin, O. A. Petrii, V. V. Batrakov, Organic Compounds Adsorption on Electrodes (Russ.), Metalurgia, Moscow, 1976.

Electrochemical impedance and dielectric spectroscopy study of TiO₂-nanofilled PEO/PVP/NaIO₄ ionic polymer electrolytes

Y. G. Marinov^{1*}, G. B. Hadjichristov¹, T. E. Vlakhov¹, H. K. Koduru^{2,3}, N. Scaramuzza³

¹*Georgi Nadjakov Institute of Solid State Physics, Bulgarian Academy of Sciences, 72 Tzarigradsko Chaussee Blvd., BG-1784 Sofia, Bulgaria*

²*Department of Physics, Madanapalle Institute of Technology & Science (MITS), Madanapalle, Andhra Pradesh, IN-517325, India*

³*Dipartimento di Fisica, Università degli Studi della Calabria, Via P. Bucci, Cubo 33B, Rende (CS), IT-87036, Italy*

Received November 08, 2019; Accepted January 03, 2020

We have experimentally investigated the ion-conducting and dielectric properties of nanocomposite ion-conductive polymer electrolytes based on two-polymer blend of poly(ethylene oxide) (PEO) and polyvinyl pyrrolidone (PVP), with added sodium metaperiodate (NaIO₄) at concentration of 10 wt%. The polymer-ion complexes PEO/PVP/NaIO₄ are doped with small amount (up to 3 wt%) TiO₂ nanoparticles of average size ~ 10 nm. Chemically-stable free-standing thin films (150 μm) of the synthesized PEO/PVP/NaIO₄/TiO₂ solid-state polymer electrolyte material are formed by using conventional solution-cast technique. The electrical and dielectric properties of these nanocomposites are studied by complex electrical impedance and dielectric spectroscopy over the frequency range 1 Hz – 1 MHz. The ionic conductivity of TiO₂-nanofilled PEO/PVP/NaIO₄/TiO₂ is determined as dependent on the concentration of the included TiO₂ nanoparticles. The obtained results indicate that both the Na⁺-ion conductivity and the dielectric function of PEO/PVP/NaIO₄/TiO₂ nanocomposite electrolytes are enhanced upon addition of TiO₂ nanoparticles. Thus, the produced NaIO₄ salt-complexed TiO₂-nanofilled ionic polymer electrolytes are attractive for use in sodium ion secondary batteries, electrochemical applications, as well as in organic electronics.

Keywords: conductivity; electrical impedance spectroscopy; dielectric spectroscopy.

INTRODUCTION

In view of the outstanding technological achievements in the multidisciplinary scientific & industrial fields, the polymer nanocomposite electrolytes (NCPEs) have been gaining vital significance owing to their unique useful properties [1]. Various nano-size inorganic fillers (such as zinc oxide, alumina, titania, silica, graphene oxide, MgO, MgAl₂O₄, γ-LiAlO₂) have been employed to fabricate NCPEs having improved properties [2–10]. Thus, one can even obtain multifunctional nanocomposite materials having versatile applications. Generally, the incorporation of proper nanoparticles (NPs) into suitable polymer matrix may substantially improve the electrical performance of the resultant polymer-based nanocomposite without sacrificing the mechanical strength of the material. In fact, this effect in polymer nanocomposites occurs due to specific interfacial interactions between the included NPs and polymer chains. In polymer nanocomposites the role of the interface is related to a fundamental length-scale in the order of the radius of gyration of the polymer chains. As a result, synergetic interactions arise in the ‘nanoscopically confined interfacial nanocomposite matrix’ and contribute to

the enhancement of the segmental mobility, electrical and mechanical properties. The same effect of interfacial interactions in nanometer ranges between polymer chains and inorganic nanofillers with high surface area takes place in NCPEs. The nanofiller-polymer interactions and possible conformational changes in the host polymer lead to increased mobility of mobile ions in amorphous phase regions in the polymer matrix of NCPEs [1,6,10–12].

Solid polymer electrolytes based on poly(ethylene oxide) (PEO) and complexed with various alkali metal salts have been recognized as permissible systems to be employed in solid state rechargeable batteries and polymer electronics [13,14]. Substantial research efforts are currently in progress to enhance the properties of the Na-ion-conducting polymer electrolytes and to search of novel Na-ion-conductor materials in order to satisfy the requirements for efficient electrolyte function and for other advanced applications. Various Na salt-complexed PEO-based polymer electrolytes intended to be used for Na⁺ battery and other applications have been reported [15–18]. Also, there are numerous investigations on Na⁺-ion-conducting polymer electrolyte systems based on blends of PEO with the high-amorphous polymer polyvinyl pyrrolidone (PVP), as complexed with

* To whom all correspondence should be sent.
E-mail: ymarinov@issp.bas.bg

various sodium salts [19–23]. The blending of PEO with PVP reduces the degree of crystallinity of polymer matrix, thus enhancing the ionic conductivity. Thus, PEO/PVP complexed with the ionic compound sodium metaperiodate (NaIO₄) showed ion-electrolytic properties attractive for electrochemical and other applications [22,23].

The next step is the reinforcement of these polymer electrolyte systems by doping with nano-sized material in order to properly modify their properties and further enhance their ion conductivity. In the present work, our investigations are focused on PEO/PVP blend based electrolyte system complexed with the ionic compound NaIO₄ and doped with nano-sized TiO₂. In particular, TiO₂ NPs were incorporated at concentration of 1, 2 and 3 wt% in PEO(70 wt%)/PVP(30 wt%) polymer blend complexed with 10 wt% NaIO₄. The effect of the inclusion of TiO₂ NPs in the PEO/PVP/NaIO₄ on the ion (Na⁺) conductivity and dielectric properties of the resulting NCPEs was studied by means of electrochemical impedance spectroscopy (EIS) and dielectric spectroscopy.

EXPERIMENTAL

PEO and PVP of molecular weights of 5×10^6 and 3.6×10^5 , respectively, were procured from Aldrich and employed without any further purification to prepare the polymer blend electrolytes. The molecular structures of both polymers are shown in Fig. 1. The salt Sodium metaperiodate (NaIO₄) and Titanium dioxide (TiO₂ nanopowder), both from Sigma Aldrich, were used as additives. The mean size of TiO₂ NPs was ca. 10 nm (given from manufacturer).

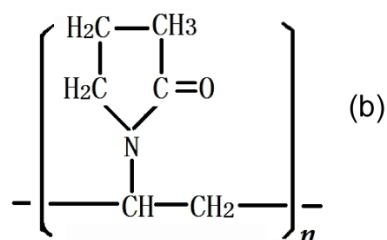
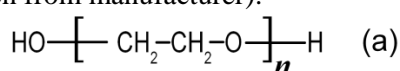


Fig. 1 Molecular structure of: (a) poly(ethylene oxide) (PEO); (b) polyvinyl pyrrolidone (PVP)

All substances were dissolved in methanol with high purity from Aldrich. First, PEO and PVP polymers were individually dissolved in methanol, then appropriate amounts of PEO and PVP solutions (w/w ratio 70% : 30% in present experiments) were mixed (Fig. 2a), followed by mechanical stirring at room temperature for 15

hours to obtain uniform mixture. In the meanwhile, 10 wt% of NaIO₄ salt was separately dissolved in methanol and this solution was added to the prepared viscous PEO/PVP polymer solution in order to be produced PEO/PVP/NaIO₄ polymer complex [22]. Separately, the powder of nano-sized TiO₂ was homogeneously dispersed in methanol. This solution was sonicated for 30 minutes and then added to PEO/PVP/NaIO₄ solution to prepare PEO/PVP/NaIO₄/TiO₂ - nanocomposite polymer blend solution with complexed salt ions and incorporated TiO₂ nanofillers (Fig. 2b). Technologically, this was done by drop-by-drop method. The concentration of the salt NaIO₄ in the PEO/PVP/NaIO₄/TiO₂ nano-composite blend solutions was kept at 10 wt%, whereas the TiO₂ NPs were included in the polymer blend at three concentrations: 1, 2 and 3 wt%.

Chemically-stable free-standing thin films (150 μm) of the synthesized PEO/PVP/NaIO₄/TiO₂ salt-complexed polymer blend material with excellent dimensional stability are formed by using solution casting of nanocomposite blend solution. The as-prepared viscous nanocomposite blend solutions were poured into polypropylene dishes and the solvent (methanol) was allowed to evaporate slowly at room temperature to obtain free-standing polymer electrolyte films of thickness of 150 μm. The final products of polymer blend electrolyte films were dried at 45°C under vacuum at 10⁻³ mbar pressure to remove traces of methanol solvent. Then the films were kept in desiccators filled with silica gel desiccants for several hours before being characterized, to avoid any traces of moisture.

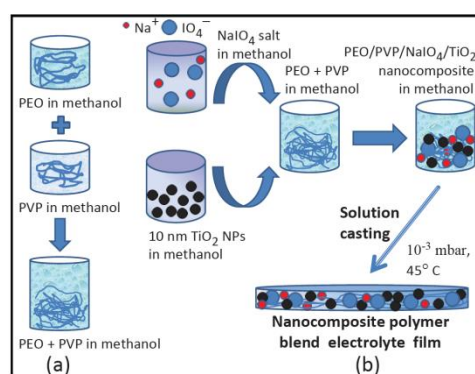


Fig. 2. A scheme showing the preparation of PEO/PVP/NaIO₄/TiO₂ solid-state nanocomposite polymer electrolytes.

Methods

For ionic conductivity measurements, the produced solid polymer electrolyte films were sandwiched between two copper electrodes with diameter 1 cm. The conductivity studies were

carried out at room temperature by EIS. Frequency spectra of complex electrical impedance were taken in the range 1 Hz – 1 MHz using potentiostat /galvanostat/ impedance-meter BioLogic SP-200. During these measurements, the voltage amplitude applied to the polymer electrolyte films was fixed at 0.5 V_{RMS}.

The ionic conductivity (σ) of the samples was calculated according to the relation

$$\sigma = t/(A \cdot R_B), \quad (1)$$

where t and A are the thickness of the sample and the area of the electrodes (i.e., the electrically-active area of the electrolyte film), respectively. R_B is the bulk resistance of the samples. This quantity is determined through impedance spectra.

Dielectric spectra of NCPEs PEO/PVP/NaIO₄/TiO₂ were obtained from the real (Z') and imaginary (Z'') parts of complex electrical impedance. In alternating-current electric field, the relative permittivity is a complex function and is defined by $\epsilon^* = \epsilon' - j \epsilon''$. Real (ϵ') and imaginary (ϵ'') parts of dielectric permittivity were calculated using the relations [24]:

$$\epsilon' = -\frac{Z''}{\omega C_0 (Z'^2 + Z''^2)} \quad (2)$$

and

$$\epsilon'' = \frac{Z'}{\omega C_0 (Z'^2 + Z''^2)}, \quad (3)$$

where C_0 is the vacuum capacitance ($C_0 = \epsilon_0 A/t$; $\epsilon_0 = 8.85 \times 10^{-12}$ F/m is the permittivity of free space). The angular frequency is given as $\omega = 2\pi f$, where f is the frequency of applied electric field.

RESULTS AND DISCUSSION

Fig. 3 shows the complex impedance plane diagrams, the Nyquist plots (Z' vs Z'') for the studied PEO/PVP/NaIO₄/TiO₂ NCPEs, as obtained from their frequency spectra of complex electrical impedance measured by EIS. For all our samples, the Nyquist plots demonstrate a well-defined semicircle at intermediate frequencies, which can be explained by parallel combination of bulk resistance and bulk capacitance [25].

The ionic conductivity (σ) of the PEO/PVP/NaIO₄/TiO₂ was calculated by Eq. (1). The bulk resistance R_B was obtained from the intercept of the semicircle with the real axis (Z'). The room-temperature σ estimated by this way for PEO/PVP/NaIO₄(10 wt%) electrolyte film was 1.57×10^{-7} S/cm [22]. As a result of the inclusion of 1 wt% of TiO₂ NPs, the value of σ of Na⁺-conducting NCPE becomes about three times higher than σ of the undoped PEO/PVP/NaIO₄ electrolyte (Fig. 4).

By increasing concentration of TiO₂ nanofillers, R_B is decreased (Fig. 3). Accordingly, at 2 wt% TiO₂ the increase in σ of TiO₂-doped PEO/PVP/NaIO₄ is about six times, and at 3 wt% TiO₂ – more than 12 times (Fig. 4).

The enhancement of conductivity as a result of inclusion of TiO₂ NPs is relevant to reduction in crystallinity of the polymer chains in blend polymer electrolyte. Certainly, this improves the sodium ion transport and hence improves the ionic conductivity of the polymer electrolyte [26,27].

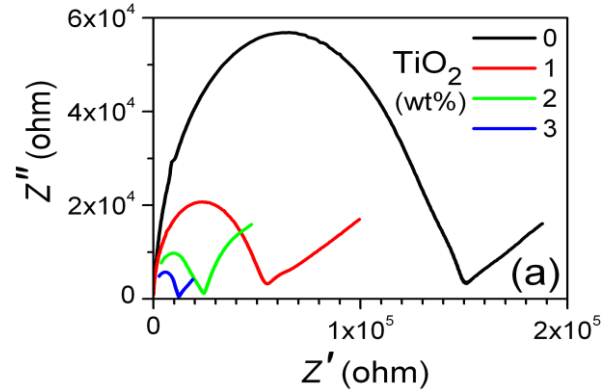


Fig. 3. Nyquist complex impedance plots for PEO/PVP/NaIO₄/TiO₂ NCPE system composed with TiO₂ NPs at concentrations 1, 2 and 3 wt%.

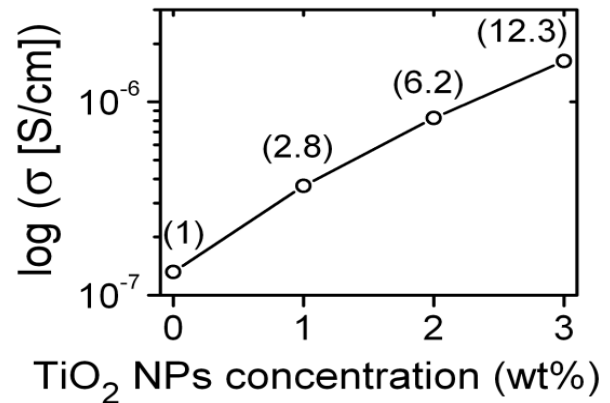


Fig. 4. Room-temperature ionic conductivity (σ) of the studied PEO/PVP/NaIO₄/TiO₂ NCPEs vs the concentration of TiO₂ NPs. The numbers in parentheses indicate the conductivity enhancement factors due to TiO₂ inclusion.

This effect occurs due to high interfacial interactions between the organic moieties of both polymers and TiO₂ NPs [1]. Such interactions of doping NPs with the polymer chains lead to improvement in the amorphicity and flexibility of the polymer matrix [28] that leads to a further increase in segmental motion of the polymer chains in the amorphous domain, which supports the mobility enhancement of the charge carriers in flexible solid-like amorphous-rich polymer electrolytes, thus increasing their ionic conductivity

[1,6,29,30]. Note that because the TiO₂ NPs are inert additives, they do not provide and conduct ions by themselves. Such inactive (passive) NPs do not participate in the ionic conduction process (are not involved in the Na⁺ transport process). But the size and the characteristics of the TiO₂ nanofillers predetermine in a large extent the electrochemical properties of the PEO/PVP/NaIO₄/TiO₂ NCPE system.

Besides the ionic conductivity, the dielectric properties of the considered NCPE are also of interest because they determine the ability of this dielectric material to store electrical energy. The real part of complex dielectric permittivity ϵ' has the same significance as that of the ordinary dielectric constant of the material. This physical quantity is directly related to the energy that can be stored in the material during each charging cycle and returned to the electric field at the end of the cycle. Fig. 5 presents the dielectric behavior (the frequency spectra of the real and imaginary parts of dielectric function) of the studied electrolyte systems, as calculated by Eqs. (2) and (3). As seen from Fig. 5, the TiO₂-doped PEO/PVP/NaIO₄ exhibits an enhanced dielectric response in comparison to undoped electrolyte PEO/PVP/NaIO₄. Moreover, the dielectric permittivity of PEO/PVP/NaIO₄/TiO₂ NCPE is increased by increasing concentration of the TiO₂ nanofillers. It should be noted that this trend does not hold at higher frequencies (> 1 kHz). The explanation of such effect requires to perform various complementary measurements and additional analyses that is out of scope of the present work, such as, for example, the calculation of ion mobility in these systems as the percentage concentration of TiO₂ varies.

The observed increase in ϵ (Fig. 5) can be explained by the capability of TiO₂ NPs to do a dissociation of undissociated salt/ion aggregates into free ions (anions) in the polymer matrix of the considered solid polymer electrolyte [31,32]. This feature is related to the conductivity processes and it evidences that the conduction in polymer electrolytes takes place through charge migration of ions between coordinated sites of the polymer along with the segmental relaxation of polymer [33].

CONCLUSIONS

By inclusion of TiO₂ NPs with a size of ~ 10 nm, the ion-conducting and dielectric properties of PEO/PVP blend solid polymer electrolytes complexed with NaIO₄ salt are considerably changed. As a result from high interfacial interactions between polymer chains and the surface of TiO₂ nanoparticles, the TiO₂ nanofillers

lead to increase of Na⁺-ion conductivity of PEO/PVP/NaIO₄/TiO₂ NCPE system, as compared to undoped electrolyte PEO/PVP/NaIO₄.

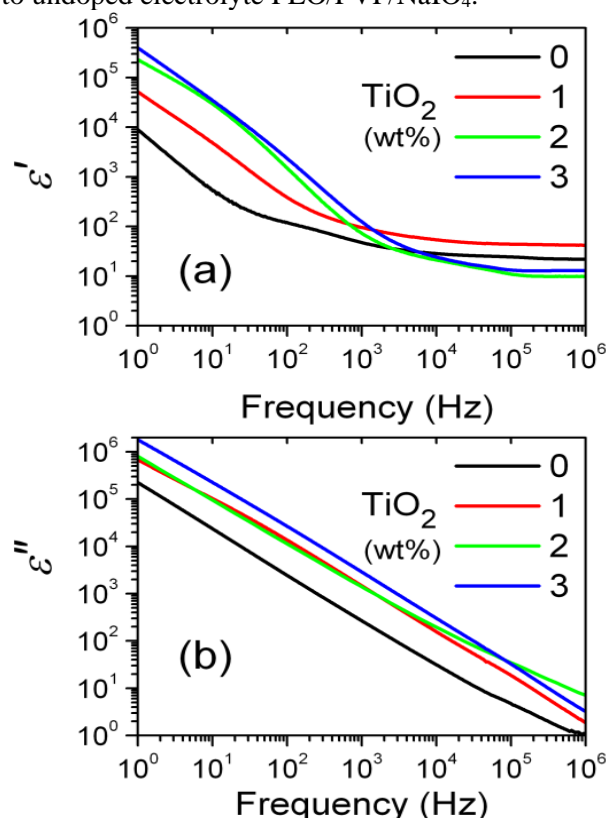


Fig. 5. (a) Frequency-dependent real (a) and imaginary (b) parts of dielectric function of PEO/PVP/NaIO₄/TiO₂ NCPEs containing 1, 2 or 3 wt% TiO₂ nanofillers. For the sake of comparison, data obtained for dielectric function of undoped PEO/PVP/NaIO₄ solid polymer electrolyte are also given.

It is demonstrated that the Na⁺-ion conductivity of PEO/PVP/NaIO₄/TiO₂ NCPEs is strongly (exponentially) enhanced with the addition of TiO₂ nanofillers when the concentration of these nanodopants is up to a level of 3 wt%. Further, in comparison to PEO/PVP/NaIO₄ electrolyte, the TiO₂-doped NCPE PEO/PVP/NaIO₄ considered here demonstrated enhanced dielectric permittivity due to increase of dissociated ions in the polymer blend matrix upon addition of TiO₂ nanofillers. Such modifications of electrical and dielectric properties characterize the PEO/PVP/NaIO₄/TiO₂ NCPE system as a promising ionic conductor, feasible to be applied in ionic devices including Na batteries, in electrochemical cells and in organic electronics. These results are encouraging to further investigate other interesting aspects regarding the electrical and dielectric properties of the produced NaIO₄ salt-complexed TiO₂-nanofilled ionic polymer electrolytes (work in progress).

Acknowledgements: Work supported by the European Regional Development Fund within OP

Y. Marinov et al.: Electrochemical impedance and dielectric spectroscopy study of TiO₂-nanofilled....
 “Science and Education for Smart Growth 2014-2020”, Project CoE “National Center of Mechatronics and Clean Technologies”, BG05M2OP001-1.001-0008-C01. This study was partially supported by the Bulgarian Ministry of Education and Science under the National Research Programme “Young scientists and postdoctoral students” approved by DCM # 577 / 17.08.2018

REFERENCES

1. S. A. Suthanthiraraj, M. Johnsi, *Ionics*, **23**, 1 (2016).
2. M. R. Johan, O. H. Shy, S. Ibrahim, S. M. M. Yassin, T. Y. Hui, *Solid State Ionics*, **196**, 41 (2011).
3. M. Yuan, J. Erdman, C. Tang, H. Ardebili, *RSC Adv.*, **4**, 59637 (2014).
4. J. H. Lee, C. H. Park, J. P. Jung, J. H. Kim, *J. Power Sources*, **298**, 14 (2015).
5. Y. Deng, C. Fang, G. Chen, *J. Power Sources*, **304**, 81 (2016).
6. H. K. Koduru, F. Scarpelli, Y. G. Marinov, G. B. Hadjichristov, P. M. Rafailov, I. K. Miloushev, A. G. Petrov, N. Godbert, L. Bruno, N. Scaramuzza, *Ionics*, **24** 3459 (2018).
7. M. S. Johnsi, S. A. Suthanthiraraj, *Macromolec. Research*, **26**, 100 (2018).
8. X. Zhang, X. Wang, S. Liu, Z. Tao, J. Chen, *Nano Research*, **11**, 6244(2018).
9. J. Sharma, S. Hashmi, *J. Polym. Compos.*, **40**, 1295 (2019).
10. H. K. Koduru, L. Bruno, Y. G. Marinov, G. B. Hadjichristov, N. Scaramuzza, *J. Solid State Electrochem.*, **23**, 2707 (2019).
11. F. Bertasi, K. Vezzu, G. A. Giffin, T. Nosach, P. Sidens, S. Greenbaumd, M. Vittadello, V. D. Noto, *Int. J. Hydrog. Energy*, **39**, 2884 (2014).
12. K. N. Kumar, K. Saijyothi, M. Kang, Y. C. Ratnakaram, K. H. Krishna, D. Jin, Y. M. Lee, *Appl. Phys. A*, **122**, art. 698 (2016).
13. J. M. Tarascon, M. Armand, *Nature*, **414**, 359 (2001).
14. S. K. Kim, D. G. Kim, A. Lee, H. S. John, J. J. Wie, N. A. Nguyen, M. E. Mackay, J. C. Lee, *Macromolecules*, **45**, 9347(2012).
15. A. M. Stephan, K. S. Nahm, *Polymer*, **47**, 5952 (2006).
16. S. Mohapatra, A. Thakur, R. N. P. Choudhary, *Ionics*, **14**, 255 (2008).
17. M. Patel, K. G. Chandrappa, A. J. Bhattacharyya, *Solid State Ionics*, **181**, 844 (2010).
18. K. Vignarooban, R. Kushagra, A. Elango, P. Badami, B. E. Mellander, X. Xu, T. G. Tucker, C. Nam, A. M. Kannan, *Int. J. Hydrogen Energy*, **41**, 2829 (2016).
19. K. K. Kumar, M. Ravi, Y. Pavani, S. Bhavani, V. V. R. N. Rao, *Physica B: Condens. Matter*, **406**, 1706 (2011).
20. K. K. Kumar, M. Ravi, Y. Pavani, S. Bhavani, V. V. R. N. Rao, *J. Non-Crystalline Solids*, **358**, 3205 (2012).
21. K. K. Kumar, M. Ravi, Y. Pavani, S. Bhavani, A. K. Sharma, V. V. R. N. Rao, *J. Membr. Sci.*, **454**, 200 (2014).
22. H. K. Koduru, L. Marino, F. Scarpelli, A. G. Petrov, Y. G. Marinov, G. B. Hadjichristov, M. T. Iliev, N. Scaramuzza, *Curr. Appl. Phys.*, **17**, 1518 (2017).
23. G. B. Hadjichristov, Tz. E. Ivanov, Y. G. Marinov, H. K. Koduru, N. Scaramuzza, *Physica Status Solidi (A): Appl. Mater. Sci.*, **216**, 1800739 (2019).
24. K. Deshmukh, S. Sankaran, B. Ahamed, K. K. Sadasivuni, K. S. K. Pasha, D. Ponnamma, P. S. R. Sreekanth, K. Chidambaram, in: Spectroscopic Methods for Nanomaterials Characterization, S. Thomas, R. Thomas, A. K. Zachariah, R. K. Mishra (eds), vol. 2, Elsevier, Amsterdam, 2017, p. 248.
25. E. Barsoukov, J. R. Macdonald (eds), Impedance Spectroscopy: Theory, Experiment, and Applications, Wiley Intescience, Hoboken, New Jersey, 2005.
26. D. Carlier, J. H. Cheng, R. Berthelot, M. Guignard, M. Yoncheva, R. Stoyanova, B. J. Hwang, C. Delmas, *Dalton Transactions*, **40**, 9306 (2011).
27. Y. C. Lin, J. H. Cheng, M. Venkateswarlu, F. M. Wang, R. Santhanam, B. J. Hwang, *J. Chin. Chem. Soc.*, **59**, 1250 (2012).
28. C. W. Lin, C. L. Hung, M. Venkateswarlu, B. J. Hwang, *J. Power Sources*, **146**, 397 (2005).
29. H. K. Koduru, M. T. Iliev, K. Kondamareddy, D. Karashanova, T. Vlachov, X. Z. Zhao, and N. Scaramuzza, *J. Phys. Conf. Ser.*, **764**, 012006 (2016).
30. H. K. Koduru, K. K. Kondamareddy, M. T. Iliev, Y. G. Marinov, G. B. Hadjichristov, D. Karashanova, N. Scaramuzza, *J. Phys. Conf. Ser.*, **780**, 012006 (2017).
31. D. Kumar, S. A. Hashmi, *Solid State Ionics*, **181**, 416 (2010).
32. A. Bhide, K Hariharan, *Polym. Int.*, **57**, 523 (2008).
33. M. A. L. Nobre, S. Langfredi, *J. Phys. Chem. Solids*, **62**, 1999 (2001).

Electrochemical deposition of Sb₂Se₃ thin films semiconductor from tartaric acid solution

V. A. Majidzade*, A. Sh. Aliyev, D. B. Tagiyev

Institute of Catalysis and Inorganic Chemistry named after acad.M.Nagiyev, Azerbaijan National Academy of Sciences, H.Javid ave., 113, AZ 1143, Baku, Azerbaijan

Received November 16, 2019; Accepted January 27, 2020

The proffered work has been dedicated to the electrochemical deposition of Sb-Se layers from tartaric acid as an electrolyte. In the course of research, the cyclic voltammetric polarization curves have been diagrammed by the potentiodynamic method. Sb-Se films have been deposited on different metals by potentiostatic and galvanostatic methods. The analysis of polarization curves and X-ray analysis of obtained samples indicate that Sb₂Se₃ was formed as a result of our research.

Keywords: Antimony-selenide, electrodeposition, polarization, tartaric acid, semiconductive layers

INTRODUCTION

Binary chalcogenide semiconductors have attracted considerable attention in the past few years owing to their applications in photoelectrochemical devices, optoelectronic devices, switching devices, thermoelectric coolers, decorative coatings etc [1-12]. The aim of the production of these thin layers is to enhance stability and effectiveness of solar batteries [13].

Antimony Triselenide (Sb₂Se₃) is a member of the V-VI semiconductor family [14-23]. It is a staggered layered compound, direct band gap semiconductor with orthorhombic crystal structure [24]. Sb₂Se₃ is also a promising light absorber material [25-27]. Excellent optoelectronic properties such as high absorption coefficient (>105 cm⁻¹), low band gap (ranging from 1.1-1.3 eV) suitable for visible light harvesting and p-type conductivity makes it an ideal candidate for solar cell applications. In addition to it, low material cost, abundant supply and relatively low toxicity constituents are some of the added advantages suitable for photovoltaics [28-30].

Currently, photoelectrochemical splitting of water is an attractive and sustainable way to generate hydrogen, which can be used to maintain fuel economy [31-33], and photoelectrodes in PEC elements play a crucial role in the solar-hydrogen process (STH) conversion efficiency [34].

Sb₂Se₃ has received a lot of attention in this area - for thermoelectric, photovoltaic and energy storage [35-36] applications owing to its earth abundance, non-toxicity in comparison toxicity to elemental selenium, single phase (indicating the

phase and defects of Sb₂Se₃ can be easy to control), favorable band gap value (1.1~ 1.2 eV) [37-39].

Sb₂Se₃ semiconductive layers are obtained using various methods: vacuum thermal evaporation [40], rapid thermal evaporation [41], chemical bath deposition [42, 43], spin coating [44], electrodeposition [45], arrested precipitation technique [46], pulsed laser deposition [47], photoelectrochemical deposition [48] and etc.

Some researchers [17, 18] got thin layers of Sb₂Se₃ with 200-720 nm in thickness using thermal evaporation via deposition on the glass substrate. The effect of the thickness of these amorphous layers to their structure, morphology and optical properties has been studied. The optical adsorption of Sb₂Se₃ layers is related to indirect adsorption gap, whereas the change of width of the forbidden band is explained by the existence of structural defects and irregularity in the chalcogenide systems. The result of optical adsorption indicated that the regularity of layer structures increases with their thickness. Authors second essential goal was a search of the mechanism of transforming of thin-layered Sb₂Se₃ into the memory cell.

Thin-layered Sb₂Se₃ has been obtained with via electrodeposition on the stainless steel and glass electrodes in the nonaqueous medium [19]. The layers of higher quality can be obtained from 0.05M of electrolyte prepared from SbCl₃ and SeO₂ components taken in 1:1 ratio. According to the result of SEM analysis, the semiconductive Sb₂Se₃ layers cover the electrode surface totally and the width of the forbidden band (energy gap) is 1.195 eV. Some researchers have attempted to synthesize

* To whom all correspondence should be sent.
E-mail: vuska_80@mail.ru

antimony-selenide of different shapes. They proved that there were homopolar (Se-Se) and heteropolar (Sb-Se) bonds in the obtained nanolayered [20], nanospheric [21] and nanowire layers by mean of Raman Spectroscopy.

Some investigations showed that [22] the deposited films of Sb_2Se_3 with different thicknesses at a rate of 30 Å s, and at room temperature were found to have an amorphous structure. The electric resistance of these layers on the silver electrodes increases with the increase of the thickness of the layer up to 370.8 nm, gets the maximal point, but after this point, it decreases. The specific resistance for every thickness decreases with increasing of temperature. Thin layers of Sb_2Se_3 were deposited using electrochemical atomic layer epitaxy (ALE) [23]. From analyzing literature related to the matter under investigation it is shown that the most effective method to deposit Sb and Se simultaneously is electrochemical. There are rare data about the electrochemical synthesis of Sb-Se, So it needs more information and experiments to clear the view. Thus, throughout the work, the thin-layered semiconductive Sb-Se has been obtained by the electrochemical method.

EXPERIMENTAL

The codeposition of antimony and selenium by the electrochemical way has been achieved as follows: tartaric acid was dissolved in distilled water to prepare under-investigated electrolyte solution, then $SbOCl$ salt and selenite acid (H_2SeO_3) was dissolved in tartaric acid solution, separately. The compositions of the obtained electrolytes consist of 0.05 mol/L $SbOCl$ + 0.007 mol/L $C_4H_6O_6$ (tartaric acid) and 0.05 mol/L H_2SeO_3 + 0.007 mol/L $C_4H_6O_6$. The polarization curves have been recorded using IVIUMSTAT Electrochemical Interface Potentiostat. A three-electrode electrochemical cell was used. The working electrodes here were Pt 2 mm² surface area and Ni with 2 cm² surface area. Silver electrode ($Ag/AgCl$) was used as a comparative (reference) electrode. Pt sheet of 4 cm² surface area was used as an auxiliary electrode. Throughout the electrolysis process, the temperature of the electrolyte solution was regulated by UTU – 4 universal ultra-thermostat. The phase composition of the obtained thin layers was studied with “D2 Phaser” XRay Phase Analyzer of “Bruker” company (CuK_{α} ; Ni filter). The morphology and chemical element composition of samples were analyzed by scanning electron microscopy (SEM) “Carel Zeiss Sigma”. The adhesion of thin films to the surface of the electrode is determined by the

method of lattice cuts [49] and bending of the electrode at an angle of 90°.

on prepared samples using a ruler At least 5 parallel and 5 perpendicular cuts at a distance of 1 or 2 mm from each other are made. In this case, a lattice of squares of the same size is formed on the surface. After applying the grating, the coating surface is cleaned with a brush from exfoliated pieces of film and adhesion is evaluated on a four-point scale: 1 point - the edges of the incisions are smooth, there are no exfoliated pieces of coating; 2 points - peeling of the coating with 5% of the surface of the lattice;

3 points - peeling of the coating from 35% of the surface of the grating; 4 points - peeling of the coating with more than 35% of the surface of the grating;

Before starting experiment required Pt is chemically polished in concentrated sulfuric acid and hydrogen peroxide solution, and then washed with distilled water. The Ni electrodes, at first, polished electrochemically in concentrated HNO_3 acid, then refurbished in a solution consists of H_2SO_4 , H_3PO_4 and citric acids ($T = 293-303K$, $i = 50 A/dm^2$, $\tau = 180 sec.$). Finally, Ni electrodes are washed with distilled water.

RESULTS AND DISCUSSION

It is known that for codeposition of any two components by the electrochemical method, at first, kinetics and mechanism of deposition of these components from the taken electrolyte and various patterns should be studied separately. The deposition process of both antimony [50, 51] and selenium [52] from tartaric acid has been investigated by our team. The electrochemical cathodic reduction processes of both components were studied; the optimal conditions were defined and investigated of the codeposition process. The kinetics and mechanisms of the electrochemical deposition of antimony and selenium from tartaric acid have been investigated separately. The cyclic voltammetric polarizations of the codeposition process of Sb and Se on Pt electrode were achieved by the potentiodynamic method, as given in Fig. 1. It seems from this figure, that codeposition process of Sb and Se layers is mono-stage and occurs within the potential range of -0.42 – (-0.7) V. The transforming processes of SeO_3^{2-} ions into Se^0 , then of electroreduced into Se^{2-} ions occurred at a potential starting from -0.42 V to 0.55 V [52]. After that, the obtained adsorbed Se^{2-} ions on the electrode surface joined with Sb^{3+} ions in solution forming Sb-Se thin films. As a result, it can be noticed that the surface of the electrode is covered with a black layer. After a potential of -0.7 V the

hydrogen gas is released, therefore simultaneous process has been studied up to this point of potential.

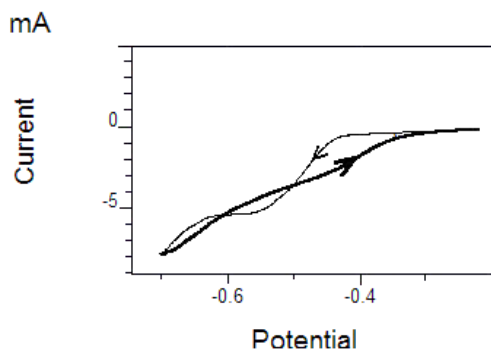


Fig.1. The cyclic polarization curve of the co-deposition process of Sb-Se layers on the Pt electrode immersed in an electrolyte consists of: 0.05 (mol/L) $SbOCl$ + 0.05 (mol/L) H_2SeO_3 + 0.007 (mol/L) $C_4H_6O_6$, at $T = 298$ K, and $E_V = 0.03$ V/s.

The result of X-Ray Phase Analysis of the electrodeposited Sb-Se layers on Pt electrode shows that through the co-electrodeposition process, the Sb_2Se_3 is obtained at these conditions. It is observed that the electrodeposited thin layers of Sb_2Se_3 are black in color, and there is a strong adhesion (2 point) between the substrate surface and the obtained compound. Depending on the condition of the electrochemical process, the composition and quality of the obtained thin layers are varied dissimilarly (Table 1).

As seen from Table 1, the quantity of components in deposited layers increases statutorily with increasing their concentration that included in an electrolyte's contents. Also, it is observed that the color of layers is changed from golden-red to dark black.

Table 1. The composition and quality of the obtained Sb-Se thin layers depending on the condition of the electrochemical process

| № | The composition of solution, (mol/L) | | The composition of the layer, mass % | | Thermal processing, T, K | The appearance of the layer |
|----|--------------------------------------|------------|--------------------------------------|-------|--------------------------|------------------------------------|
| | $SbOCl$ | H_2SeO_3 | Sb | Se | | |
| 1. | 0.01 | 0.09 | 15.2 | 84.8 | 673 | Golden-red, rough, amorphous |
| 2. | 0.05 | 0.05 | 62.26 | 37.74 | 723 | Black-red, smooth, crystalline |
| 3. | 0.09 | 0.01 | 82.6 | 17.4 | 703 | Dark black, crystalline, smooth |
| 4. | 0.01 | 0.09 | 23.7 | 76.3 | 293 | Golden-red, smooth, amorphous |
| 5. | 0.05 | 0.05 | 48.27 | 51.73 | 293 | Black-red, low crystalline, smooth |
| 6. | 0.09 | 0.01 | 70.7 | 29.3 | 293 | Dark black, crystalline, rough |

On the other hand, it can be noticed from Table 1 that the quantity of Sb is more in layers that are exposed to thermal processing under argon atmosphere. It looks like thermal evaporation of Se after 673K temperature. The effect of different factors (temperature, the concentration of components, the rate of potential and etc.) to co-electrodeposition process of the semiconductive Sb_2Se_3 compound have been clarified [53].

The essential effective factor – the temperature has been studied. The cyclic voltammetric polarization curves via the potentiodynamic method on the Ni electrode were given in figure 2. The experiments were carried out within the range of 298-358 K. As is seen from the curves of Fig. 2, it can be observed that with an increase in the temperature, the deposition process accelerates. The temperature increment stimulates obtaining of crystalline layers. But this process continues up to about 338-343 K temperature interval. Upwards of 343 K temperatures the quality, adhesion, smoothness, composition, and crystallinity of obtaining layers decrease.

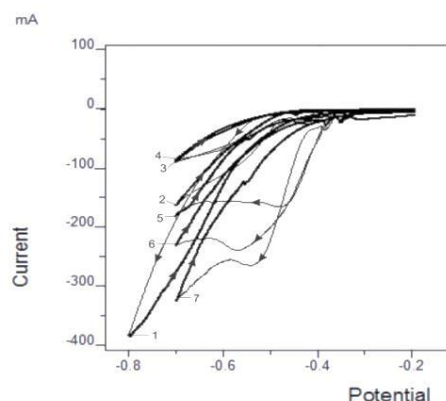


Fig. 2. The effect of temperature to co-deposition process of Sb-Se layers on the Pt electrode. Electrolyte composition (mol/L): 0.05 $SbOCl$ + 0.05 H_2SeO_3 + 0.007 $C_4H_6O_6$. 1- 298K, 2- 308K, 3- 318K, 4- 328K, 5- 338K, 6- 348K, 7- 358K. $E_V = 0.03$ V/s.

The effect of the other main factor – concentration to the co-deposition process has been studied by both potentiodynamic and galvanostatic methods. Some of the outcomes were given in Table 1. Results show that stoichiometric semiconductive layers are attained from 0.05 mol/L concentration of both components.

Table 2. The effect of temperature to co-deposition process of Sb-Se by electrochemical method according to the result of SEM analysis. Electrolyte (mol/L): 0.05 $SbOCl$ + 0.05 H_2SeO_3 + 0.007 $C_4H_6O_6$, $E_V = 0.03$ V/s.

| № | T, K | The composition of the layer, % | | The appearance of the layer |
|----|------|---------------------------------|-------|---|
| | | Sb | Se | |
| 1. | 308 | 27.25 | 72.75 | Golden-red, amorphous, rough |
| 2. | 318 | 15.63 | 84.37 | Reddish-black, small crystalline, rough |
| 3. | 328 | 18.57 | 81.43 | Black, crystalline, smooth |
| 4. | 338 | 26.07 | 73.93 | Dark-black, crystalline, smooth |
| 5. | 348 | 12.93 | 87.07 | Dark-black, small crystalline, rough |

Therefore, this concentration is optimal to get Sb_2Se_3 . As seen from Fig. 3, the cyclic polarization curves of components within 0.025 - 0.09 mol/L concentration interval were given. It is observed from polarization curves that with increasing of concentration of $SbOCl$ in the electrolyte, the co-deposition potential is displaced from - 0.72 V to - 0.38 V. It means that the co-deposition process is displaced to the more positive region with increasing of concentration.

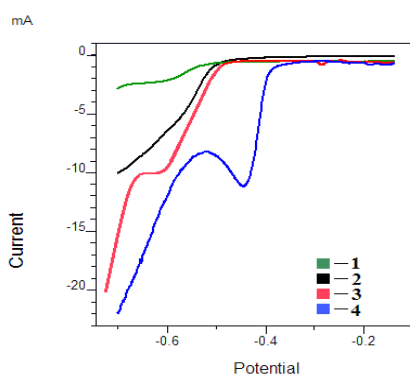


Fig. 3. The effect of the concentration of the components on the co-deposition process of Sb-Se via potentiodynamic method on the Pt electrode. Electrolyte composition (mol/L): 1- 0.025 $SbOCl$ + 0.075 H_2SeO_3 + 0.007 $C_4H_6O_6$; 2- 0.05 $SbOCl$ + 0.05 H_2SeO_3 + 0.007 $C_4H_6O_6$; 3- 0.075 $SbOCl$ + 0.025 H_2SeO_3 + 0.007 $C_4H_6O_6$; 4- 0.09 $SbOCl$ + 0.01 H_2SeO_3 + 0.007 $C_4H_6O_6$, at $E_V = 0.03$ V/s, and $T = 298$ K.

The effect of the scan rate of potential to the co-deposition process has been also studied within 0.005-0.2 V/s interval (Fig. 4).

The experiment was carried out by potentiodynamic method via recording the cathodic polarization curves. From polarization curves, it is obvious that the increase in the scan rate of potential enables the co-deposition process to occur in the more cathodic potential region. It is important supremacy of the electrochemical process.

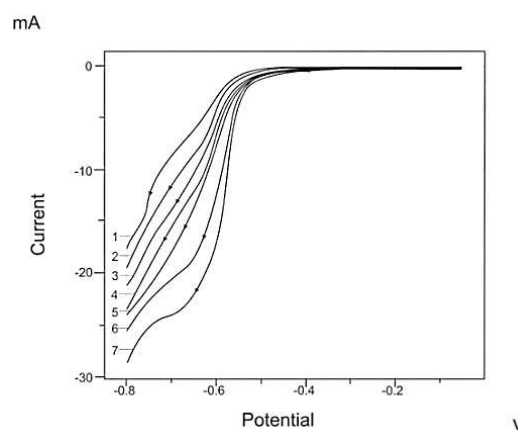


Fig. 4. The effect of the scan rate variation to the co-deposition process of Sb-Se via potentiodynamic method on the Pt electrode. Electrolyte composition (mol/L): 0.05 $SbOCl$ + 0.05 H_2SeO_3 + 0.007 $C_4H_6O_6$; E_V (V/s): 1- 0.005; 2- 0.01; 3- 0.03; 4- 0.05; 5- 0.08; 6- 0.12; 7- 0.2. $T = 298$ K.

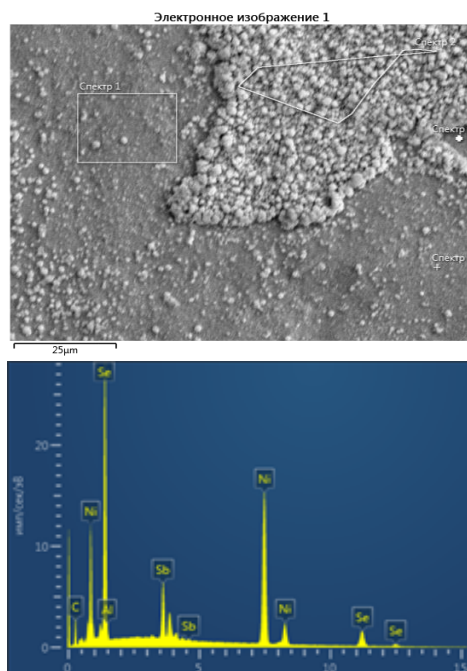


Fig. 5. SEM and EDX of the electrodeposited thin-layered Sb-Se on the Ni electrode. At the electrolyte composition of 0.05 mol/L $SbOCl$ + 0.05 mol/L H_2SeO_3 + 0.007 mol/L $C_4H_6O_6$ at $T = 338$ K.

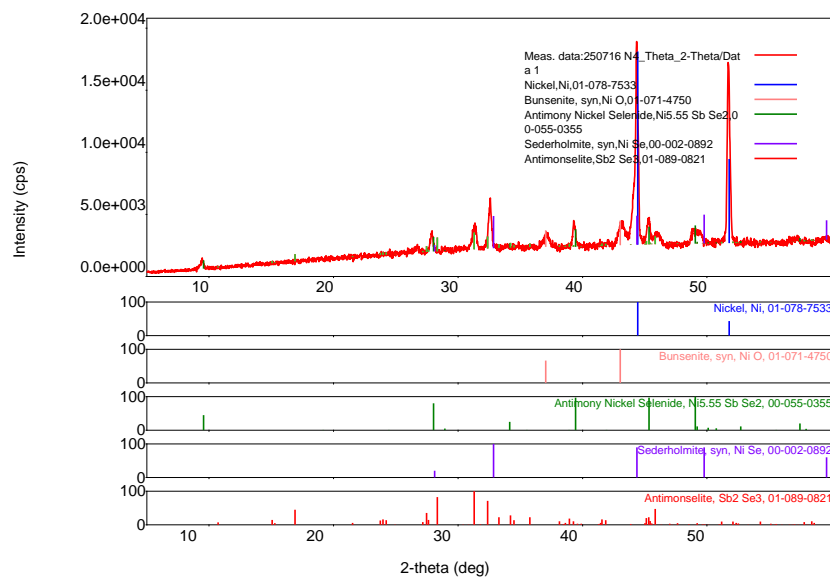


Fig. 6. X-Ray Phase Analysis of Sb-Se thin layers of the co-electrodeposited from electrolyte 0.05 mol/L $SbOCl$ + 0.05 mol/L H_2SeO_3 + 0.007 mol/L $C_4H_6O_6$ on the Ni electrode, at $T= 298K$.

As a result of the accomplished investigation, the composition of electrolyte and electrolytic condition for obtaining of thin layers of the Sb_2Se_3 compound by electrochemical method were detected as follow: at the electrolyte composition of 0.05 mol/L $SbOCl$ + 0.05 mol/L H_2SeO_3 + 0.007 mol/L $C_4H_6O_6$, $E_V = 0.03$ V/s, and $T= 298K$. The X-Ray Phase and SEM analysis of the obtained Sb_2Se_3 compound on Ni electrode confirmed that it is close to stoichiometric composition. The outcomes of this analysis were given in Figures 5 and 6.

CONCLUSIONS

The electrochemical deposition process of semiconductive Sb-Se thin layers has been investigated by both galvanostatic and potentiodynamic methods. The effects of the different factors on the co-deposition process of Sb-Se thin layers have been studied. The composition of electrolyte and electrolytic condition for depositing of these layers were typically determined according to outcomes. The results of X-ray Phase and SEM analysis indicate that the electrodeposited compound with stoichiometric composition (Sb_2Se_3) can be via the co-deposition process at our optimal conditions.

REFERENCES

1. N.S. Shinde, V.B. Prabhune, H.D. Dhaigude, C.D. Lokhande, V.J. Fulari, *Appl. Surf. Sci.*, **255**, 8688 (2009).
2. A.P. Torane, C.H. Bhosale, *Mater. Res. Bull.*, **38**, 847 (2003).

3. A.D.A. Buba, E.O. Ajala, D.O. Samson, *Asian Journal of Science and Technology*, **6**, 1146 (2015).
4. A.Sh. Aliyev, Sh.O. Eminov, T.Sh. Sultanova, V.A. Mejidzadeh, D.A. Kuliyeu, D. Jalilova, D.B. Tagiyev, *Chemical Problems*, **2**, 139 (2016)
5. M. Luo, M. Leng, X. Liu, J. Chen, C. Chen, S. Qin, J. Tang, *Appl. Phys. Lett.*, **104**, 173904 (2014).
6. O. Rachel, M.N. Jessy, R.P. Usha, *J. Ovonic Res.* **6**, 259 (2010).
7. R.G. Sotelo Marquina, T.G. Sanchez, N.R. Mathews, X. Mathew, *Mater. Res. Bull.*, **90**, 285 (2017).
8. A.Sh. Aliyev, V.A. Majidzade, N.Sh. Soltanova, D.B. Tagiyev, V.N. Fateev, *Chemical Problems*, **2**, 178 (2018).
9. Y.H. Yeo, T.S. Oh, *Mater. Res. Bull.*, **58**, 54 (2014).
10. R. Vadapoo, S. Krishnan, H. Yilmaz, C. Marin, *Phys. Status Solidi B.*, **248**, 700 (2011).
11. G.M. Huseynov, N.A. Mammadova, H.A. Imanov, *Chemical Problems*, **3**, 329 (2017).
12. A.Sh. Aliyev, M. Elrouby, S.F. Cafarova, *Mat. Sci. Semicon. Proc.*, **32**, 31 (2015).
13. T.T. Ngo, S. Chavhan, I. Kosta, O. Miquel, H.I. Grande, R. Tena-Zaera, *Acs. Appl. Mater. Inter.*, **6**, 2843 (2014).
14. A. Shongalova, M.R. Correia, B. Vermang, J.M.V. Cunha, P.M.P. Salomé, P.A. Fernandes, *MRS Commun.*, **1** (2018).
15. K.W. Sun, C.-H. Yang, T.-Y. Ko, H.-W. Liu, *Pure Appl. Chem.*, **81**, 1511 (2009).
16. S.-S. Zhang, J.-M. Song, H.-L. Niu, C.-J. Mao, S.-Y. Zhang, Y.-H. Shen. *J. Alloy Compd.*, **585**, 40 (2014).
17. M. Malligavathy, R.T. Ananth Kumar, Das Chandasree, S. Asokan, D. Pathinettam Padiyan, *J. Non-Cryst. Solids*, **429**, 93 (2015).

18. X. Liu, J. Chen, M. Luo, M. Leng, Z. Xia, Y. Zhou, S. Qin, D.-J. Xue, L. Lv, H. Huang, D. Niu, J. Tang, *ACS Appl. Mater. Interface*, **6**, 10687 (2014).
19. A.P. Torane, C.H. Bhosale, *J. Phys. Chem. Solids.*, **63**, 1849 (2002).
20. Y. Lai, Z. Chen, C. Han, L. Jiang, F. Liu, J. Li, Y. Liu, *Appl. Surf. Sci.*, **261**, 510 (2012).
21. Y. Zhang, G. Li, B. Zhang, L. Zhang, *Mater. Lett.*, **58**, 2279 (2004).
22. F. Abd El-Salam, M.A. Afify, E. Abd El-Wahab, *Vacuum*, **44**, 1009 (1993).
23. Y. Chen, L. Wang, A. Pradel, A. Merlen, M. Ribes. M.-C. Record, *J. Solid State Electrochem.*, **19**, 2399 (2015).
24. X. Shi, X. zhang, Y. Tian, C. Shen, C. Wang, H.-J. Gao, *Appl. Surf. Sci.*, **258**, 2169 (2012).
25. Y.C. Choi, Y.H. Lee, S.H. Im, J.H. Noh, T.N. Mandal, W.S. Yang, S.I. Seok, *Adv. Energy Mater.*, **4**, 1301680 (2014).
26. Y.C. Choi, T.N. Mandal, W.S. Yang, Y.H. Lee, S.H. Im, J.H. Noh, S.I. Seok, *Angew. Chem. Int. Ed. Engl.*, **53**, 1329 (2014).
27. Z. Kai, X. Ding-Jiang, T. Jiang, *Semicond. Sci. Technol.*, **31**, 063001 (2016).
28. X. Liu, C. Chen, L. Wang, J. Zhong, M. Luo, J. Chen, D.-J. Xue, D. Li, Y. Zhou, J. Tang, *Prog. Photovoltaics: Research and Applications*, **23**, 1828 (2015).
29. Y. Zhou, L. Wang, S. Chen, S. Qin, X. Liu, J. Chen, D.-J. Xue, M. Luo, Y. Cao, Y. Cheng, E.H. Sargent, J. Tang, *Nat. Photon.*, **9**, 409 (2015).
30. M. Leng, M. Luo, C. Chen, S. Qin, J. Chen, J. Zhong, J. Tang, *Appl. Phys. Lett.*, **105**, 083905 (2014).
31. D. Kim, K.K. Sakimoto, D. Hong, P. Yang, *Angew. Chem.*, **54**, 3259 (2015).
32. A.Sh. Aliyev, R.G. Guseynova, U.M. Gurbanova, D.M. Babanly, V.N. Fateev, I.V. Pushkareva, D.B. Tagiyev, *Chemical Problems*, **16**, 283 (2018).
33. L.J. Minggu, R.W.D. Wan, M.B. Kassim, *Inter. J. Hydrog. Energy*, **35**, 5233 (2010).
34. Y. Yang, S. Niu, D. Han, T. Liu, G. Wang, Y. Li, *Adv. Energy Mater.*, **7**, 1700555 (2017).
35. T.L. Kulova, I.I. Nikolaev, V.N. Fateev, A.Sh. Aliyev, *Chemical Problems*, **16**, 9 (2018).
36. V.N. Fateev, O.K. Alexeeva, S.V. Korobtsev, E.A. Seregina, T.V. Fateeva, A.S. Grigorev, A.Sh. Aliyev, *Chemical Problems*, **16**, 453 (2018).
37. X. Liu, C. Jie, L. Miao, M. Leng, X. Zhe, Z. Ying, S. Qin, D.J. Xue, L. Lu, H. Han, *Acs Appl. Mater. Interfaces*, **6**, 10687 (2014).
38. R. Venkatasubramanian, E. Silvola, T. Colpitts, B. O'Quinn, *Nature*, **413**, 597 (2001).
39. X. Ou, C. Yang, X. Xiong, F. Zheng, Q. Pan, C. Jin, M. Liu, K. Huang, *Adv. Funct. Mater.*, **27**, 1606242 (2017).
40. L. Zhiqiang, Z. Hongbing, G. Yuting, N. Xiaona, C. Xu, Z. Chong, Z. Wen, L. Xiaoyang, Z. Dong, C. Jingwei, M. Yaohua, *Appl. Phys. Express.*, **9**, 052302 (2016).
41. Y. Li, Y. Zhou, J. Luo, W. Chen, B. Yang, X. Wen, S. Lu, C. Chen, K. Zeng, H. Song, J. Tang, *RSC Adv.*, **6**, 87288 (2016).
42. S. Messina, M.T.S. Nair, P.K. Nair, *J. Electrochem. Soc.*, **156**, H327 (2009).
43. Y. Rodriques-Lazcano, Y. Peña, M.T.S. Nair, P.K. Nair, *Thin Solid Films*, **493**, 77 (2005).
44. B. Yang, D.-J. Xue, M. Leng, J. Zhong, L. Wang, H. Song, Y. Zhou, J. Tang, *Sci. Rep.*, **5**, 10978 (2015).
45. A.M. Fernández, M.G. Merino, *Thin Solid Films*, **66**, 202 (2000).
46. X. Wang, K.F. Cai, F. Shang, S. Chen, *J. Nanopart. Res.*, **15**, 1541 (2013).
47. L. Yu, J. Chen, Z.-W. Fu, *Electrochim. Acta*, **55**, 1258 (2010).
48. J. Yang, Y. Lai, Y. Fan, Y. Jiang, D. Tang, L. Jiang, F. Liu, J. Li, *RSC Adv.*, **5**, 85592 (2015).
49. P.M. Vyacheslavov, N.M. Shmeleva, Test methods for electrolytic coatings. L.: Engineering, 1977.
50. V.A. Majidzade, P.H. Guliyev, A.Sh. Aliyev, M. Elrouby, D.B. Tagiyev, *J. Mol. Struct.*, **1136**, 7 (2017).
51. A.Sh. Aliyev, M. Elrouby, Z.H. Hasanli, R.H. Huseynova, M.T. Abbasov, *Chemical Problems*, **1**, 62 (2015).
52. V.A. Majidzade, A.Sh. Aliyev, P.H. Guliyev, Y.N. Babayev, M. Elrouby, D.B. Tagiyev, *J. Electrochem. Sci., Eng.*, **8**, 197 (2018).
53. V.A. Majidzade. *Chemical Problems*, **3**, 331 (2018).

NiCo₂O₄/Ag as catalyst for bi-functional oxygen electrode

D. Nicheva^{1,2}, B. Abrashev¹, I. Piroeva³, V. Boev¹, T. Petkova¹, P. Petkov², K. Petrov¹

¹*Institute of Electrochemistry and Energy Systems Acad.E.Budevski, Bulgarian Academy of Sciences, Bl.10 Acad. G. Bonchev Str., 1113 Sofia, Bulgaria*

²*University of Chemical Technology and Metallurgy, 8, St. Kliment Okhridski Blvd., 1756 Sofia, Bulgaria*

³*Institute of Physical Chemistry, Bulgarian Academy of Sciences, Bl. 11 Acad. G. Bonchev Str.,1113 Sofia, Bulgaria*

Received January 16, 2020; Accepted February 03, 2020

NiCo₂O₄ has been synthesized using precipitation reaction. The obtained material studied by X-ray diffraction and scanning electron microscopy exhibits spinel structure. The electrochemical performance of the electrodes prepared from NiCo₂O₄ and NiCo₂O₄/Ag has been investigated by cyclic voltammetry, steady-state measurements and charge/discharge tests. The results demonstrate good electrochemical activity of the catalysts both in oxygen evolution and oxygen reduction reaction - the NiCo₂O₄/Ag electrode is stable more than 400 charge/discharge cycles.

Keywords: nickel-cobaltite, precipitation reaction, bi-functional oxygen electrode

INTRODUCTION

Innovative rechargeable batteries that can effectively store renewable energy are subject of increasing development. Among various metal/air batteries, the zinc/air battery is a system proven to have the required capacity for numerous applications. The rechargeable Zn-air batteries have focused the efforts of the researchers not only due to considerably high energy density but also due to cost efficiency. The theoretical calculated specific energy density of Zn-air batteries is 1084 Wh.kg⁻¹. [1-3].

The main challenge in the Zn/Air batteries progress is associated with the problems of zinc anode: dissolution into the alkaline solution [4], corrosion and the dendrite formation [5]. In rechargeable metal-air batteries, the oxygen evolution reaction (OER) and oxygen reduction reaction (ORR) both occur on the same electrode (usually the positive electrode) during the charge and discharge processes, respectively. The barriers for the bi-functional oxygen electrodes (BOE) are connected with: (i) the irreversibility of the oxidation reaction; (ii) corrosion during OER and (iii) the need of catalysts for both reactions – OER and ORR.

The efforts to develop oxygen electrode catalysts that operate both in cathodic and anodic modes are met by the irreversibility of both oxygen and evolution reactions in aqueous media at moderate temperatures (<150 °C) and composition limitations. The material used for a bi-functional oxygen electrode should be good catalysts for both the oxidation and reduction reactions of oxygen and

should be chemically stable over the wide range of potentials experienced during charge and discharge. Several attempts to construct bi-functional oxygen electrode (BOE) using metallic catalysts in a multi-layered design have been made but no commercially available material have appeared yet. The need of more efficient and corrosion resistant catalyst materials still exists and various metal oxides have been investigated as bi-functional catalysts for oxygen electrodes last years [6-11].

It is important to develop efficient bifunctional catalysts for both ORR during discharge and OER during charge. For ORR in alkaline electrolytes, Ag is known to be very active. Its activity can be increased by modification with other metals as NiCo₂O₄. The spinel nickel cobaltite (NiCo₂O₄) catalyst has focused much attention due to their cost-efficiency and availability but also due to the better electrical conductivity and electrochemical activity in comparison to other binary transition metal oxides [12, 13].

This paper describes our results in preparation of a non-precious metal hybrid as bi-functional catalysts for ORR and OER by mixing a catalyst which has superior activity for ORR (Ag) with one which is highly active and stable for OER (NiCo₂O₄) as.

EXPERIMENTAL

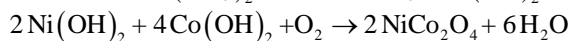
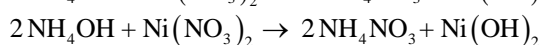
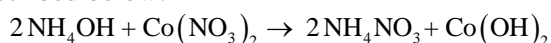
1. Synthesis

NiCo₂O₄ was synthesised by precipitation technique: solutions of Co(NO₃)₂.6H₂O and Ni(NO₃)₂.6H₂O were mixed with NH₄OH in appropriate amounts at room temperature. The resultant precipitate, after filtration, was washed

* To whom all correspondence should be sent.

E-mail: d.vladimirova@iees.bas.bg

with distilled water and dried for 2 hours. The obtained product was slowly heated with a rate of 1°C/min in air up to 350 °C for 4 hours. The reactions occurring during the synthesis are described below:



Silver powder was prepared by reduction method using the procedure reported by Carey [14] from iron sulfate, sodium citrate and sodium base mixed with silver nitrate solution under vigorous stirring. The obtained precipitate was filtered, washed with ammonium nitrate and ethyl alcohol and dried in the open air.

2. Characterization

XRD patterns were recorded by X-ray diffractometer (Philips APD-15) at ambient temperature with a constant step of 0.02 s⁻¹ in the range 2θ = 20°- 80° at wavelength λ = 1.54178 Å using a CuKα tube. The Rietveld refinement of the experimental data was performed using the MAUD program.

The microstructure was studied using JSM 6390 scanning electron microscope (Japan) equipped with ultrahigh resolution scanning system (ASID-3D) in regimes of secondary electron image (SEI) and back scattered electrons (BSE) image. The measurements were performed with an accelerating voltage of 20 kV, power of ~65 mA and pressure - 10⁻⁴ Pa.

3. Electrochemical tests

The electrochemical behaviors of the electrodes were examined by cyclic voltammetry (CV), steady-state measurements and charge/discharge tests. Cyclic voltammetry and steady state curves were recorded using Solartron Schumberger 1820 potentiostat and Tacussel (Bi-PAD), supplied by a commercial software. Inert gas (N₂) was purged through the gas-permeable layer during the cycling. The study was carried out in three-electrode electrochemical setup consisting of working electrode (WE), platinum plate counter electrode (CE), and hydrogen electrode as a reference electrode (RE) (“Gascatel”). All tests were carried out at room temperature in electrolyte of 6M KOH aqueous solution.

CV tests were performed in the voltage range of -0.5 +1.5 V (RHE) at scan rate of 50mVs⁻¹.

Charge/discharge tests were performed using three-electrode cell designed by us [15], eight channel Galvanostate 54 (PMC) working in the potential range -1,0 V + 2 V and charge/discharge

current density of ±10mA/cm⁻². The experiment was completed in 6M KOH solution with duration: charge time - 45 min, discharge time -30 min.

4. Electrode preparation

Two WE were prepared: electrode I with NiCo₂O₄ as catalytic material and electrode II – with catalytic material mixture of NiCo₂O₄/Ag.

Working electrode (WE) with geometric surface area of 10cm² was fabricated by pressing of 40 mg/cm² active catalytic layer on the current collector (nickel mesh). The composition of the active layer was: 70 wt.% Ag , 20 wt. % NiCo₂O₄ or NiCo₂O₄/Ag mixed with 10 wt. % PTFE (Teflon emulsion, Sigma Aldrich), 50 mg/cm² conductive agent and binder (teflonized Vulcan XC72 carbon black (Cabot Corporation).

RESULTS AND DISCUSSION

The X-ray analysis of the as-prepared material (Fig.1) proves face-centred cubic NiCo₂O₄ crystalline structure (ICSD № 2421). The Reitveld refinement of the XRD data defines the lattice parameter value a = b = c = 8.110 Å. NiCo₂O₄ and Co₃O₄ have analogous patterns and cell parameters. The obtained value is much closer to that of the standard NiCo₂O₄ cell (8.114 Å) than the value for Co₃O₄ cell (0.8065 nm), ICSD № 27498).

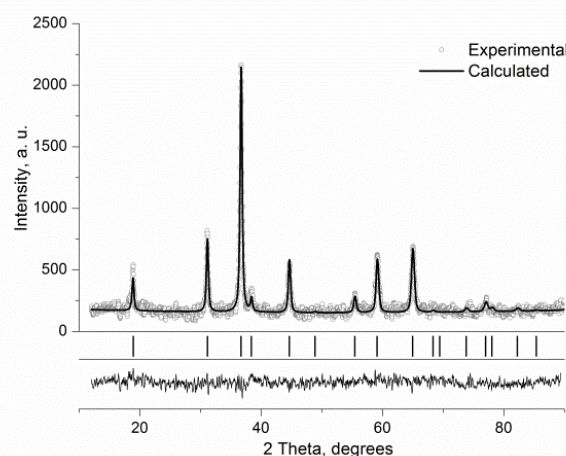


Fig. 1. X-Ray diffraction pattern of NiCo₂O₄ (open circles and Reitveld refinement (straight line). Difference between theoretical and experimental data is shown as bottom line.

Figure 2 presents the XRD patterns of NiCo₂O₄/Ag sample (a) and that of synthesized Ag (b). The peaks on the silver diffractogram define standard FCC structure of Ag (ICSD №. 053761) and lack of silver oxide peaks. In the XRD pattern of NiCo₂O₄/Ag both peaks of NiCo₂O₄ and peaks of metallic silver are visible. The NiCo₂O₄ possesses a face-centered cubic (fcc) spinel structure with Fd3m symmetry with strong (100)

orientation, where all the nickel cations are located in the octahedral positions and the cobalt cations occupy the tetrahedral and octahedral sites.

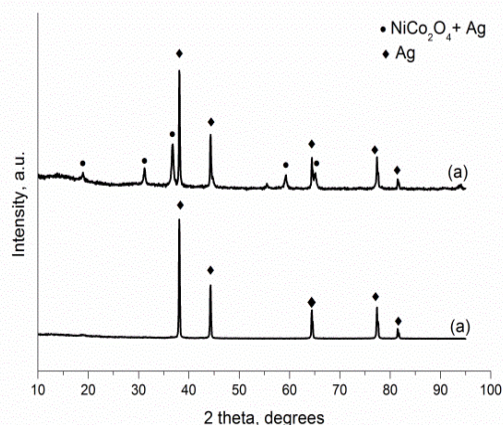


Fig. 2. X-Ray diffraction patterns of NiCo₂O₄/Ag (a) and metallic Ag (b)

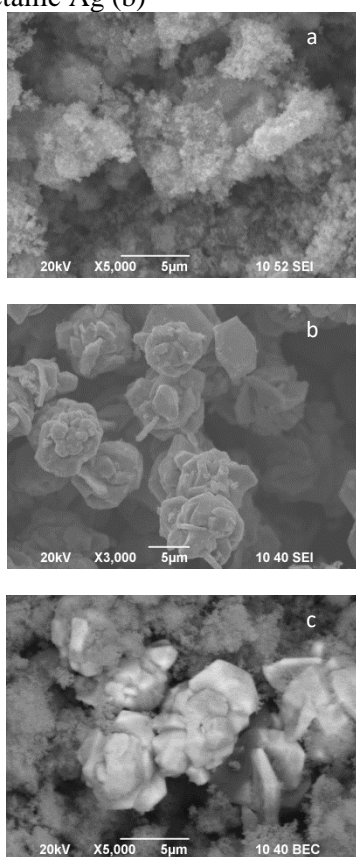
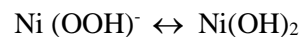


Fig. 3. SEM images: (a) NiCo₂O₄, (b) Ag, (c) NiCo₂O₄/Ag

The SEM images of pure NiCo₂O₄ (a), silver (b) and NiCo₂O₄/Ag (c) are shown in Fig. 3. The morphology of NiCo₂O₄ oxide (a) consists of nanosized spherical particles. Silver particles are bigger in size and clear visible on SEM picture of NiCo₂O₄/Ag sample (c).

The CV-curves of the studied materials depicted in Fig. 4 are conducted at room temperature with a

scan rate of 50 mVs⁻¹. The NiCo₂O₄/Ag electrode (curve II) possesses much broader area indicating a much higher capacitance as compared to the pure NiCo₂O₄ electrode (curve I). The dominant features on the forward scan are generally attributed to a change in oxidation state of Ni ions in the lattices (peaks 1 and 2). The reaction we believe is associated with:



The biggest peak in the curve II, NiCo₂O₄/Ag electrode, at 0.5 mV is due to silver oxidation on the forward scan and to the silver reduction in the reverse scan (peaks 3 and 6). As concerns the peak 4 we suppose it is results of adsorption of OH- while peak 5 is due to oxygen desorption from the electrode surface. The peak 7 and 8 are due to the change in the oxidation state of silver.

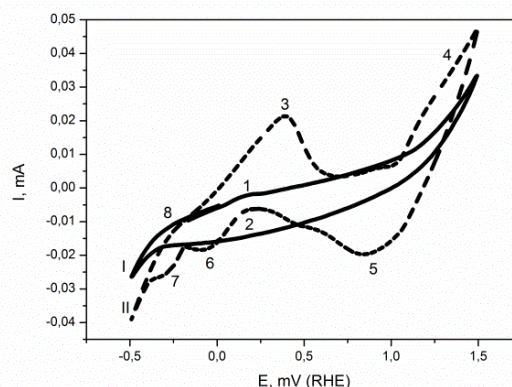


Fig. 4. Cyclic voltammograms of NiCo₂O₄ (I) and NiCo₂O₄/Ag (II) in 6M KOH

The volt-ampere (VA) curves show the catalytic activity of the NiCo₂O₄/Ag and NiCo₂O₄ electrode (fig.5) in the current density range 1–120 mA cm⁻². The silver addition to NiCo₂O₄ increases the catalytic activity of the electrode in ORR reaching a maximum load at current density of 20 mA cm⁻². The deviation in the shape of the curve observed in this graph probably is due to the oxidation of Ag to Ag₂O [16].

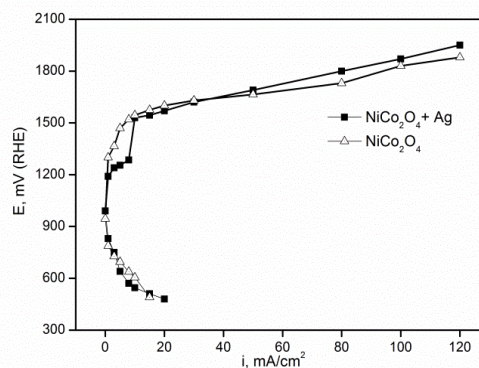


Fig. 5. Polarization curves of NiCo₂O₄ and NiCo₂O₄/Ag

Tafel slopes for cathode and anode reaction are defined from the polarization curves (Fig.6). The Tafel slope, b , is a multifaceted parameter which can give various insights into the efficiency of a reaction. The Tafel slope at lower over potentials is 73 mV dec^{-1} for the anode reaction and 68 mV dec^{-1} for the cathode reaction. The relatively low Tafel slope of the NiCo₂O₄/Ag catalyst indicates high reaction rate for low over potential input. It is often a difficult parameter to interpret as it can depend on several factors including the reaction pathway, the adsorption conditions and the active catalyst layer. The metal oxide/solution interface region consists of an inner anhydrous oxide and an outer, catalytically active hydrated region forming a surfaquo group responsible for the electrochemical activity of the oxide. Lyons and co-workers review the ORR and OER catalytic properties of transition metal oxide materials to determine the reaction mechanism [17]. They emphasize the surfaquo group concept to connect molecular catalysis and heterogeneous catalysis at hydrated oxide surfaces. The metal oxide surface possesses hydrophilic behaviours when immersed in aqueous alkaline solution. As the oxide interacts with water, solvent molecules can bond the metal cations, resulting in the transfer of a proton to a neighbouring oxygen site. Additionally not dissociated water molecules may also exist in the solution. Hence, the surface oxy groups are hydrated or hydroxylated. These hydrated surface species, named “surfaquo group”, may undergo rapid redox transformations involving the simultaneous loss or gain of electrons, protons and hydroxide ions. The electrocatalytic activity of the nickel cobaltite oxide film can be ascribed to the presence of complex anionic surface groups, consisting of octahedrally co-ordinated metal complexes – the surfaquo group [17, 18]. Obviously, the electrochemical performance of NiCo₂O₄ is defined by the presence of the nickel atom with grain size similar to that of the cobalt atom. The presence of both atoms causes change in the crystal structure, in which the defects have some unexpected effects on electrochemical

performance. During the charge-discharge process, fast and reversible faradaic reactions occur on the surface of the electrode leading to the valence state changes of Co³⁺/Co⁴⁺ and M²⁺/M³⁺ (M=Co or Ni).

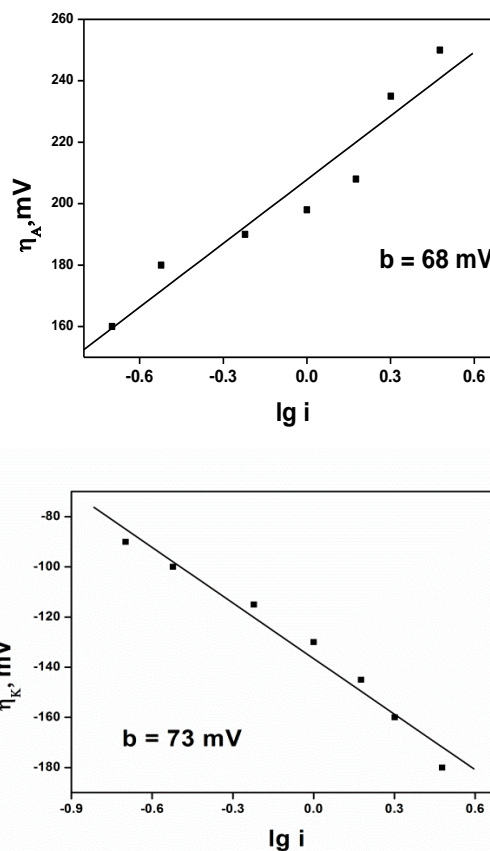


Fig. 6. Tafel plots of NiCo₂O₄/Ag: (a) anode reaction and (b) cathode reaction

The NiCo₂O₄/Ag catalyst examined as bi-functional oxygen electrode achieved 250 charge-discharge cycles without any visible structure changes (Fig.7). During the next cycles it was found to steadily degrade up to 415 charge/discharge cycles. The observed high stability of the BOE is due to both stability of the prepared NiCo₂O₄ catalyst and the design of gas diffusion electrode.

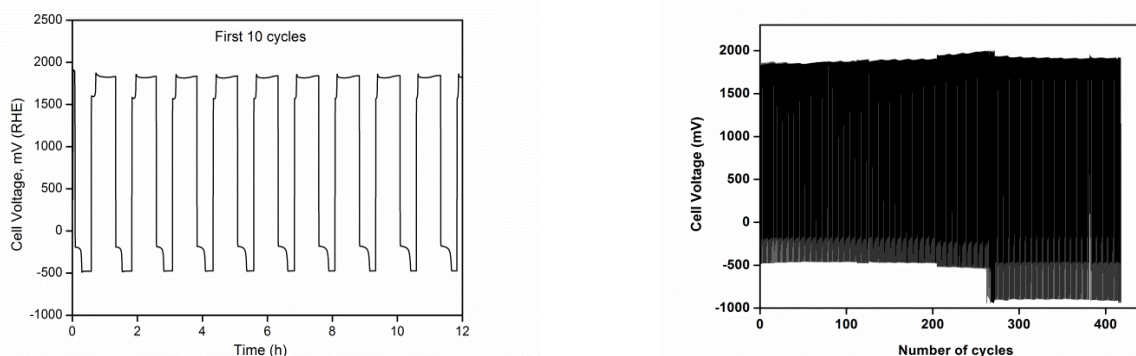


Fig. 7. Charge/discharge tests: (a) first 10 charge/discharge cycles and (b) 415 charge-discharge cycles.

CONCLUSIONS

NiCo₂O₄ catalyst synthesized through precipitation reaction possesses cubic spinel structure confirmed by XRD study. The electrode of NiCo₂O₄/Ag shows good catalytic activity in both oxygen reduction and evolution reactions and exhibits stable-voltage characteristics over 400 charge-discharge cycles.

Acknowledgements The research leading to these results was funded by the European Commission through the project "Zinc Air Secondary innovative nanotech based batteries for efficient energy storage" (ZAS) - Horizon 2020: H2020-NMP-2014. Project number: 646186.

REFERENCES

1. Y. Li, H. Dai, *Chem. Soc. Rev.* **43**, 5257 (2014).
2. T. Danner, S. Eswara, V. P. Schulz, A. Latz, *J. Power Sources*, **324**, 646 (2016).
3. F. Zhan, L.J. Jiang, B.R. Wu, Z.H. Xia, X.Y. Wei, G.R. Qin, *J Alloys Compd.*, **293**, 804 (1999).
4. A.R. Mainar, L.C. Colmenares, J.A. Blázquez, I. Urdampilleta, *Int. J Energy Res.*, 1 (2017).
5. H. Ma, B. Wang, Y. Fan, W. Hong, *Energies*, **7**, 6549 (2014).
6. M. Xu, D. Ivey, Z. Xie, W. Qu, *J. Power Sources*, **283**, 358(2015).
7. P. Sapkota, H. Kim, *J. Ind. Eng. Chem.*, **15**, 445 (2009).
8. G. Du, X. Liu, Y. Zong, T. S. A. Hor, A. Yu, Z. Liu, *Nanoscale*, **5**, 4657 (2013).
9. Y. Li, M. Gong, Y. Liang, J. Feng, J. E. Kim, H. Wang, G. Hong, B. Zhang, H. Dai, *Nat. Commun.*, **4**, 1805 (2013).
10. Z. Chen, A. Yu, R. Ahmed, H. Wang, H. Li, Z. Chen, *Electrochim. Acta*, **69**, 295 (2012).
11. P. Pei, K. Wang, Z. Ma, *Appl. Energy*, **128**, 315 (2014).
12. US Patent No. 4031 033 (1972).
13. I. Iliev, S. Gamburgzev, A. Kaisheva, E. Budevski, *Bulg. Chem. Commun.*, **8**, 359 (1975).
14. M. Carey Lea, *Amer. J. Sci.*, **37**, 476 (1889).
15. B. Abrashev, D. Uzun, H. Hristov, D. Nicheva and K. Petrov, *Advances in Natural Science: Theory and Application*, **2**, 65 (2015).
16. H. M. A. Amin, H. Baltruschat, D. Wittmaier, K. A. Friedrich, *Electrochim. Acta*, **151**, 332 (2015).
17. R. L. Doyle, M. E.G. Lyons, Photoelectrochemical Solar Fuel Production, From Basic principles to Advanced Devices **2**, 92 (2016).
18. B. Marson, N. Fradette, G. Beaudoin, *J. Electrochem Soc.*, **139**, 1889 (1992).

Co-electrodeposition of iron and sulfur in aqueous and non-aqueous electrolytes

V.A Majidzade^{1*}, S. P. Mammadova¹, E. S. Petkucheva, E. P. Slavcheva², A. Sh. Aliyev¹, D. B. Tagiyev¹

¹Acad. M.Nagiyev Institute of Catalysis and Inorganic Chemistry NAS of Azerbaijan, AZ 1143, H.Javid ave. 113, Baku, Azerbaijan

²Acad. Evgeni Budevsk Institute of Electrochemistry and Energy Systems - Bulgarian Academy of Sciences, Akad. G. Bonchev 10, 1113 Sofia, Bulgaria

Received February 07, 2020; Accepted February 20, 2020

The work is devoted to the electrochemical co-deposition of iron and sulfur on Pt substrates from aqueous and nonaqueous electrolytes. The potential range of the single Fe and S and the bi-component Fe-S thin film electrodeposition is determined by applying the potentiodynamic polarization curves. The mechanism of the proceeding faradaic reactions on the surface of the platinum substrate is studied and identified in a broad potential range. The structure, stoichiometry, and morphology of Fe-S thin films deposited by potentiostatic and galvanostatic methods are determined using SEM, EDXA and X-ray phase analysis. The comparison of the results obtained in aqueous and non-aqueous electrolyte showed that Fe-S electrodeposition on the platinum substrate occurs by a similar mechanism in aqueous and non-aqueous electrolytes within a relatively broad potential range as in aqueous media, the process is facilitated due to the higher electrical conductivity of the electrolyte.

Keywords: Fe-S films, electrodeposition, semiconductors

INTRODUCTION

The demand for obtaining two-component or multicomponent semiconductor materials is related both to the development of solar energy, based on the use of thin layers of semiconductor materials and the various practical applications of semiconductor chalcogenides in micro- and optoelectronics [1-9]. Such materials are used to create miniature amplifiers and generators of electrical signals operating in a wide frequency range; integrated circuits for modern computers; converters of one type energy to another one [10-14]; thin-layered solar cells for energy production and storage [15-16]; semiconductor light emitting diodes; lasers and photo-detectors operating within infrared and visible light ranges; components of the fiber optic cables for communication; radiation and particle detectors; magnetic, piezoelectric, ferroelectric and many other devices.

The thin FeS₂ (pyrite) films are known for their valuable properties for photoelectric and photoelectrochemical applications [17]. They are also considered as potential solar absorber material due to several factors among which the main is the suitable gap between their energy zones (0.95 eV) with a high optical absorption coefficient ($\alpha \approx 5 \times 10^5 \text{ cm}^{-1}$) and a sufficiently long minority carrier diffusion length to produce short circuit currents >30 mA. Thanks to the high absorption coefficient, even a very thin FeS₂ film can capture the great part of the reflecting solar radiation, as the theoretical

conversion efficiency is about 20%. In addition, FeS₂ has demonstrated catalytic ability [18]. Finally, Fe and S are extremely widespread, cheap, and non-toxic materials [19].

Various methods are used to obtain thin pyrite films among which gas-phase methods such as sputtering and organometallic chemical vapor deposition [20, 21]; phase-solution methods such as spray pyrolysis, chemical bath deposition [17, 22], electrophoretic deposition, sol-gel [20] and sulfurization of electrochemically deposited Fe-S layers [23-26]. The hydrothermal method is the most attractive synthesis and processing method because it enables ideal control of morphology, purity, crystallinity, composition and low cost for large-scale production [27-29]. The hydrothermal treatment is also testified with respect to annealing, in order to increase efficiency and improve the optoelectronic properties of electrodeposited semiconductor materials [28].

In comparison with the above mention methods, the electrochemical deposition of FeS₂ is relatively simple and very economical [30-31] approach. It does not require expensive equipment and high-temperatures for annealing. The method is very environmentally friendly, has high selectivity, and allows deposition onto complex electrodes of different shapes and large sizes. Electrodeposition in a potentiostatic or galvanostatic mode makes it possible to obtain thin-film semiconductor structures. The goal of this work is to study the mechanism of initial components (Fe and S)

* To whom all correspondence should be sent.

E-mail: vuska_80@mail.ru

electroreduction separately and then to investigate their co- electrodeposition from aqueous and non-aqueous electrolytes, resulting in the formation of thin bi-component Fe-S films.

EXPERIMENTAL

The aqueous and non-aqueous electrolytes used for Fe-S electrodeposition were prepared as Fe- and S- containing salts (0.01 – 0.1 M Fe(NO₃)₃·9H₂O and 0.01 – 0.1 M Na₂S₂O₃·5H₂O) were dissolved separately in bi-distilled water or in ethylene glycol (EG) at a temperature of 313-323 K and then mixed under stirring.

The electrochemical tests were carried out in a three-electrode electrochemical cell with a volume of 100 ml. The working electrode a Pt wire with an area of 0.3 cm² onto which the thin Fe, S, and Fe-S films were deposited. As reference and counter electrodes were used silver/silver chloride (Ag/AgCl/KCl) electrode and a Pt sheet with an area of 4 cm², respectively. Before electrodeposition, Pt electrodes were pretreated in concentrated nitric acid, washed with bi-distilled water, and kept in boiling nitric acid containing a small amount of ferric chloride for 30 minutes. Next, they were thoroughly washed with distilled water and finally rinsed with alcohol or acetone.

The polarization curves were taken using the “IVIUMSTAT Electrochemical Interface” potentiostat. Firstly, the potentiodynamic polarization method was applied to determine the potential region of the single components electrodeposition. For each test, the potential scan rate was adjusted so that the redox peaks on the voltammogram are clearly distinguished. After that Fe, S, and FeS_x were deposited galvanostatically under following conditions: j=22 mA.cm⁻², t=15 min, bath composition 0.05 M Fe(NO₃)₃·9H₂O + 0.5 Na₂S₂O₃·5H₂O in aqueous media or in ethylene glycol r non aqueous solutions.

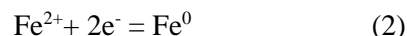
The surface structure and morphology of the as prepared films were studied by X-ray diffraction (XRD). The diffraction data were collected using X-ray diffractometer PhilipsADP15 with Cu-Kα(λ=1.54178 Å) radiation at a constant rate of 0.20 s⁻¹ over an angle range 2θ-10-900.

The crystal structure and phase identification of the catalytic films were examined by scanning electron microscopy (SEM) with a JEM-200CX, JEOL (80 keV accelerating voltage and magnification up to 100,000) microscope.

RESULTS AND DISCUSSION

Figure 1 shows the polarization curve recorded in aqueous electrolyte, containing: 0.1M Fe(NO₃)₃·9H₂O. As can be seen, there are two well-

shaped current peaks on the curve, related to electroreduction of iron ions on the substrate surface. The first peak formed in the potential range from 0.68 to -0.36 V is due to reduction of Fe (III) to Fe (II) (eq.1), while the second peak situated at potentials from -0.36- to -0.8 V can be prescribed to further reduction of Fe (II) to atomic iron in a two-electron reaction (eq. 2) [32].



At potential values more negative than -0.8 V, metallic iron is deposited on the substrate.

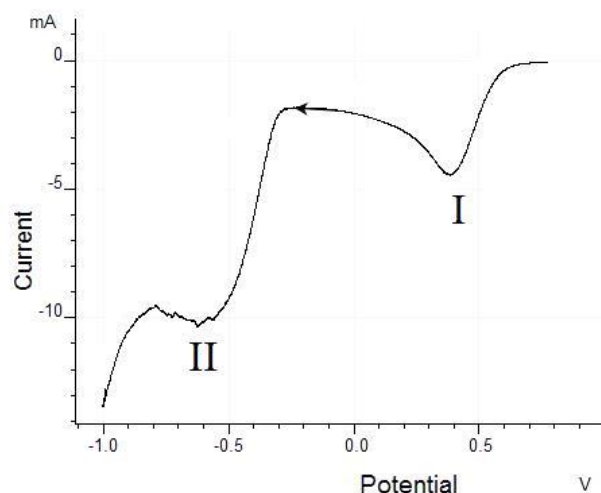
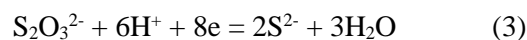


Fig. 1. Potentiodynamic polarization curve presenting the electroreduction of Fe³⁺ ions on Pt electrode in 0.1M Fe (NO₃)₃ aqueous electrolyte; scan rate 0.04 (V.s⁻¹); temperature 293 K

The electroreduction process of thiosulfate ions from an aqueous 0.1M Na₂S₂O₃ electrolyte is shown in Figure 2. It can be seen that this reaction occurs in the potential range from -0.3 to -0.9 V in one stage according to eq. (3):



After determining the range of potentials where the electrochemical reduction of individual components occurs, the co-electrodeposition of iron and sulfur from mixed 0.1 M Fe(NO₃)₃ + 0.1M Na₂S₂O₃ aqueous electrolyte was studied. Figure 3 shows the obtained cyclic potentiodynamic curve. As it is seen, several cathodic and anodic peaks are observed in the course of the process.

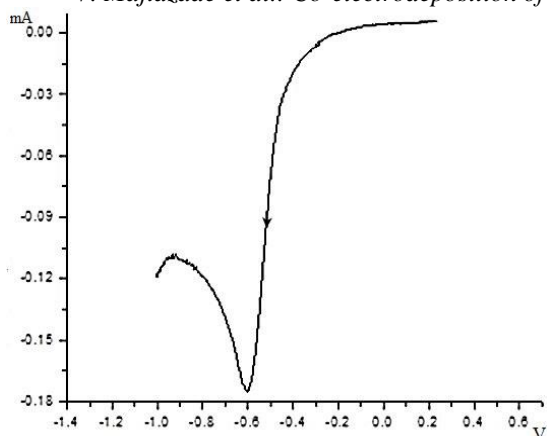


Fig. 2. Potentiodynamic polarization curve presenting the electroreduction of thiosulfate ions on Pt electrode from aqueous 0.1M Na₂S₂O₃ electrolyte; scan rate 0.02 V.s⁻¹; temperature 293 K

On the cathode part of the curve, within the potential interval from 0.65 V to -0.63 V, reduction peaks (I and II) of thiosulfate to sulfide ions is observed. The reaction proceeds according the eq. (4):

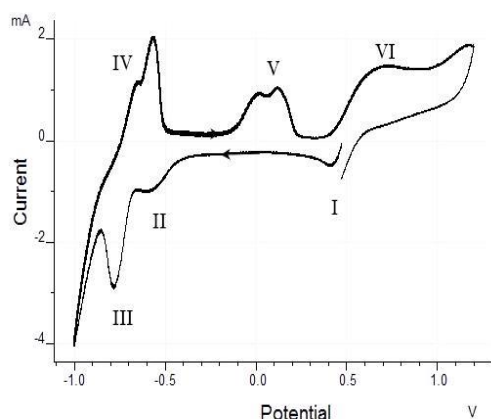
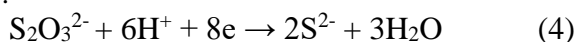
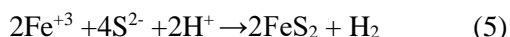


Fig. 3. Potentiodynamic cyclic polarization curve of co-electrodeposition of Fe and S on Pt electrode from 0.1 M Fe(NO₃)₃ + 0.1M Na₂S₂O₃ aqueous electrolyte; scan rate 0.08 V.s⁻¹; temperature 293 K

In the following section of the cathodic polarization curve (from -0.7 to -0.9 V), co-deposition of Fe-S occurs (peak III) according to the eq. (5):



Then, at potentials more negative than -0.87 V trivalent iron is reduced and deposited on the surface in atomic state.

On the anode branch of the cyclic polarization curve, first the processes of dissolution of iron to Fe²⁺ and Fe³⁺ ions (peak IV) occurs, then the deposited FeS₂ dissolves to Fe³⁺ and S²⁻ ions (peak

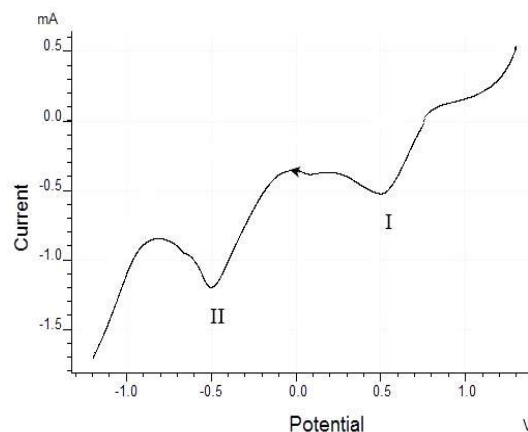


Fig. 4. Potentiodynamic polarization curve presenting the electroreduction of Fe³⁺ ions on Pt electrode in nonaqueous 0.1M Fe(NO₃)₃ + CH₂OH-CH₂OH electrolyte; scan rate 0.02 V, temperature 293 K V). The last peak VI corresponds to dissolution of S²⁻ to elemental S⁰.

For comparison, the same experiments were carried out using non-aqueous ethylene glycol solutions. Figure 4 shows the polarization curve of the process of electroreduction of Fe³⁺ ions on Pt electrode from EG solution of 0.1M Fe(NO₃)₃.

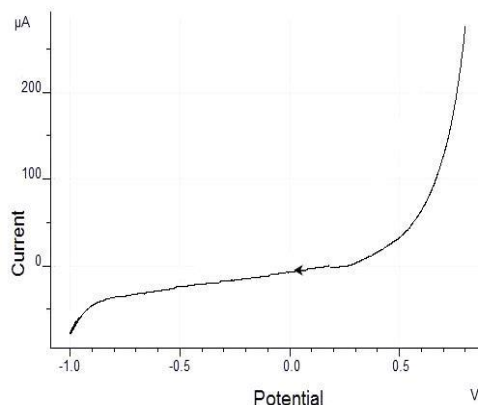


Fig. 5. Potentiodynamic polarization curve presenting the electroreduction of thiosulfate ions on Pt electrode in 0,1 M Na₂S₂O₃ nonaqueous EG electrolyte; scan rate 0.02 V/s; temperature 293 K

The comparison of Figure 1 and Figure 4, shows that the electroreduction of Fe³⁺ ions in an aqueous and nonaqueous media occurs by the same mechanism with slight differences in the rate of the surface reactions due to the difference in electrical conductivity of both electrolytes.

In the case of thiosulfate ions, the electroreduction also occurs in a single stage, but at more negative potentials. The comparison of Figure 2 and Figure 5 shows that in aqueous media, the process begins at the potential value of -0.3 V, while in non-aqueous media this occurs at much more negative potentials (-0.9 V).

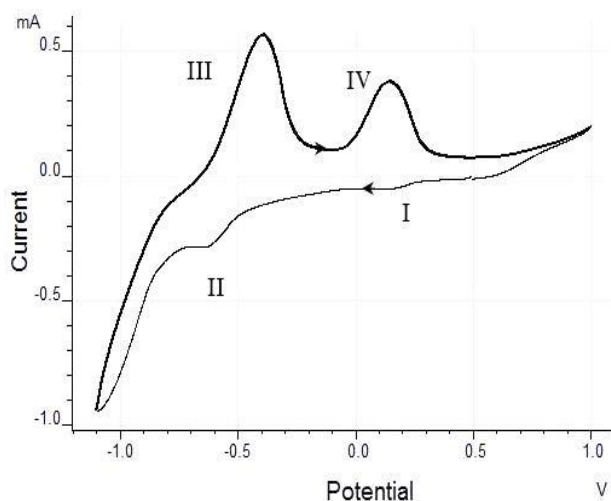


Fig. 6. Potentiodynamic cyclic polarization curve presenting the co-electrodeposition of Fe and S on Pt electrode from a mixed 0.1M $\text{Fe}(\text{NO}_3)_3$ + 0.1M $\text{Na}_2\text{S}_2\text{O}_3$ non-aqueous (EG) electrolyte; scan rate 0.03 V/s, temperature 293 K

Figure 6 shows the electrochemical co-deposition of Fe and S from an ethylene glycol solution. On the cathode part of the curve, two current peaks are distinguished. The first peak (I) appears in the potential range from 0.60 to 0.35 V and is related to reduction of Fe^{3+} to Fe^{2+} ions. Further reduction of iron is observed in the potential range from -0.45 to -0.73 V (peak II), while the process of Fe-S co-deposition starts at around -0.9 V and intensifies at more negative potentials. The assumed reaction mechanism at the reverse potential scan includes the dissolution of the obtained Fe-S film in the potential range from -0.65 to -0.3 V, (peak III), while at potentials from -0.1 to 0.25 V (peak IV), thiosulfate ions dissolve with the formation of various ions.

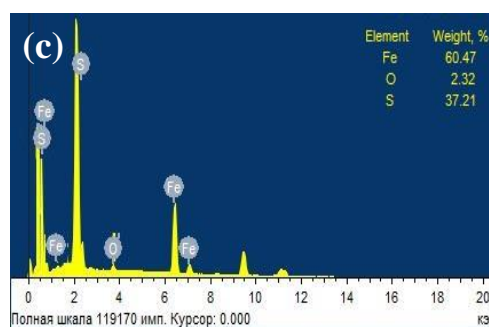
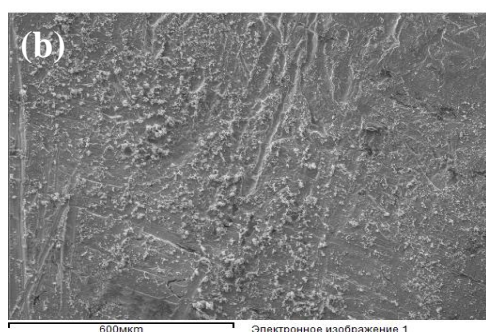
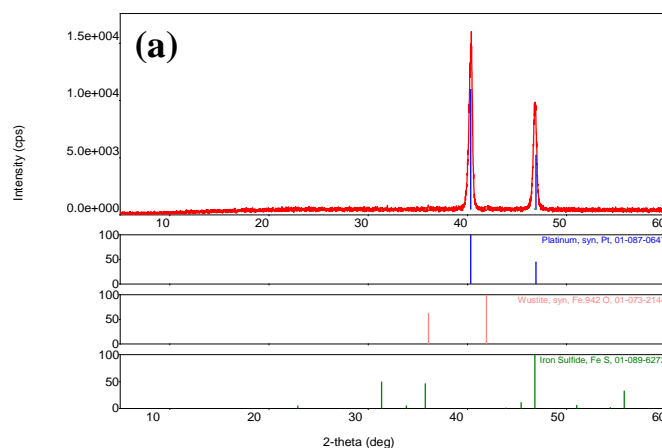


Fig. 7. XRD pattern (a), EDAX (b) and SEM (c) image of thin Fe-S films on a Pt electrode from aqueous electrolyte

The obtained samples were studied using SEM and X-ray phase analysis. The data obtained are shown in Figures 7 and 8. The results prove the co-electrodeposition of Fe and S on the Pt for both studied samples. The XRD patterns of the samples obtained from aqueous and non-aqueous electrolytes consist of two phases, which conform to Fe-S and iron oxides.

The EDAX analysis also shows the spectra of iron, sulfur, and oxygen. In samples obtained from a non-aqueous electrolyte, oxygen spectra are not seen. Therefore, it can be assumed that the films obtained from ethylene glycol solution are of higher quality, since the composition of these films is closer to the stoichiometric composition of FeS and they have better adhesion to the electrode surface.

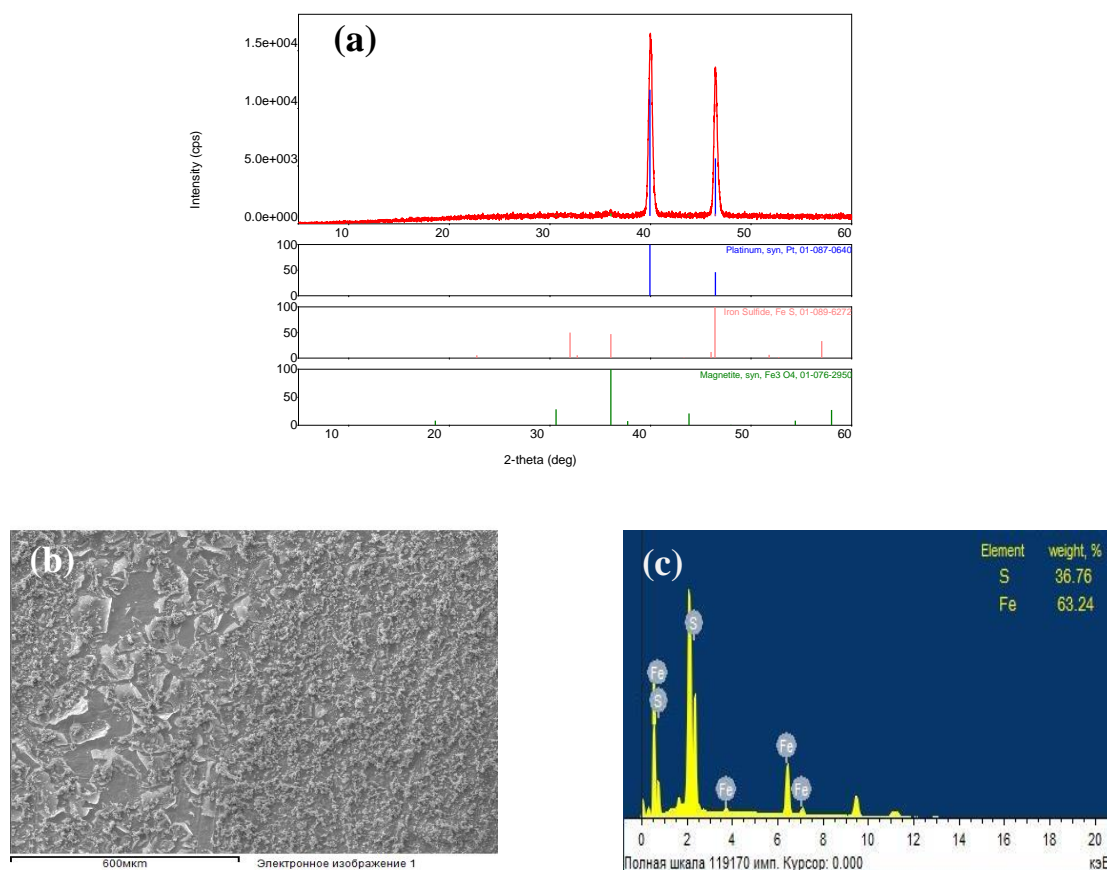


Fig. 8. XRD pattern (a), EDAX (b) and SEM (c) image of thin Fe-S films on a Pt electrode from non-aqueous (EG) electrolyte

CONCLUSIONS

The research performed demonstrated that the electrochemical co-deposition is an easy and efficient approach to obtain bi-component semiconductor materials. It was found that the Fe-S electrodeposition on the platinum substrate from aqueous and non-aqueous ethylene glycol electrolytes occurs by a similar mechanism of the proceeding surface reactions within a relatively broad potential range. The Fe-S co-deposition in aqueous electrolyte starts at about -0.4 V, while in EG the reaction is shifted to much negative potential of about -0.9 V. Thus, it can be concluded that in aqueous media, the process is facilitated due to the higher electrical conductivity of the electrolyte. Further research is currently in progress to investigate how the type of electrolyte affects the mechanical and corrosion stability, as well to evaluate photosensitive and electrocatalytic properties of the electrodeposited Fe-S films.

Acknowledgment: The research has been supported by bilateral agreement between Acad. M.Nagiyev Institute of Catalysis and Inorganic Chemistry (Azerbaijan National Academy of

Sciences, ANAS) and Acad. Evgeni Budevsk Institute of Electrochemistry and Energy Systems (Bulgarian Academy of Sciences, BAS), Project "Electrochemical and photoelectrochemical application of hybrid $FeCh_x-TiO_2-MoS_x$ cathodes" (2018-2020)

REFERENCES

1. P. Tonndorf, R. Schmidt, P. Böttger, X. Zhang, J. Borner, et al. *Opt. Express*, **21**, 4908 (2013).
2. G. M.Huseynov, N. A. Mammadova, H. A. Imanov, *Chem. Problems*, **15**, 329 (2017).
3. W. He, H. Zhang, Y. Zhang, M. Liu, X. Zhang, F. Yang, *J. Nanomater.* (2015)
4. V.A., Majidzade, *Chem.I Problems.*, **16**, 331 (2018).
5. A. Sh. Aliyev, V. A. Majidzade, N. Sh. Soltanova, D. B. Tagiyev, V. N. Fateev, *Chem.Problems.*, **16**, 178 (2018).
6. D. S. Sofronov, E. A. Vaksler, Y. A. Bondarenko, V.V. Starikov et. al., *Inorg. Mater.*, **52**, 1205 (2016).
7. C. Agapescu, A. Cojocaru, A. Cotarta, T. Visan. *J. Appl. Electrochem.*, **43**, 309 (2013).
8. V. A. Majidzade, S. F. Cafarova, A. Sh. Aliyev, D. B. Tagiyev, *Azərb. Kimya J.*, **3**, 6 (2018).
9. E.A., *Streltsov Bulletin of BSU.*, Ser. **2.**, 1 (2011).

10. Ch. Li, F. Wang, Y. Chen, L. Wu, J. Zhang, et. al., *Mater. Sci. Semicond. Process.*, **83**, 89 (2018).
11. W. Liyanage, J. Wilson, Ed. Kinzel, B. Durant, Nath. Manashi, *Sol. Energy Mater. Sol. Cells*, **133**, 260 (2015).
12. D. Boosagulla, Sr. Mandati, R. Allikayala, B. V. Sarada, *ECS J. Solid State Sci. Technol.*, **7**, 440.
13. Ch. Chen, D. C. Bobela, Y. Yang, Sh. Lu, et. al. *Front. Optoelectron.*, **10**, 18 (2017).
14. S. Im, C.S. Lim, J. Chang, Y. Lee, N. Maiti et. al., *Nano Lett.*, **11**, 4789 (2011).
15. V. N. Fateev, O. K. Alexeeva, S. V. Korobtsev E. A. Seregina, et. al., *Chem. Problems*, **16**, 4, 453 (2018).
16. T. L. Kulova, I. I. Nikolaev, V. N. Fateev, A. Sh. Aliyev, *Chem. Problems.*, **16**, 9 (2018).
17. V. Aluri, K. T. Reddy, Y. M. Reddy, *Nanotechnol. Rev.* , **4**, 469 (2015).
18. Jasion D. Thesis , 2015
19. Sh. Kawai, R. Yamazaki, S. Sobue, E., Okuno, M. Ichimura, *APL Materials*, **2**, 032110 (2014) .
20. S. Seefeld, M., Limpinsel, Y. Liu, N. Farhi, et. al. *J. Am. Chem. Soc.*, **135**, 4412 (2013).
21. S. Kment, H. Kmentova, A. Sarkar, R. J. Soukup, et.al. *J. Alloys Compd.*, **607**, 169 (2014).
22. K. Anuar, W. T. Tan, N. Saravanan, S. M. Ho, S. Y. Gwee, *Pac. J. Sci. Technol.*, **10**, 801 (2009).
23. X. Wang, G. Wang, J. Chen, X. Zhu, et. al., *Mater. Lett.*, **110**, 144 (2013).
24. A. Gomes, J. R. Ares, I. J. Ferrer, M. I. S. Pereira, C. Sanchez, *Mater. Res. Bull.*, **38**, 1123 (2003).
25. Y. Z. Dong, Y. F. Zheng, H. Duan, Y. F. Sun, Y. H. Chen, *Mater. Lett.*, **59**, 2398 (2005).
26. Y. Z. Dong, Y. F. Zheng, X. G. Zhang, H. Duan, et. al., *Sci. China Ser. E*, **48**, 601 (2005).
27. S. Nakamura, A. Yamamoto, *Sol. Energy Mater.Sol. Cells*, **65**, 79 (2001).
28. N. Yu, L. Du, H. Du, Z. Mao, et. al. *Thin Solid Films*, **550**, 206 (2014).
29. R. Henríquez, C. Vasquez, N. Briones, E. Muñoz, P. Leyton, E. A. Dalchiele, *Int. J. Electrochem. Sci.*, **11**, 4966 (2016) .
30. P. Prabukanthan, R. Lakshmi, T. R. Kumar, S. Thamaraiselvi, G. Harichandran, *Adv. Mater. Proceedings*, **2**, 521 (2017).
31. M. Ichimura, T. Kajima, Sh. Kawai, K. Mibu, *Jpn. J. Appl. Phys.*, **55**, 038006 (2016).
32. A.A. Sukhotin (Ed): Handbook of Electrochemistry, Chemistry, Leningrad, Russian, 1981, p.488.

Effect of ball milling treatment on the Zn electrode properties in Ni- Zn battery

G. D. Ivanova¹, V. P. Petrova², O. K. Petkov², B. A. Minchev², P. A. Lilov², A. K. Stoyanova- Ivanova², A. E. Stoyanova¹

¹*Institute of Electrochemistry and Energy System "Academician Evgeni Budevski ", Bulgarian Academy of Sciences, Acad. Georgi Bonchev Str, Block 10, 1113 Sofia, Bulgaria*

²*Georgi Nadjakov Institute of Solid State Physics, Bulgarian Academy of Sciences, 72 Tzarigradsko Chaussee Blvd., 1784 Sofia, Bulgaria*

Received February 18, 2020; Accepted March 14, 2020

This study is focused on the improvement of the properties of the nickel-zinc battery through ball mill treatment of the Zn-electrode active mass. Three zinc electrodes with carbon additive, two of them mixed with conductive ceramic additives from the Bi-Sr-Ca-Cu-O (BSCCO) system with nominal chemical composition $\text{Bi}_{1.7}\text{Pb}_{0.3}\text{Sr}_2\text{CuO}_x$ (B(Pb)SCO 2201) and $\text{Bi}_{1.7}\text{Pb}_{0.3}\text{Sr}_2\text{CaCu}_2\text{O}_x$ (B(Pb)SCCO 2212), were investigated. The phase composition and morphology of the as-prepared samples were characterized by scanning electron microscopy (SEM) and X-ray diffraction (XRD). The conductivity of the Zn electrodes was examined by Potentiostatic Electrochemical Impedance Spectroscopy (PEIS) and it was found that the ball mill treatment of the electrodes with BSCCO additives increases their overall resistance.

Keywords: Ni- Zn battery, through ball mill treatment, Zn-electrode, conductive BSCCO ceramic additives

INTRODUCTION

The nickel-zinc battery is one of the most significant energy storage systems for various electrical applications due to moderate specific energy (55-85 Whkg⁻¹), high specific power density (140-200 Wkg⁻¹), high open circuit potential (1.705 V), and nominal cell voltage of 1.6 V [1,2]. These batteries have attractive, such as being low cost, environmentally friendly and having abundant resources of raw materials. However, they have not reached their full potential mostly due to critical problems with the zinc electrode. These problems are attributed to the shape change of the electrode with increasing charge/discharge cycle count, zinc electrode passivation, and dendritic zinc growth leading to short – circuiting of the battery. During the discharge process, zincate ion ($\text{Zn}(\text{OH})_4^{2-}$) in the alkaline electrolyte is formed before zinc oxide precipitates. During the charging process, the concentration of zincate ions near the bottom of the electrode decreases and zincate ions are precipitated as zinc oxide when the limit of solubility is reached. This process leads to shape change and formation of zinc dendrites as well as protrusion on the surface of zinc electrode with increasing the number of charge/discharge cycles [3].

Passivation is also another serious problem for deterioration of zinc-based batteries. The passivation of the zinc electrode occurs when the solubility of the zincate ions is exceeded in the electrolyte close to the surface of the zinc electrode,

and an insulating ZnO barrier layer is formed on the electrode surface. Due to these issues, short cycle life and/or poor electrochemical performance have limited the wide-range application of Ni-Zn batteries.

There are approaches to solving the existing problem, one of them being the introduction of conductive ceramic additives to the zinc electrode mass. Our previous researches have shown that the nickel-zinc battery cell with zinc electrode whose active mass contain superconducting B(Pb)SCCO (2212) and B(Pb)SCO (2201) ceramic additive exhibits increased cycling and performance stability during prolonged charge-discharge [4-6]. It is supposed that the superconducting powder forms a highly conductive network between the particles of the zinc oxide in the electrode mass, thus improving the electric contact in the power generation material of the zinc electrode. The addition of BSCCO ceramics improves not only the conductivity and electrochemical homogeneity of the electrode mass and reduces the gas evolution (because of the absence of carbon materials with low- overpotential of hydrogen evolution), but it also stabilizes its porous structure [7-9].

The optimization of the zinc electrode mass, including the homogeneous particle distribution of zinc oxide and ceramics, is very important for the robust operation of the battery. The method of electrode preparation can modify the surface morphology and, consequently, the affinity between the particles, which is beneficial to improve the

* To whom all correspondence should be sent.
E-mail: galia.ivanova@iees.bas.bg

cyclic stability of the electrode. Therefore, the correct choice of active mass preparation has significant effect on the electrochemical properties of the electrode.

A simple effective method to improve the rate capability and reduce the initial voltage delay without compromising the capacity of the active material is the ball milling treatment [10, 11]. Although it may not be as effective as some soft chemical methods that can elaborately tailor the physicochemical nature of the final products, the mechanochemical method is, due to its simplicity and easy operation, attractive and in principle applicable to different electrode materials with poor structural integrity. It is found that the high-energy ball-milling, brings considerable effects on the structure, morphology, and size distribution of the electrode materials, thereby modifying their electrochemical behavior [12, 13].

Improved electrochemical activity (increased capacity, stable cycling behavior, and good rate capability) of LiMnPO_4 ball-milled with 8 wt. % acetylene black has been established and this effect may be attributed to enhanced kinetics and structure integrity, which are related to the decreased particle size, expanded unit cell volume, and crystal defects. It is believed that the activity of LiMnPO_4 can be further improved given that the ball-milling parameters like time, material/ball ratio, and conductive additive are optimized [2].

Our previous work has shown that the active mass with carbon and B(Pb)SCO 2201 additive has superior particle distribution compared to the other two samples (with B(Pb)SCCO 2212 and without ceramic additive) after ultrasound treatment while the composition of the active mass is preserved [14].

These results and the results, obtained from other authors in different systems [2, 10-13] provoked our interest to conduct similar studies by processing the active mass in a ball mill. The aim of this work is to determine the effect of ball mill treatment on the physicochemical and electrochemical properties of the negative active mass in Ni/Zn cell, as compared with an untreated electrode mass.

EXPERIMENTAL

Preparation of the B(Pb)SCCO conductive ceramic additives

The powder sample of conductive ceramic additives from the Bi-Sr-Ca-Cu-O (BSCCO) system with nominal chemical composition $\text{Bi}_{1.7}\text{Pb}_{0.3}\text{Sr}_2\text{CuO}_x$ (B(Pb)SCO 2201) and $\text{Bi}_{1.7}\text{Pb}_{0.3}\text{Sr}_2\text{CaCu}_2\text{O}_x$ (B(Pb)SCCO 2212) are prepared by the standard solid state reaction. High-

purity (99, 99 %) oxides and carbonates (Bi_2O_3 , PbO , CuO , SrCO_3 and CaCO_3) were used for the production of the Bi-Sr-Ca-Cu-O system samples. The powder is thoroughly mixed, ground and initially heat treated at 780 °C for 24 hours in air. Afterwards the obtained mass is ground and pressed (5-6 MPa) into round tablets 9.8 mm in diameter and 1.8 mm in thickness. The tablets are then sintered again: B(Pb)SCCO 2212 at 830 °C for 48 hours and B(Pb)SCO 2201 at 830 °C for 24 hours in air atmosphere (in accordance with established procedure [15]). BSCCO tablets were ground again and the powder was used as an additive to the active mass.

Preparation of the active mass

An electrode mass was composed of powder ZnO (NZN050, Anhui Elite Industrial Co., LTD, Hong Kong Elite Industrial Group Limited) (67 %), acetylene black (14 %) and binding agents – polytetrafluorethylene (PTFE, 5 %) and carboxymethylcellulose (CMC, 14 %). Two other were prepared with acetylene black (7 %), additives – conducting ceramic powder B(Pb)SCO 2201 and B(Pb)SCCO 2212 (7 %) respectively and the same binding agents. The prepared composite of zinc oxide and additives was sequentially plasticized with PTFE suspension and with CMC and mixed manually to form a mushy paste [16]. For better mixing, the active mass was also homogenized in a ball mill for 1 hour at room temperature (23 °C).

Preparation of the zinc electrodes

The pasted zinc electrodes prepared by inserting the zinc paste in the matrix of copper foam (successively covered with tin and zinc) with dimensions 2,0 x 2,0 cm (thickness 0,15 cm) are used for current collector and carrier of the zinc mass. The pasted electrode is dried at 70 °C for 2 hours and then pressed under 30 MPa for 2 min. The paste was applied to form uniform layer.

Physicochemical characterization of electrode materials

The following methods are used for physicochemical and electrochemical characterization of the investigated substances: X-ray diffraction (XRD), Scanning Electron Microscopy (SEM) and Potentiostatic Electrochemical Impedance Spectroscopy (PEIS).

The samples were examined using a Philips X-ray diffractometer PW 1030 having a θ -2 θ Bragg-Brentano geometry, with Cu $K\alpha$ radiation (30 kV, 20 mA) with a wavelength $\lambda = 1.5406 \text{ \AA}$ and a scintillation detector. The original radiographs were obtained at room temperature and a constant scan rate and a reflection angle of 2 θ in the interval 5 ÷ 90° with a step of 0.04°. The

diffraction patterns obtained were interpreted by the PCPDFWIN database, ICDD, 2002

The microstructure of the prepared active masses was studied by JOEL-200 CX scanning electron microscope (SEM) with LaB₆ cathode on the polished cross-section of the samples, at 80 keV.

Electrochemical impedance spectroscopy measurements

The electrochemical system SP-200: potentiostat/galvanostat was used to perform potentiostatic electrochemical impedance spectroscopy (PEIS) measurements. The obtained impedance spectra were fitted to an equivalent circuit model using the EC-Lab software. PEIS measurements were taken using the ZnO electrodes as the working electrode (WE) in a three electrode electrochemical cell. The counter-electrode (CE) was a platinum plate. Potential was measured relative to a saturated calomel reference electrode (RE). The applied sine-wave potential amplitude is 10 mV. In some cases a higher potential of 20 or 30 mV was required in order to obtain noise free data. In all experiments the frequency was swept from 1 MHz down to 0.1 Hz. The supporting electrolyte was 7M KOH. Impedance spectra were taken at 25 °C in order to examine electrode kinetics near working condition.

RESULTS AND DISCUSSION

The XRD patterns of the ball mill and mechanically mixed electrode masses are compared in Fig.1.

Based on XRD analysis of the two electrode masses, containing B(Pb)SCCO additives a single well-crystallized phase of the ceramic is observed. Secondary phases are not detected. The ball mill treatment only affects the active mass with B(Pb)SCO 2201 ceramic. There is a slight broadening of the diffraction peaks, indicating a decrease of the particle size during ball mill processing. In the other two samples, the treatment method has no impact on the structure of the active mass.

The morphology of the active electrode mass is the next parameter that influences the electrode performance. In Figure 2 the SEM images of the Zn active mass with carbon, B(Pb)SCO 2201 and carbon and B(Pb)SCCO 2212 and carbon – additives, treated mechanically and by ball milling are compared.

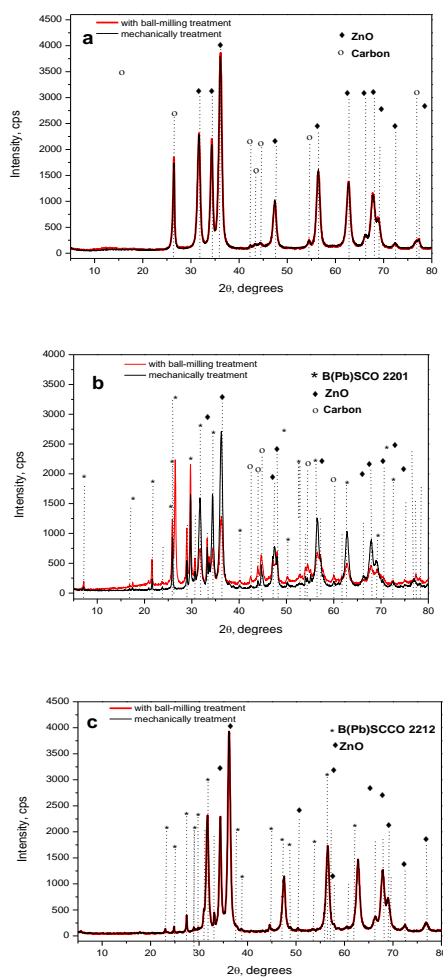


Fig. 1. Powder X-ray diffraction patterns of the Zn active mass with B(Pb)SCO 2201+ carbon (a), B(Pb)SCCO 2212 + carbon (b) and carbon (c), prepared with mechanical (black lines) and ball mill (red lines) mixing

The ball mill assisted mixing of the active mass leads to very good ceramic and carbon particle distribution (Fig. 2). The SEM images of the active mass display a formation of relatively homogenous surface with fine-grained structure. The sample with B(Pb)SCO 2201 shows a particle reduction after ball milling that is consistent with XRD images (Fig. 1b). The results presented so far correlate well with those of our previous studies according to which ultrasound treatment mainly affects the active mass with carbon and B(Pb)SCO 2201 additive [14]. The morphology of the active electrode mass is the next parameter that influences the electrode performance. In Figure 2 the SEM images of the Zn active mass with carbon, B(Pb)SCO 2201 and carbon and B(Pb)SCCO 2212 and carbon – additives, treated mechanically and by ball milling are compared.

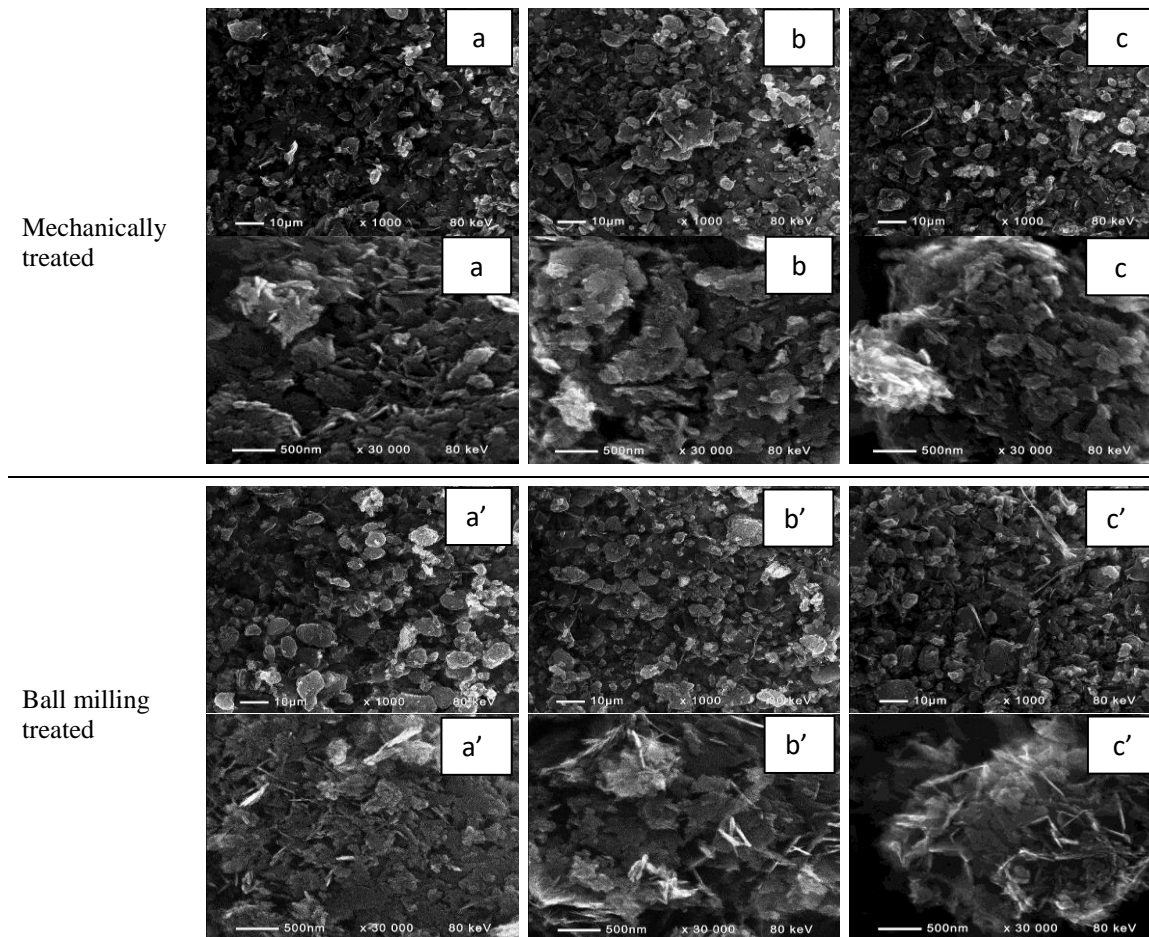


Fig. 2 SEM images of the Zn active mass with carbon (a, a'), B(Pb)SCO 2201+carbon (b, b') and B(Pb)SCCO 2212+carbon (c, c') with mechanical and ball mill treatment

The ball mill assisted mixing of the active mass leads to very good ceramic and carbon particle distribution (Fig. 2). The SEM images of the active mass display a formation of relatively homogenous surface with fine-grained structure. The sample with B(Pb)SCO 2201 shows a particle reduction after ball milling that is consistent with XRD images (Fig. 1b). The results presented so far correlate well with those of our previous studies according to which ultrasound treatment mainly affects the active mass with carbon and B(Pb)SCO 2201 additive [14].

Probably the different structure and composition of the two ceramics is responsible for the observed effect. Electrochemical tests were conducted to interpret these results further. The Nyquist plots of zinc electrodes with carbon and carbon and ceramic additives, mixed in ball mill have been recorded (Fig. 3). These measurements are compatible with our previous studies on the impedance of Zn electrode mass after mechanically and ultrasound treatment [14]. On the graph the electrode resistance is determined by the high frequency intercept of the curves with the real axis. Calculated impedance parameters, using the equivalent circuit

model describing PEIS (Fig. 3, insert) are given in Table 1.

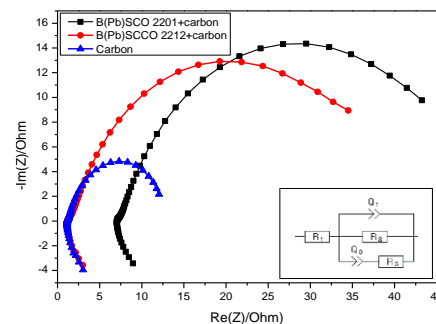


Fig. 3 Nyquist impedance plot of ZnO electrodes with carbon, B(Pb)SCO 2201+carbon and B(Pb)SCCO 2212+carbon at 25°C with ball milling treatment (insert figure - equivalent circuit model for electrode)

The results show that the electrode with B(Pb)SCO 2201 additive exhibits significantly higher resistance, compared to the other two samples. This can be due to the changes in an electronic conduction path in the electrode matrix when treated with a ball mill and respectively to the worsening of its electrochemical characteristics. Not well-chosen ball milling parameters like time,

fluid, material/ball ratio and conductive additive is another possible cause of the obtained effect [17].

Table 1. Calculated impedance parameters of ball mill treated electrodes (the data presented are from measurements taken with an applied potential of 20 mV)

| Parameter | Carbon (C) | B(Pb)SCO 2201+C | B(Pb)SCCO 2212+C |
|-----------------------|-----------------------|-----------------------|-----------------------|
| R_1, Ω | 1.18 | 7.05 | 1.15 |
| Q_1, Fs^{-1} | 16.5×10^{-3} | 9.08×10^{-3} | 9.2×10^{-3} |
| a_1 | 0.952 | 0.708 | 0.681 |
| R_2, Ω | 11.95 | 43.54 | 39.41 |
| Q_3, Fs^{-1} | 27.5×10^{-3} | 1.78×10^{-3} | 2.25×10^{-3} |
| a_3 | 0.825 | 0.905 | 0.938 |
| R_3, Ω | 0.65 | 4.5 | 3.75 |

CONCLUSIONS

In this work the effect of the ball mill mixing of the active mass on the Zn- electrode characteristics is discussed. XRD analysis shows that the composition of the active mass is preserved during the grinding process. There is no significant change in the active mass morphology after ball mill treatment. BSCCO additives increase the overall resistance of the electrode, which adversely affects the electrochemical characteristics of the electrode, respectively of the battery. The use of ball mill assisted mixing for preparation of the Zn-electrode active mass is not appropriate in the current conditions until further optimization is done.

Acknowledgments: The financial support of the Bulgarian National Scientific Fund under project № KII-06-M29/3 is gratefully appreciated.

REFERENCES

- G. Payer, O. Ebil, *J. Nanomater.*, **17**, 75-84 (2016).
- J. Ni, Y. Kawabe, M. Morishita, M. Watada, T. Sakai, *J. Power Sources*, **196**, 8104 – 8109 (2011).
- G. Cihanoglu, O. Ebil, *J. Turkish Chemical Soc. Chem.*, **5**, 65-84 (2018).
- G. Ivanova, L. Stoyanov, S. Terzieva, A. Stoyanova-Ivanova, M. Mladenov, D. Kovacheva, R. Raicheff, *BPS*, **14**, 33-34 (2014).
- G. Ivanova, L. Stoyanov, A. Stoyanova, M. Mladenov, R. Raicheff, *BPS*, **16**, 27-29 (2016).
- G. Ivanova, A. Stoyanova-Ivanova, D. Kovacheva, A. Stoyanova, *Bulg. Chem. Com.*, **51**, 66 – 72 (2019).
- G. Ivanova, L. Stoyanov, S. Terzieva, A. Stoyanova-Ivanova, M. Mladenov, D. Kovacheva, R. Raicheff, *Nanosci. Nanotechnol.*, **14**, 33 (2014).
- L. Stoyanov, S. Terzieva, A. Stoyanova, A. Stoyanova-Ivanova, M. Mladenov, D. Kovacheva, R. Raicheff, *JPRC*, **2**, 83 - 91 (2016).
- G. Ivanova, L. Stoyanov, A. Stoyanova, M. Mladenov, R. Raicheff, *Nanosci. Nanotechnol.*, **16**, 27 – 30 (2016).
- Jun-Ying Huang, Wei-Ren Liu, *J. Taiwan Inst. Chem. E.*, **96**, 205-213(2019).
- P. Zhouad, J. Weng et. all, *J. Power Sources*, **414**, 210-217 (2019).
- L. Ning, Y. Wu, S. Fang, E. Rahm, R. Holze, *J. Power Sources*, **133**, 229-242 (2004)
- M. Gutierrez, F. Garcia-Alvarado, E. Gonzalo, M. Dompablo, *J. Power Sources*, **160**, 523 – 528 (2006).
- V. Petrova, A. Stoyanova-Ivanova, P. Lilov, O. Petkov, G. Ivanova, B. Karamanova, A. Stoyanova, V. Mikli, *ECS Trans.*, **95**, 227-234 (2019).
- H. Maeda, Y. Tanaka, M. Fukutomi, T. Asano, *J. Appl. Phys.*, **27**, L209 - L210 (1988).
- M. Mladenov, R. Raicheff, L. Stoyanov, A. Stoyanova-Ivanova, S. Terzieva, D. Kovacheva, *BG Patent Reg. # 111 646* (in Bulgarian) (2013).
- F. Kukurugya, E. Kim, P. Nielsen, L. Horckmans, J. Spooen, K. Broos, M. Quaghebeur, *Hydrometallurgy*, **171**, 245-253 (2017).

Mathematical modeling and experimental validation of advanced alkaline water electrolyser U/j performance

Galin Borisov, Nevelin Borisov, Elica Petkucheva, Evelina Slavcheva

Acad. Evgeni Budevsk Institute of Electrochemistry and Energy Systems - Bulgarian Academy of Sciences, Akad. G. Bonchev 10, 1113 Sofia, Bulgaria

Received April 07, 2020; Accepted April 27, 2020

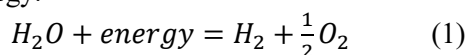
Hydrogen generation by water electrolysis plays an important role in the green energy cycle with zero carbon emissions. The recent development in the classical alkaline electrolysis including the development of new electrode materials, novel cell architecture and system design, offers possibilities for enhanced kinetics and improved energy efficiency. At the same time, the mathematical modeling and simulations of the reaction mechanisms are more and more often used to predict the response of the system to varying operating conditions which in turn, speeds up additionally the progress of this clean energy converting technology. This paper presents a simple modeling of advanced alkaline water electrolyser using the theoretical thermodynamic functions and electrochemical equations by means of free Scilab 6.0 software. The model allows the calculation of the U/j characteristics as well as parameters such as reversible potential, activation and ohmic losses of the electrochemical process. It is validated using real experimental data obtained in a single electrolysis cell with Ni-based electrodes and Zifron Perl 500 diaphragm at 25 °C. Through extrapolation of the results obtained, the model is applied to predict the electrochemical performance of the cell at elevated temperatures up to 80 °C and current densities up to 1 A.cm⁻².

Keywords: Hydrogen production, alkaline electrolyser, U/j performance, mathematical modeling

INTRODUCTION

The renewable energy sources (wind, solar, etc.) are considered as zero emission technologies for electricity generation that will replace the carbon based economy. A major drawback of these technologies is their intermittent character. For this reason, the balancing of the electric grid is a real challenge as the unused electric energy needs to be curtailed. A promising solution for the problem is the usage of hydrogen generators as energy balancing consumers [1]. The advanced alkaline water electrolysers are considered as second-generation systems for industrial production of clean hydrogen. This type of electrical energy converters have been successfully upgraded in the last years concerning energy efficiency, electron and mass transport balance, size, weight, etc. [2]. The principal scheme of the advanced alkaline water electrolyser is presented in fig. 1.

The hydrogen generators with alkaline electrolyte consist of two chambers separated by OH⁻ conductive diaphragm also called separator. The system operates with metal mesh electrodes (stainless steel or nickel-based) with large surface area. The water splitting reaction (eq. 1) is an endothermic process and in order to proceed it requires energy.

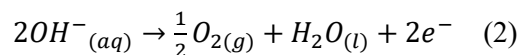


* To whom all correspondence should be sent.

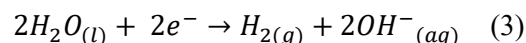
E-mail: gal.rusev@ices.bas.bg

The partial electrochemical reactions occurring on the anode and cathode of the cell are presented with equations (2) and (3), respectively.

Anode reaction:



Cathode reaction:



Each partial reaction in turn, goes through number of consecutive steps described in the literature [3].

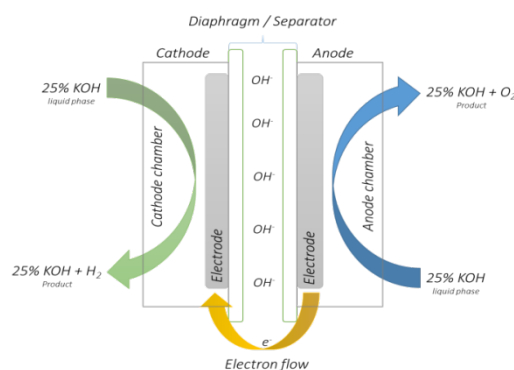


Fig.1. Principal scheme of advanced alkaline water electrolyser in a single cell mode

In order to split the water molecule to hydrogen and oxygen (according eqs. 2 and 3), an electric current flow (DC) is needed between both

electrodes. The hydrogen gas is produced on the cathode. Based on the fundamental thermodynamics and the basic electrochemical equations, the required minimum electric voltage to split the water electrochemically is determined by Gibbs equation (eq. 4):

$$\Delta G = zFE_{rev} \quad (4)$$

where ΔG is the Gibbs energy, z – is the number of electrons and F – Faraday constant, E_{rev} – reversible potential. E_{rev} is easily calculated by eq. (5):

$$E_{rev} = \frac{\Delta G}{zF} \quad (5)$$

The reversible potential correlates with the generator temperature and reflects the thermodynamic effects of the electrochemical reaction. At standard conditions (25°C, 1 atm) the value of E_{rev} is 1.229 V.

The water dissociation is also influenced by the catalytic activity of the electrodes. During the electrolysis process the cell voltage, U_{cell} , can be expressed as a sum of all potential barriers, namely the reversible potential, E_{rev} , the activation potential of both partial reactions, E_{act} , and the ohmic losses, E_{ohmic} , of the process. The mathematical relationship is presented by eq. (6).

$$U_{cell} = E_{rev} + E_{act} + E_{ohmic} \quad (6)$$

Both partial reactions according eqs. (2) and (3) have their own activation energy, while the activation energy of the electrochemical conversion is expressed by eq. (7).

$$E_{act} = s \log\left(\frac{t_1 + \frac{t_2}{T} + \frac{t_3}{T^2}}{A} I + 1\right) \quad (7)$$

Theoretically, the activation overpotential, E_{act} , increases with the increasing current density, while it can be decreased if active catalysts are integrated the both electrodes. In case of alkaline water electrolysis the transition metals such as Ni and its alloys have demonstrated high efficiency, resp. low overpotential, concerning both partial reactions [4-6].

The temperature dependence of the ohmic resistance (r) and the overvoltage (s) coefficients are described in details in the specialized literature [7]. The ohmic resistance of the advanced alkaline water electrolyser is related mainly to the low electrolyte conductivity. E_{ohmic} can be expressed as follows (eq. 8):

$$E_{ohmic} = \frac{\delta}{\varrho} I \quad (8)$$

where δ is the thickness of the diaphragm (cm), ϱ is the cell conductivity (S.cm⁻¹) which strongly

depends on the KOH concentration in the cell, and I is the operating current density.

This paper presents a simple modeling of advanced alkaline water electrolyser based on the partial electrode reactions in fig. 1, following the thermodynamic equations and dependencies expressed by eqs. (4-8). The mathematical calculations are performed using free Scilab 6.0 software. The energy requirements for the electrochemical conversion of water are calculated at KOH concentration and cell temperature input values fixed at 25 wt.% and 25 °C, respectively. The results are validated using experimental data obtained in a patented single electrolysis cell [8] with highly advanced Ni based electrodes (both for anode and cathode) and possibility to operate at temperatures up to 120 °C and pressure up to 5 bar.

EXPERIMENTAL

A. Mathematical modeling data

The mathematical modeling is performed using a free Scilab 6.0 software. The equations (4-8) are applied as programmable code directly in the Scinote (part of the software). The obtained dependencies are imported as data file in Origin 2019b in order to make precise comparison between the mathematical calculations and the real experimental data. The used variables are summarized in Table 1.

Table 1: Nomenclature of the used variables

| Symbol | Parameters | Dimensions | Values |
|------------|---|------------------------------|--------|
| A | Area of electrode | [m ²] | 0.0001 |
| ΔG | Gibbs free energy | [J.mol ⁻¹] | - |
| F | Faraday constant | [C.mol ⁻¹] | 96485 |
| T | Temperature | [K] | 293 |
| V | Cell voltage | [V] | - |
| n | Number of cells | [n] | 1 |
| r | Ohmic resistance coefficient | [Ω .m ²] | 1 |
| s | Coefficient for overvoltage on electrodes | [V] | 0.185 |
| z | Number of electrons | [n] | 2 |
| I | Current density | [A.cm ⁻²] | 0 - 1 |
| E_{rev} | Reversible potential | [V] | 1.229 |

B. Advanced alkaline water electrolyser - preparation and assembling

In order to validate the developed mathematical model the performance of an advanced laboratory

alkaline electrolyser is evaluated experimentally in a single cell mode. The cell consists of two Ni-based electrodes with 7 cm² geometric area. They have a double layered structure - a gas diffusion support (Ni foam with 96% porosity) and 25 μm thick micro porous layer (mixture of Ni powder and PTFE at ration 70:30 wt.%; the preparation procedure is described in details elsewhere [9]). The diaphragm integrated in the cell is Zifron Perl (0.5 mm thick, 56% porosity). The electrolyte used is 25 wt.% KOH. The cell performance is characterized by U/j polarization curves recorded in range 0 A.cm⁻² to 0.1 A.cm⁻² (cell voltage) at scan rate of 1 mA.s⁻¹. The measurements are carried out using commercial Potentiostat/Galvanostat Gamry, model 1010E.

RESULTS AND DISCUSSION

The operation performance of the electrolyser is characterized by the change of the cell voltage as a function of the flowing current density, j (A.cm⁻²). This dependence known also as voltammogram or U/j curve presents the response of electrolyser on varying electrical load. In this work the calculations and experiments are performed in the current density range from 0 A.cm⁻² to 1 A.cm⁻². The lower current density range requires low cell voltage and the system demonstrates high energy efficiency combined with low hydrogen production rate [10]. In fig. 2 are compared the model voltammogram calculated according eqs. (4-8) and the experimental curve obtained in the laboratory electrolysis cell at current density varying from 0 to 0.1 A.cm⁻².

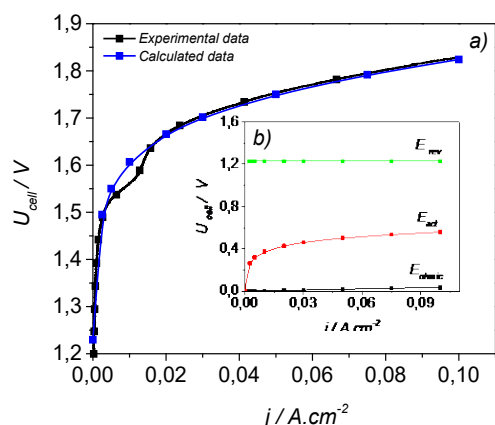


Fig. 2. Voltammograms of alkaline water electrolyser: a) comparison of mathematically calculated and experimental data; b) parameters, calculated by the developed model at 20 °C

Both voltammograms (experimental and modeled) fit perfectly, which validates the developed mathematical model. The increase of current density leads to increase in the cell

overpotential. The process of hydrogen evolution starts at potentials of 1.6 V - 1.7 V where the current density value is 0.01 A.cm⁻² – 0.015 A.cm⁻². At these conditions, the cell overpotential calculated according eqs. (5) and (6) varies in the range 0.371 V to 0.471 V.

The parameters determining the cell voltage (E_{rev} , E_{act} , E_{ohmic}), are presented in fig.2b as function of the current density. It is seen that at low current densities the cell voltage strongly depends on the activation overpotential and the electrolysis starts at E_{act} of about 0.35 V. The part of the cell voltage which is due to ohmic losses, E_{ohmic} is a linear function of current density and at low current densities it has much lower values compared to E_{act} .

In order to predict the behavior of the electrolyser at higher loads and elevated operating temperatures, the validated data from fig. 2 are applied in the model and the calculations are extended in the current density range up to 1 A.cm⁻² and temperatures up to 80 °C. The calculated results are presented in fig. 3.

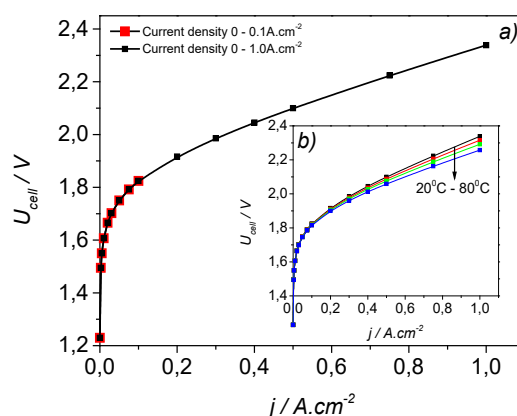


Fig. 3. U/j characteristics: a) experimental data (in red) and extended calculated U/j curve (in black) at current density up to 1 A.cm⁻²; b) temperature dependence of the modeled U/j curves

It is seen that the increase of j leads to gradual change in the slope of the modeled U/j curve which above 0.2 A.cm⁻² becomes linear. At current density of 1 A.cm⁻² the cell voltage reaches value of 2.35 V.

The inset figure 3b shows the temperature dependence of the modeled U/j curves in the range 20 °C to 80 °C. The overall cell voltage depends essentially on the operating temperature. At current density of 1 A.cm⁻² it drops with approximate 10 mV per each 10 °C temperature increase.

The change of E_{ohmic} at these extended operating conditions (j up to 1 A.cm⁻² and temperature up to 80 °C) again demonstrates clear lineal dependency versus current density (fig. 4). At

current density of 1 A.cm^{-2} E_{ohmic} reaches values of 0.375 V at 20°C and is decreasing with approximately 20 mV per each temperature step of 20°C .

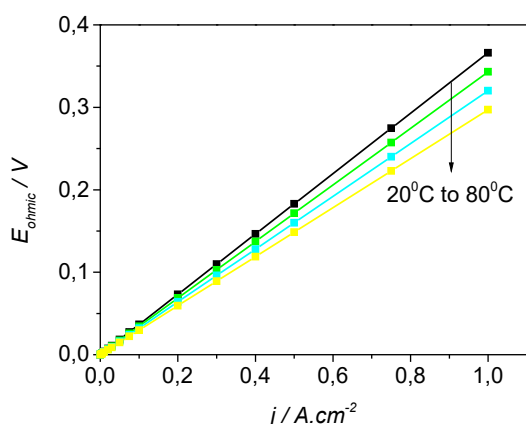


Fig. 4. Ohmic losses as function of current density at operating temperature range 20°C - 80°C

The respective calculations of E_{act} as function of current density are shown in fig. 5. It is seen that the increase in cell temperature has impact on E_{act} , however it is much lower than on E_{ohmic} (fig. 5b).

It should be noted that the activation losses occur because the cell needs energy to initiate reactions at both electrodes - anode and cathode. As a result, a voltage drop is initialized inside the cell. With the increase of current density, the slope of the U/j curve changes. The activation polarization becomes less significant, while the ohmic effect becomes dominating.

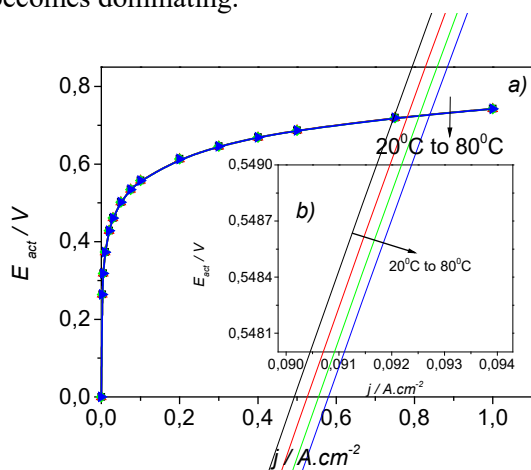


Fig. 5. Activation losses vs. current density: a) under

operating temperature in range of $20 - 80^\circ\text{C}$, b) zoomed results in the potential range 548.0 mV – 549.0.V

CONCLUSIONS

The developed mathematical model based on fundamental thermodynamics and electrochemical relationships enables to calculate and predict electrochemical functions such as energy barriers, activation losses, ohmic drops and U/j performance characteristics of water electrolyser. It is validated through input of real experimental data obtained in advanced alkaline electrolysis cell and used to predict the cell performance at extended operating conditions namely, elevated cell temperatures and heavier electrical loads.

Acknowledgment: This research is funded by the National Science Fund of Bulgaria, Contract KII-06-OIIP04. The experiments are performed using the equipment of distributed Research Infrastructure INFRAMAT (part of Bulgarian National Roadmap for Research Infrastructures) supported by Bulgarian of Education and Science under Contract DOI-155/28.08.2018

REFERENCES

1. F. Martin, G. Hernandez, *Int. J. Hydrogen Energy*, **37**, 1151 (2012).
2. M. Schalenbach, O. Kasian, K. Mayrhofer, *Int. J. Hydrogen Energy*, **43**, 11932 (2018).
3. S. Marini, P. Salvi, P. Nelli, R. Pesentia, M. Villa, M. Berrettoni, G. Zangari, Y. Kiros, *Electrochim. Acta*, **82**, 384 (2012).
4. M. Kumar, N. Shetti, *Mater. Sci. Eng. Technol.*, **1**, 160 (2018).
5. S. Ahn, H. Park, I. Choi, S. Yoo, S. Hwang, H. Kim, E. Cho, C. Yoon, H. Park, H. Son, J. Hernandez, S. Nam, T. Lim, S. Kim, J. Jang, *Int. J. Hydrogen Energy* **38**, 13493 (2013).
6. S. Hong, S. Ahn, J. Choi, J. Kim, H. Kim, H. Kim, J. Jang, H. Kim, S. Kima, *J. Appl. Surf. Sci.*, **349**, 629 (2015).
7. Ø. Ulleberg, *Int. J. Hydrogen Energy*, **28**, 21 (2003).
8. G. Borisov, N. Borisov, E. Slavcheva, Bulg. Patent № 4341/ 2019
9. G. Borisov, A. Stoyanova, E. Lefterova, E. Slavcheva, *Bulg. Chem. Comm.*, **4**, 186 (2013).
10. S.Shiva Kumar, V. Himabindu, *Mater. Sci. Eng. Technol.*, **2**, 442 (2019).

Impedance spectroscopy studies of the electrochemical hybrid supercapacitors based on activated carbon and iron oxides

Elefteria Lefterova*, Svetlana Veleva, Antonia Stoyanova

Acad. Evgeni Budevsk Institute of Electrochemistry and Energy Systems - Bulgarian Academy of Sciences, Akad. G. Bonchev 10, 1113 Sofia, Bulgaria

Received February 10, 2020; Accepted April 17, 2020

Symmetric and hybrid supercapacitors were developed and investigated by electrochemical impedance spectroscopy (EIS). Activated nanoporous carbon (commercial product, TDA Research, USA) and electrochemically active iron oxides - Fe_2O_3 (hematite) and Fe_3O_4 (magnetite) were laboratory synthesized and used as electrode materials for assembling of supercapacitor cells. LiBF_4 with an organic solvent mixture of ethylene carbonate/dimethyl carbonate (1:1) was served as an electrolyte. The results from EIS measurements show the possibility of application of magnetite and hematite as electrochemically active materials for hybrid lithium battery–supercapacitor systems and can provide guidance in selection the most suitable metal oxides, as composite electrode materials in supercapacitors.

Keywords: Magnetite, hematite, activated carbon, hybrid supercapacitors, impedance spectroscopy

INTRODUCTION

Among the various advanced solutions, concerning energy storage and conversion technologies, energy can in particular be stored electrochemically in accumulators (batteries) and supercapacitors (SCs). Although batteries currently present much higher energy density, their relatively low power density and poor cycle life hinder high power demanding applications such as regenerative braking systems. By contrast, supercapacitors store larger amounts of energy than the traditional dielectric capacitors and provide energy far faster than batteries. Therefore, they are particularly adapted for applications requiring energy pulses in short periods of time [1]. Although supercapacitors are now commercially available, they still require improvements, especially for enhancing their energy density and cut the cost at the same time. Hybrid electrochemical systems involving hybridization of a faradaically rechargeable battery-type electrode with an electrochemical double-layer capacitor-type electrode (e.g. asymmetric supercapacitors) show promising capability to achieve this [2]. On this basis various hybrid capacitor configurations, consisting of activated carbon and a negative electrode based on metal oxides (nickel, lead or manganese oxides) in non-aqueous electrolytes, are studied [2, 3].

The iron oxides - Fe_2O_3 and Fe_3O_4 are promising electrode materials for lithium-ion batteries because of their low cost, simple manufacturing process, wide range of sources, non-toxicity and

environmental friendliness, and mainly – large theoretical specific capacity of both oxides [4-6].

In our previous studies hybrid lithium battery–supercapacitors are assembled by an electrode of activated carbon, a composite electrode with activated carbon matrix and addition of 50 wt. % Fe_3O_4 or Fe_2O_3 and they are subjected to charge/discharge cycling test under galvanostatic conditions at different current loads and continuous cycling. It is found, that the developed hybrid supercapacitors, especially the magnetite based cell, demonstrate high current efficiency and specific capacity higher than the capacities of the basic symmetric capacitor as well as stable capacity behaviours at prolong cycling [7].

These results prove the possibility of application of magnetite and hematite as electrochemically active material for hybrid lithium battery–supercapacitor systems and provoked our further interest in detailed study of their electrochemical properties.

Usual testing schedule of SCs was always followed involving galvanostatic charging/discharging, cyclic voltammetry and other recommended experiments. The electrochemical impedance spectroscopy (EIS) of supercapacitors provide additional information about the faradaic reactions, internal resistances as serial resistance and charge transfer resistance. The advantage of the EIS over other testing techniques of SCs is the possibility of identification, separation and evaluation of the characteristic resistances as

* To whom all correspondence should be sent.
E-mail: e.lefterova@iees.bas.bg

electronic contacts at the current collector/ active electrode interface, charge transfer, electric resistance of the electrode, diffusion, etc . In addition, the pseudocapacitance of the electrode can be distinguished from the double-layer capacitance over a range of frequencies [8].

The objective of the present work is to investigate using impedance spectroscopy an electrochemical hybrid lithium battery-supercapacitor composed by an activated carbon electrode, a composite electrode with activated carbon matrix and addition of Fe₂O₃ and Fe₃O₄, and a non-aqueous electrolyte. The results obtained from EIS can be used as guidance in selecting the most suitable metal oxides as electrode materials for supercapacitors.

EXPERIMENTAL

Synthesis of nanosized Fe₂O₃ and Fe₃O₄

Activated nanoporous carbon (AC) and electrochemically active iron oxides - α -Fe₂O₃ (hematite) and Fe₃O₄ (magnetite) were used as electrode materials for assembling of hybrid supercapacitor cells.

Nanosized magnetite and hematite were laboratory synthesized. Magnetite was obtained by sonochemical synthesis which is carried out by precipitation the corresponding metal hydroxides and their further decomposition to oxides under ultrasonic irradiation. As starting compounds FeCl₂.6H₂O, Fe (NO₃)₃.9H₂O and NaOH in a molar ratio of 1:2:5 were used.

Hematite was obtained by solution combustion synthesis method. As starting reagents Fe (NO₃)₃.9H₂O and sucrose (as fuel) in 3.2:1 molar ratio were used. Stoichiometric amounts of the reagents were dissolved in an appropriate amount of deionized water.

The activated carbon is a commercial product (TDA Research, USA).

Preparation of hybrid supercapacitor cells and electrochemical testing

The activated carbon and iron-oxides (Fe₂O₃ or Fe₃O₄) were used to fabricate electrodes for two types of electrochemical cells for capacity measurements. The first type is a symmetric supercapacitor cell using two identical electrodes from activated carbon and a non-aqueous electrolyte – lithium tetrafluoroborate (LiBF₄) with organic solvent – ethylene carbonate and dimethyl carbonate (EC/DMC) mixture in ratio 1:1. The second one was a hybrid battery - supercapacitor cell, which was assembled by a composite electrode and an activated carbon electrode. The composite (negative) electrode was prepared of activated carbon matrix with

addition (50 wt. %) of iron oxide – Fe₂O₃ or Fe₃O₄. The positive electrode was made from the same activated carbon material. The same non-aqueous electrolyte – LiBF₄-EC/DMC (1:1) as in the symmetric supercapacitor cell is used. The prepared electrodes were soaked in organic electrolyte and then mounted in a coin-type cell with Glassmat separator and the cell was filled with electrolyte.

Electrochemical impedance spectroscopy (EIS)

Electrochemical impedance spectroscopy (EIS) measurements were carried out, using Phase Sensitive Multimeters Newtons4th Ltd. PsimetriQ-PSM1700 equipped with Newtons4th Impedance Analysis Interface (IAI). Experiments were conducted in two electrode cell in frequency range of 1 MHz to 1 mHz with sampling rate of 10 points per decade, and A.C. sinusoidal amplitude 10 mV. All EIS experiments were performed after the 50th cycle to be sure that the formation of SEI is completed. EIS data were analyzed in terms of an equivalent circuit model and a complex non-linear least squares fitting (CNLS) algorithm was used.

Theoretical remarks

Electrical impedance was defined by applying an A.C. potential to an electrochemical cell and then measuring the current through the cell. The electric potential is $\Delta E(\omega) = E_o e^{i\omega t}$ with small E_o amplitude (5–10 mV) and an angular frequency $\omega = 2\pi f$. Responding current was determined by $\Delta I(\omega) = I_o e^{i\omega t + \varphi}$, where I_o is the current amplitude and φ is the frequency-dependent phase angle between the applied potential $\Delta E(\omega)$ and the measured current $\Delta I(\omega)$. Therefore, the impedance Z is defined as:

$$Z(\omega) = \frac{\Delta E(\omega)}{\Delta I(\omega)} = \frac{E_o e^{i\omega t}}{I_o e^{i(\omega t + \varphi)}} = \frac{E_o}{I_o} e^{-i\varphi} = |Z(\omega)| e^{-i\varphi} = Z'(\omega) + iZ''(\omega), \quad (1)$$

where $Z'(\omega)$ and $Z''(\omega)$ are the real and imaginary parts of the complex impedance respectively, and $|Z(\omega)|$ is a module as $|Z(\omega)|^2 = Z'^2 + Z''^2$ [9,10].

The complex capacitance $C(\omega) = C'(\omega) - iC''(\omega)$ can be calculated from impedance data using equations [10]:

$$Z(\omega) = \frac{-1}{i\omega C(\omega)} \quad (2)$$

$$C'(\omega) = \frac{-Z''(\omega)}{\omega |Z(\omega)|^2} \quad (3)$$

$$C''(\omega) = \frac{Z'(\omega)}{\omega |Z(\omega)|^2} \quad (4)$$

In case of a pure capacitive behaviour ($Z'=0$ and $C''=0$, ideal capacitor) the relation is:

$$Z'' = \frac{-1}{C\omega} \quad (5)$$

The plot of $-Z''$ versus $1/\omega$ will be a straight line with a slope of $1/C$ and thus the capacity can be calculated [11].

The most used presentation of EIS data are Nyquist plot and Bode plot. In a complex plane (Nyquist plot) the real part is plotted on the X-axis and the imaginary part is plotted on the Y-axis. In Bode plot the impedance is plotted with log frequency on the X-axis and both the absolute values of the impedance $|Z|$ and the phase-shift on the Y-axis. A typical Nyquist plot of an electrochemical supercapacitor is presented in Fig. 1. Four frequency bands are distinguished and each can be described with the corresponding elements. Therefore the capacitive electrochemical systems can be represented by connection of electrical elements in a suitable equivalent circuit. The semicircle at high to medium frequencies (2) describing with (RC) elements is due to pore resistance in EDLC, or charge transfer resistance in pseudo capacitors as well as to the electrical resistance of low conductive electrodes. The high frequency region (1), bounded by the beginning of the semicircle (left-intercept of Z' at the Z' axis) gives the value of the effective series resistance (ESR) denoted as R_s and usually it is due to an electrical contact and/or electrolyte resistance. A line with slope $\cong 45^\circ$ at medium frequencies (3) and a nearly vertical line at low frequencies describe the diffusion process and presents by Finite-Length Warburg element (FLW) with open reflective (blocking) terminus:

$$Z_D = R_D \frac{\coth(i\tau\omega)^{\frac{1}{2}}}{(i\tau\omega)^{\frac{1}{2}}} \quad (6)$$

In the diffusion interpretation $\tau = L^2/D$ (L is the effective diffusion thickness, and D is the effective diffusion coefficient of the particle). At very low frequencies, the Z' approaches R and Z'' continues to increase - similar to the behaviour of a capacitor. A Randles equivalent circuit was used to modelling such electrochemical cells with mixed kinetic and charge-transfer control (fig. 1c). At lack of homogeneity the semicircle is depressed and low frequency line is declined (red line, fig.1b). In this case a constant phase element (CPE) replaces the capacitor, and Generalized Finite Warburg element (GFW) replaces FLW in Randles equivalent circuit as:

$$Z_{CPE} = \frac{-1}{T(i\omega)^\alpha} \quad (7)$$

$$Z_D = R_D \frac{\coth(i\tau\omega)^{\frac{\alpha}{2}}}{(i\tau\omega)^{\frac{\alpha}{2}}}, \quad (8)$$

where T is a capacitive parameter (in $Fs^{\alpha-1}$), and α is the constant phase exponent ($0 \leq \alpha \leq 1$) reflecting the deviation from ideal case [9].

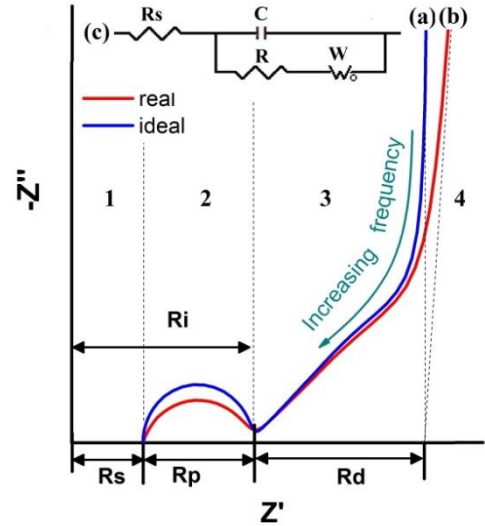


Fig. 1. Nyquist plot and equivalent (Randles) circuit model for the porous electrodes.

RESULTS AND DISCUSSION

Nyquist and Bode plots of the supercapacitors under investigation are shown in Figure 2 and Figure 3. The different electrochemical processes at the different frequencies ranges are well distinguished. The Nyquist plot of AC/AC and AC/AC+ Fe_3O_4 are close. Their A.C. response is intrinsic to porous electrode and similar to the presented in fig. 1. The difference consists in the high to middle frequencies range (2) where instead of one, two overlapped semicircles are depicted as it is shown in the zoomed plot (Fig. 2b). For this reason, another RC element is added to the Randles circuit (fig. 4) and this equivalent circuit is used for fitting procedure. The results are presented in Table 1.

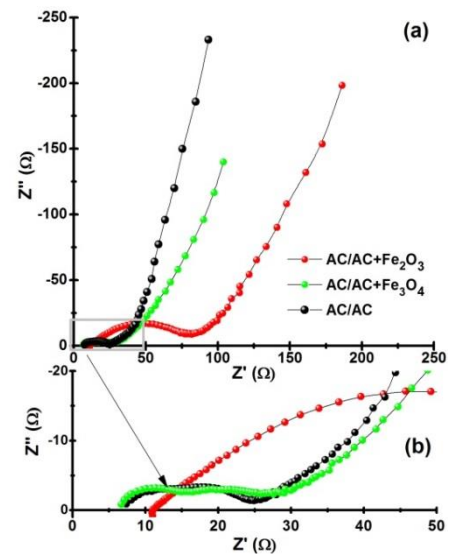


Fig. 2. Nuquist plot of symmetric and hybrid supercapacitors (a) full range; (b) the data of the high frequency range

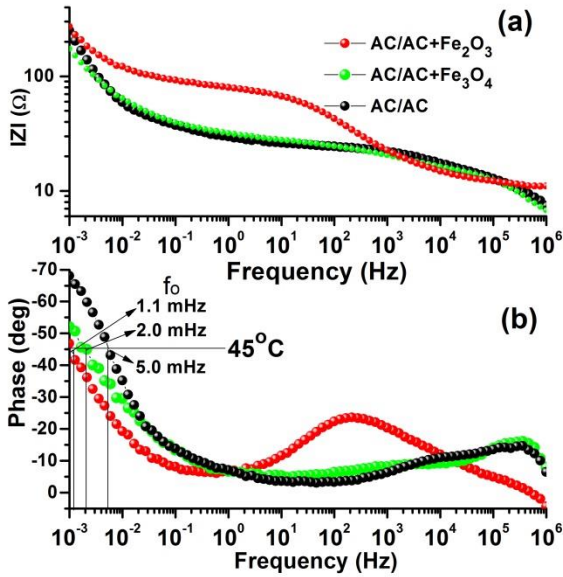


Fig. 3. Bode plots of symmetric and hybrid supercapacitors: (a) $|Z|$ vs. frequency; (b) phase vs. Frequency

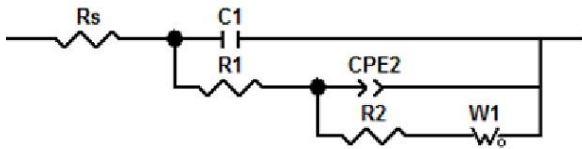


Fig. 4. Equivalent circuit describing EIS spectra

Table 1. Calculated impedance parameters

| Cell | CLNS | | | | | | | Linear fit | |
|------------------|-------------------|-------------------|------------------|-------------------|----------------------------|-----------------|--------------------|------------|------------------|
| | R_s Ω | R_1 Ω | C_1 μF | R_2 Ω | CPE2 T $mFs^{\alpha-1}$ | CPE α | WR_D Ω | χ^2 | C $F cm^{-2}$ |
| AC-AC | 7.96 | 4.37 | 0.108 | 12.73 | 0.303 | 0.53 | 48.85 | 0.00027 | 0.707 |
| AC-AC/ Fe_3O_4 | 7.34 | 5.57 | 0.121 | 12.87 | 0.077 | 0.499 | 38.46 | 0.00124 | 0.961 |
| AC-AC/ Fe_2O_3 | 11.7 | 3 | 1.36 | 61.47 | 0.464 | 0.59 | 57.28 | 0.00041 | 1.333 |

The hybrid cells have a greater slope of the line at low frequency range. This non-ideality is a typical feature of electrochemical charging processes, and may be interpreted as resulting from a distribution in macroscopic path lengths (non-uniform active layer thickness) or a distribution in microscopic charge transfer rates [14], adsorption processes, or surface roughness as well as from diffusion restrictions. The diffusion character is maintained almost to 1 mHz for hematite electrode, as it can be seen from Bode plot and confirmed by characteristic frequency f_0 ($f_{0Fe_2O_3}=1.1$ mHz) (fig. 3b). Characteristic frequency f_0 for capacitors is defined by the frequency where resistance and reactance are equal (-45° phase angle) i.e. f_0 divided the frequency range in two: at $f < f_0$ capacitive ($-90^\circ \leq \text{phase} < -45^\circ$) behaviour and at $f > f_0$ ($-45^\circ \leq \text{phase} \leq 0^\circ$) resistive [15].

Different explanation of the high frequency semicircle exist in the literature as electronic resistance of the electrode, ionic resistance in the pores, charge transfer trough electrolyte-electrode interface etc.. Taking account very low capacitance ($C_1 < 1 \mu F cm^{-2}$) this semicircle is due to ionic resistance in the pores. The second arc (frequency range 200 Hz-20 KHz) could be connected with lithium ion transport at separator interface or lithium ion (charge) transfer at an electrode/electrolyte interface (R_{ct}) (at lower frequency) [12,13]. The weak broadening of the second semicircle of hybrid AC/AC+ Fe_3O_4 cell is explained by the superposition of the two processes, one on the AC electrode and second of AC+ Fe_3O_4 electrode. For AC/AC+ Fe_2O_3 cell a large depressed semicircle is visible. The internal resistance R_i of hematite electrode exceeds in times the internal resistance of the AC and AC+ Fe_3O_4 cells (Table 1) and it is related to the lower specific area in results of the larger particles size as well as the low conductivity of the hematite [7].

The Bode plot reveals that the reaction of the iron oxide contained electrodes are shifted to lower frequencies and therefore the processes are slower in the hybrid cells.

The Fig. 5 shows the frequency dependence of the real and imaginary parts of capacitance, calculated from equations (3) and (4). C' sharply increases, when the frequency decreases below 1 Hz. It tends to be less frequency dependent for AC/AC cell. The imaginary part of the AC/AC capacitance goes through a maximum at a frequency $f_p = 3.5$ mHz defining a time constant τ_0 (or relaxation time) as $\tau_0 = 1/f_p$ [10]. For the asymmetric cells $f_p \leq 1$ mHz, i.e. f_p is out of measured frequency range.

The plot of $-Z''$ versus $1/f$ is a straight line at low frequencies as it can be seen from Figure 6. The capacitance of the cells was calculated from the slope according to equation (5).

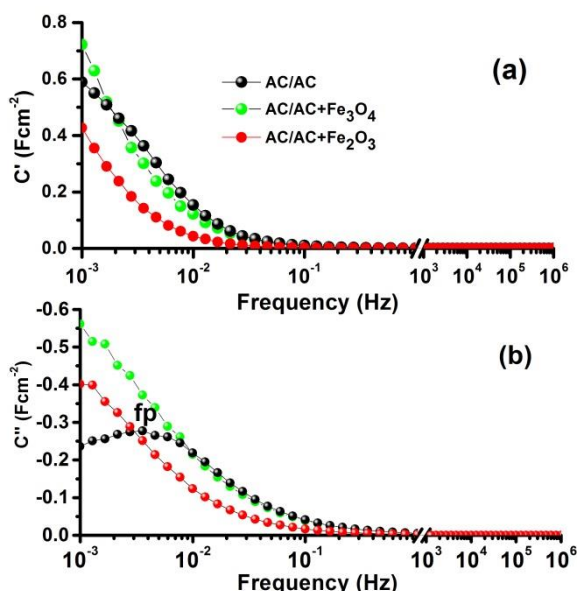


Fig. 5. Evolution of the real (C') and imaginary (C'') parts of capacitance vs. frequency

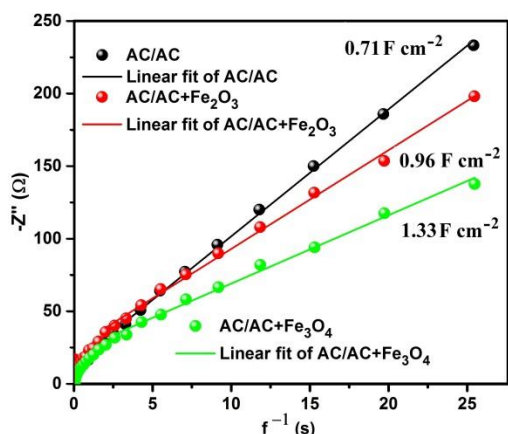


Fig. 6. The plot of the $-Z''$ vs. f^{-1} .

From CNLS and linear fit results summarized in Table 1, the following relationships are established: $R_s(\text{AC/AC}) \approx R_s(\text{AC/AC+Fe}_3\text{O}_4) < R_s(\text{AC/AC+Fe}_2\text{O}_3)$ and $R_2(\text{AC/AC}) \approx R_2(\text{AC/AC+Fe}_3\text{O}_4) < R_2(\text{AC/AC+Fe}_2\text{O}_3)$, where the higher $R_s(\text{AC/AC+Fe}_2\text{O}_3)$ value is due to the higher resistance of the electrode caused by the lower electronic conductivity of the hematite. The highest capacitance is obtained for AC/AC+Fe₃O₄ cell. In spite the large resistance of the hematite electrode, this hybrid cell has relatively high capacitance. This means that it is possible to significantly increase the hematite pseudo capacitance and reduce R_i , by increasing the specific surface area.

CONCLUSIONS

Electrochemical impedance spectroscopy (EIS) reveals that the magnetite based cell has the highest capacitance. In spite the highest intrinsic resistance the hematite electrode shows a relatively high

capacitance, and hence possesses a potential for significantly increase of its pseudo-capacitance by optimizing the particle size and morphology. The results demonstrate the applicability of the EIS method for providing guidance on appropriate selection of metal oxides as composite electrode materials in supercapacitor systems.

Acknowledgment: This work was financially supported by the Bulgarian National Science Fund through KP-06-OPR 04/5 project "Innovative hybrid supercapacitors as a challenge for efficient, safe and environmentally energy storage". Research equipment of distributed research infrastructure INFRAMAT (part of Bulgarian National roadmap for research infrastructures) supported by Bulgarian Ministry of Education and Science under contract D01-155/28.08.2018 was used in this investigation.

REFERENCES

1. Lu Wang, Y. Han., X. Feng, J. Zhou, P. Qi, Bo Wang, *Coord. Chem. Rev.*, **307**, 361 (2016).
2. C. Zhao, W. Zheng, *Front. Energy Res.*, **3**, 1 (2015).
3. T. Cottineau, M. Toupin, T. Delahaye, T. Brousse, D. Bélanger, *Appl. Phys. A*, **82**, 599 (2006).
4. J. Chen, L. Xu, W. Li, X. Gou, *Adv. Mater.*, **17**, 582 (2005).
5. W., Zhang Wu X., J. Hu, Y. Guo, L. Wan, *Adv. Funct. Mater.*, **18**, 3941 (2008).
6. D. Cericola, R. Kötz, *Electrochim. Acta*, **72**, 1 (2012).
7. S. Veleva, A. Stoyanova, R. Raicheff, D. Kovacheva, M. Mladenov, *J. Progr. Res. Chem.*, **4**, 179 (2017).
8. B. E. Conway, *Electrochemical Supercapacitors*, Springer Science+Business Media New York 1999
9. A. Lasia, *Electrochemical Impedance Spectroscopy and its Applications*, Springer Science+Business Media New York 2014
10. P. L. Taberna, P. Simon, and J. F. Fauvarque, *J. Electrochem. Soc.*, **150**, A292 (2003)
11. R. Negroiu, P. Svasta, C. Ionescu, A. Vasile, 1st PCNS Passive Components Networking Days, 12-15th Sep 2017, Brno, Czech Republic, paper 3.2. Supercapacitors Session, PCNS2017 Proceedings Pg.56-62
12. M. Stoller, R. Ruoff, *Energy Environ. Sci.*, **3**, 1294 (2010).
13. M. Gaberscek, J. Moskon, B. Erjavec, R. Dominko, J. Jamnik, *Electrochem. Solid-State Lett.*, **11** A170 (2008).
14. D. Gruet, B. Delobel, D. Sicsic, I. Lucas, V. Vivier, *Electrochim. Acta*, **295**, 787 (2019).
15. F. Beguin, E. Frackowiak, *Supercapacitors: Materials, Systems, and Applications*, John Wiley & Sons., 2013.

Instructions about Preparation of Manuscripts

General remarks: Manuscripts are submitted in English by e-mail. The text must be prepared in A4 format sheets using Times New Roman font size 11, normal character spacing. The manuscript should not exceed 15 pages (about 3500 words), including photographs, tables, drawings, formulae, etc. Authors are requested to use margins of 2 cm on all sides.

Manuscripts should be subdivided into labelled sections, e.g. INTRODUCTION, EXPERIMENTAL, RESULTS AND DISCUSSION, *etc.* **The title page** comprises headline, author(s)' names and affiliations, abstract and key words. Attention is drawn to the following:

a) **The title** of the manuscript should reflect concisely the purpose and findings of the work. Abbreviations, symbols, chemical formulae, references and footnotes should be avoided. If indispensable, abbreviations and formulae should be given in parentheses immediately after the respective full form.

b) **The author(s)**' first and middle name initials and family name in full should be given, followed by the address (or addresses) of the contributing laboratory (laboratories). **The affiliation** of the author(s) should be listed in detail (no abbreviations!). The author to whom correspondence and/or inquiries should be sent should be indicated by an asterisk (*) with e-mail address.

The abstract should be self-explanatory and intelligible without any references to the text and containing up to 250 words. It should be followed by keywords (up to six).

References should be numbered sequentially in the order, in which they are cited in the text. The numbers in the text should be enclosed in brackets [2], [5, 6], [9-12], etc., set on the text line. References are to be listed in numerical order on a separate sheet. All references are to be given in Latin letters. The names of the authors are given without inversion. Titles of journals must be abbreviated according to Chemical Abstracts and given in italics, the volume is typed in bold, the initial page is given and the year in parentheses. Attention is drawn to the following conventions: a) The names of all authors of a certain publications should be given. The use of "*et al.*" in the list of references is not acceptable; b) Only the initials of the first and middle names should be given. In the manuscripts, the reference to author(s) of cited works should be made without giving initials, e.g. "Bush and Smith [7] pioneered...". If the reference carries the names of three or more authors it should be quoted as "Bush *et al.* [7]", if Bush is the first author, or as "Bush and co-workers [7]", if Bush is the senior author.

Footnotes should be reduced to a minimum. Each footnote should be typed double-spaced at the bottom of the page, on which its subject is first mentioned. **Tables** are numbered with Arabic numerals on the left-hand top. Each table should be referred to in the text. Column headings should be as short as possible but they must define units unambiguously. The units are to be separated from the preceding symbols by a comma or brackets. Note: The following format should be used when figures, equations, *etc.* are referred to the text (followed by the respective numbers): Fig., Eqns., Table, Scheme.

Schemes and figures. Each manuscript should contain or be accompanied by the respective illustrative material, as well as by the respective figure captions in a separate file. As far as presentation of units is concerned, SI units are to be used. However, some non-SI units are also acceptable, such as °C, ml, l, etc. Avoid using more than 6 (12 for review articles) figures in the manuscript. Since most of the illustrative materials are to be presented as 8-cm wide pictures, attention should be paid that all axis titles, numerals, legend(s) and texts are legible.

The authors are required to submit the text with a list of three individuals and their e-mail addresses that can be considered by the Editors as potential reviewers. Please note that the reviewers should be outside the authors' own institution or organization. The Editorial Board of the journal is not obliged to accept these proposals.

The authors are asked to submit **the final text** (after the manuscript has been accepted for publication) in electronic form by e-mail. The main text, list of references, tables and figure captions should be saved in separate files (as *.rtf or *.doc) with clearly identifiable file names. It is essential that the name and version of the word-processing program and the format of the text files is clearly indicated. It is recommended that the pictures are presented in *.tif, *.jpg, *.cdr or *.bmp format.

The equations are written using "Equation Editor" and chemical reaction schemes are written using ISIS Draw or ChemDraw programme.

EXAMPLES FOR PRESENTATION OF REFERENCES

REFERENCES

1. D. S. Newsome, *Catal. Rev.–Sci. Eng.*, **21**, 275 (1980).
2. C.-H. Lin, C.-Y. Hsu, *J. Chem. Soc. Chem. Commun.*, 1479 (1992).
3. R. G. Parr, W. Yang, *Density Functional Theory of Atoms and Molecules*, Oxford Univ. Press, New York, 1989.
4. V. Ponec, G. C. Bond, *Catalysis by Metals and Alloys (Stud. Surf. Sci. Catal., vol. 95)*, Elsevier, Amsterdam, 1995.
5. G. Kadinov, S. Todorova, A. Palazov, in: *New Frontiers in Catalysis (Proc. 10th Int. Congr. Catal., Budapest (1992))*, L. Guzzi, F. Solymosi, P. Tetenyi (eds.), Akademiai Kiado, Budapest, 1993, Part C, p. 2817.
6. G. L. C. Maire, F. Garin, in: *Catalysis. Science and Technology*, J. R. Anderson, M. Boudart (eds.), vol. 6, Springer Verlag, Berlin, 1984, p. 161.
7. D. Pocknell, *GB Patent 2 207 355* (1949).
8. G. Angelov, PhD Thesis, UCTM, Sofia, 2001, pp. 121-126.
9. JCPDS International Center for Diffraction Data, *Power Diffraction File*, Swarthmore, PA, 1991.
10. *CA* **127**, 184 762q (1998).
11. P. Hou, H. Wise, *J. Catal.*, in press.
12. M. Sinev, private communication.
13. <http://www.chemweb.com/alchem/articles/1051611477211.html>.

Texts with references which do not match these requirements will not be considered for publication

CONTENTS

| | |
|---|----|
| <i>Preface – SED’2019</i> | i |
| <i>K. Nešović, V. Mišković-Stanković</i> , Graphene-based poly(vinyl alcohol)/chitosan hydrogels with electrochemically synthesized silver nanoparticles for medical applications – a review | 5 |
| <i>V. Milusheva, B. Tzaneva, M. Petrova, B. Stefanov</i> , Graphene-based electroless copper-based layers deposition on anodized aluminum | 15 |
| <i>F. Caubert, P.-Louis Taberna, L. Arurault, B. Fori</i> , Electrophoretic deposition of boehmite particles to improve the anti-corrosion behavior of anodized aluminum alloy 2024-T3..... | 21 |
| <i>M. Georgieva, G. Avdeev, V. Milusheva, D. Lazarova, M. Petrova</i> , Investigation of the structure of copper coatings obtained by chemical deposition from formaldehyde-free solution on dielectrics | 28 |
| <i>V. Vitkova, Ch. Minetti, A. Stoyanova-Ivanova</i> , Bending rigidity of lipid bilayers in electrolyte solutions of sucrose | 35 |
| <i>A. Petrovski, P. Perica Paunović, A. Grozdanov, A. T. Dimitrov, I. Mickova, G. Gentile, M. Avella, D. Lilova</i> , Electrochemical polymerization and in situ characterization of PANI in presence of chemically modified graphene | 41 |
| <i>A. Popova, A. Vasilev, N. Ivanova</i> , Quaternary ammonium bromides as mild steel corrosion inhibitors in acid media | 49 |
| <i>Y. Marinov, G. Hadjichristov, T. Vlahov, H. Koduru, N. Scaramuzza</i> , Electrochemical impedance and dielectric spectroscopy study of TiO ₂ -nanofilled PEO/PVP/NaIO ₄ ionic polymer electrolytes | 57 |
| <i>V. Majidzade, A. Aliyev, D. Tagiyev</i> , Electrochemical deposition of Sb ₂ Se ₃ thin films semiconductor from tartaric acid solution | 62 |
| <i>D. Nicheva, B. Abrashev, I. Piroeva, V. Boev, T. Petkova, P. Petkov, K. Petrov</i> , NiCo ₂ O ₄ /Ag as catalyst for bi-functional oxygen electrode | 68 |
| <i>V. Majidzade, S. Mammadova, E. Petkucheva, E. Slavcheva, A. Aliyev, D. Tagiyev</i> , Co-electrodeposition of iron and sulfur in aqueous and non-aqueous electrolytes..... | 73 |
| <i>G. Ivanova, V. Petrova, O. Petkov, B. Minchev, P. Lilov, A. Stoyanova- Ivanova, A. Stoyanova</i> , Effect of ball milling treatment on the Zn electrode properties in Ni- Zn battery | 79 |
| <i>G. Borisov, N. Borisov, E. Petkucheva, E. Slavcheva</i> , Mathematical modeling and experimental validation of advanced alkaline water electrolyser U/j performance..... | 84 |
| <i>E. Lefterova, S. Veleva, A. Stoyanova</i> , Impedance spectroscopy studies of the electrochemical hybrid supercapacitors based on activated carbon and iron oxides..... | 88 |
| Instruction to the authors | 93 |

